INFORMATION TO USERS

This manuscript has been reproduced from the microfilm master. UMI films the text directly from the original or copy submitted. Thus, some thesis and dissertation copies are in typewriter face, while others may be from any type of computer printer.

The quality of this reproduction is dependent upon the quality of the copy submitted. Broken or indistinct print, colored or poor quality illustrations and photographs, print bleedthrough, substandard margins, and improper alignment can adversely affect reproduction.

In the unlikely event that the author did not send UMI a complete manuscript and there are missing pages, these will be noted. Also, if unauthorized copyright material had to be removed, a note will indicate the deletion.

Oversize materials (e.g., maps, drawings, charts) are reproduced by sectioning the original, beginning at the upper left-hand corner and continuing from left to right in equal sections with small overlaps.

ProQuest Information and Learning
300 North Zeeb Road, Ann Arbor, MI 48106-1346 USA
800-521-0600

University of Alberta

Using Hydrogen to Extend the EGR Limit of SI Engines

by

David M. Arthur

A thesis submitted to the Faculty of Graduate Studies and Research in partial fulfillment of the requirements for the degree of Master of Science.

Department of Mechanical Engineering

Edmonton, Alberta
Spring 2005

We are the ones we have been waiting for

The Hopi Elders

to Didem

Abstract

A series of experiments was completed on a single-cylinder Co-operative Fuel Research engine to determine the effect of H_2 addition on the extension of the exhaust gas recirculation (EGR) limit of a natural gas fuelled spark ignition engine. All experiments were conducted at 1200 RPM, wide open throttle and maximum brake torque spark timing. The addition of a 17.4% H_2 energy fraction resulted in a doubling of the original EGR mass fraction limit, from 14.8% to 30.0%. Such an extension of the EGR limit had significant implications on all metrics of engine performance: indicated specific NO emissions decreased by 93%, from 1.5 to 0.1 g/kW h while neither indicated specific CO or indicated specific total hydrocarbon emissions were greatly affected; fuel conversion efficiency (η_{fc}) decreased slightly, from 31.4 to 30.9%, although this change falls within the uncertainty in determining η_{fc}; indicated mean effective pressure decreased by 20%, from 5.21 to 4.17 bar; and "usage" indicated specific CO_2 emissions fell by 18%, from 637 to 521 g/kW h.

ACKNOWLEDGEMENTS

Assistance in the completion of this study came in several forms from many sources, all of which are gratefully recognized.

I would like to begin by thanking my supervisor, Dr. David Checkel, for his understated guidance and sense of humour. Through a combination of subtle suggestions and encouragement, he has allowed me to develop confidence and independence in my ideas.

Invaluable technical assistance in the design, construction and troubleshooting of the experimental system was provided by Mr. Bernie Faulkner and Mr. Terry Nord. Their willingness to help is matched only by their esoteric senses of humour and both are equally appreciated.

Several pieces of equipment were either loaned or donated for use in the experimental system. Dr. Bob Koch and Mr. Randy Burkett are both gratefully acknowledged for their respective contributions.

The financial assistance of many organizations and individuals was essential in the completion of this study. Acknowledgements are extended to: the Natural Sciences and Engineering Research Council of Canada, Alternative Fuel Systems, the Auto21 Network of Centres of Excellence, the University of Alberta, the Faculty of Engineering, David Morris Fine Cars, the Government of Alberta and Canadian Natural Resources Limited.

Support of a different sort is attributed to the indelible friendships which I have made over the course of this study. Beyond the typical contributions of close friends, Mr. Pat Kirchen is recognized for his quick wit and for keeping me honest in and out of the lab; Mr. Senthil Ponnusamy for the exercises in keeping my right-brain active; and Mr. Travis Manchur for the exercises in keeping my left-wing arguments sharp and close at hand.

I would also like to thank my Mom, Dad and brother for their love and support, not only during this study, but throughout my entire education. Their pride is a constant reminder to do my best.

Finally, I would like to thank my wife Didem for her love, encouragement and understanding. Her innumerable contributions have had a direct impact not only on the completion and quality of this work, but also on my happiness during its composition.

CONTENTS

1 Introduction 1

2 Review of Relevant Literature 5
- 2.1 The Effect of Mixture Composition on Combustion 5
  - 2.1.1 Exhaust Gas Dilution 6
  - 2.1.2 H_2 Addition 8
- 2.2 H_2 Addition to Extend EGR Limit of an SI Engine 10
- 2.3 Summary 14

3 Experimental System and Procedure 16
- 3.1 Instrumented Engine 16
  - 3.1.1 Intake System 17
  - 3.1.2 Fuelling System 19
  - 3.1.3 EGR System 20
  - 3.1.4 Ignition System 21
  - 3.1.5 Cylinder Pressure Measurement 21
  - 3.1.6 Torque Measurement 22
  - 3.1.7 Emissions Measurement 22
  - 3.1.8 Data Acquisition System 23
- 3.2 Test Procedure 26
  - 3.2.1 Startup Procedure 26
  - 3.2.2 Experimental Procedure 27

4 Results and Discussion 41
- 4.1 Data Post-Processing 42
  - 4.1.1 Exhaust Emissions 42
  - 4.1.2 Chauvenet's Criterion 44
- 4.2 The Effect of Spark Timing on Engine Performance 46
  - 4.2.1 Output Torque 47

4.2.2 Combustion Stability 50
4.2.3 Fuel Conversion Efficiency 50
4.2.4 Pollutant Emissions 52
4.3 The Effect of EGR on Engine Performance 60
4.3.1 Output Torque 60
4.3.2 Combustion Stability 62
4.3.3 Fuel Conversion Efficiency 64
4.3.4 Pollutant Emissions 71
4.4 The Effect of H_2 Addition on Exhaust Diluted Engine Performance 75
4.4.1 Output Torque 77
4.4.2 Combustion Stability 77
4.4.3 Fuel Conversion Efficiency 81
4.4.4 Pollutant Emissions 86

5 Conclusions and Future Work **98**
5.1 Conclusions 98
5.2 Future Work 100

A Detailed Equipment Information **107**
A.1 Equipment Specifications 107
A.2 Equipment Operating Principles 111
A.2.1 Chemiluminescent Detector Gas Analyzer 111
A.2.2 FID Gas Analyzer 111
A.2.3 NDIR Gas Analyzer 111
A.2.4 Paramagnetic Gas Analyzer 112

B Calibration and Error Analysis **113**
B.1 Overview of Measurement Error 113
B.2 Differential Error Analysis Overview 116
B.3 Mass Flow Meters 116
B.3.1 Air Mass Flow Meter 116
B.3.2 H_2 Mass Flow Meter 117
B.3.3 Natural Gas Mass Flow Meter 119
B.4 Pressure Transducers 121
B.5 Dynamometer Load Cell 123
B.6 Gas Analyzers 127
B.6.1 Chemiluminescent Detector Gas Analyzer 127

B.6.2 FID Gas Analyzer 130
B.6.3 NDIR Gas Analyzer 132
B.6.4 Paramagnetic Gas Analyzer 135
B.7 Rotary Encoder Alignment 139
B.8 Cylinder Pressure Transducer 139

C Physical Properties **142**
C.1 Gaseous Fuels 142
C.1.1 Natural Gas 142
C.1.2 H_2 142
C.2 Air/Fuel Mixture 142

D Calculating EGR Mass Fraction **145**

List of Tables

3.1 CFR Engine Specifications 17
3.2 CFR Schematic Label Descriptions 30
3.3 Fuelling System Schematic Label Descriptions 32
3.4 Emissions Measurement System Schematic Label Descriptions 34

4.1 Statistical Effects of Applying Chauvenet's Criterion 46
4.2 CFR Engine Operating Conditions 47
4.3 Physical Properties of H_2 and CH_4 78
4.4 H_2 Required to Maintain Combustion Stability 81

A.1 Detailed Equipment Information 108

B.1 Instrument and Calibration Uncertainty 115
B.2 Kistler 6043A Cylinder Pressure Transducer Properties 141

C.1 Domestic Natural Gas Properties 143

List of Figures

3.1 CFR Engine Schematic 29
3.2 Fuelling System Schematic 31
3.3 Emissions Measurement System Schematic 33
3.4 Data Acquisition System Schematic 35
3.5 PCI-MIO-16E Wiring Diagram (Device 1) 36
3.6 PCI-MIO-16E Wiring Diagram (Device 2) 37
3.7 PCI-MIO-16E Wiring Diagram (Device 3) 38
3.8 Labview Execution Flowchart 39
3.9 MTS CAS Wiring Diagram 40

4.1 The Effect of Spark Timing on IMEP 48
4.2 Spark Timing Effects on Cylinder Pressure History 49
4.3 The Effect of Spark Timing on COV IMEP 51
4.4 The Effect of Spark Timing on Fuel Conversion Efficiency . . . 53
4.5 The Effect of Spark Timing on Exhaust Gas Temperature . . 54
4.6 The Effect of Spark Timing on Relative ISNO Emissions . . . 56
4.7 The Effect of Spark Timing on Relative ISCO Emissions . . . 58
4.8 The Effect of Spark Timing on Relative ISTHC Emissions . . 59
4.9 The Effect of EGR on IMEP 61
4.10 The Effect of EGR on MBT Spark Timing 65
4.11 The Effect of EGR on COV IMEP 66
4.12 The Effect of EGR on Cylinder Pressure History 67
4.13 The Effect of EGR on IMEP Distribution 68
4.14 The Effect of EGR on Fuel Conversion Efficiency 69
4.15 The Effect of EGR on Exhaust Temperature 70
4.16 The Effect of EGR on ISNO Emissions 72
4.17 The Effect of EGR on ISCO Emissions 74
4.18 The Effect of EGR on ISTHC Emissions 76
4.19 The Effect of H_2 Addition on Exhaust Diluted IMEP 79

4.20 The Effect of H_2 Addition on Exhaust Diluted MBT Spark Timing 82
4.21 The Effect of H_2 Addition on Exhaust Diluted COV IMEP . . 83
4.22 The Effect of H_2 Addition on Exhaust Diluted Cylinder Pressure History 84
4.23 The Effect of H_2 Addition on the Distribution of Exhaust Diluted IMEP 85
4.24 The Effect of H_2 Addition on Exhaust Diluted Fuel Conversion Efficiency 87
4.25 The Effect of H_2 Addition on Exhaust Diluted Exhaust Gas Temperature 88
4.26 The Effect of H_2 Addition on Exhaust Diluted ISNO Emissions 90
4.27 The Effect of H_2 Addition on Exhaust Diluted ISCO Emissions 91
4.28 The Effect of H_2 Addition on Exhaust Diluted ISTHC Emissions 93
4.29 The Effect of H_2 Addition on Exhaust Diluted $ISCO_2$ Emissions 94
4.30 The Effect of Upstream CO_2 Emissions on H_2 Supplemented Exhaust Diluted $ISCO_2$ Emissions 97

B.1 Air Mass Flow Meter Calibration 118
B.2 H_2 Mass Flow Meter Calibration 120
B.3 Natural Gas Mass Flow Meter Calibration 122
B.4 Intake Pressure Transducer Calibration 123
B.5 Exhaust Pressure Transducer Calibration 124
B.6 Dynamometer Load Cell Calibration 126
B.7 CLD Gas Analyzer Calibration 129
B.8 FID Gas Analyzer Calibration 131
B.9 NDIR Gas Analyzer CO_2 Calibration 134
B.10 NDIR Gas Analyzer CO Calibration 136
B.11 Paramagnetic Gas Analyzer Calibration 138
B.12 Rotary Encoder Alignment 140

NOMENCLATURE

ABDC ..... After Bottom Dead Center

AC ..... Alternating Current

ATDC ..... After Top Dead Center

BBDC ..... Before Bottom Dead Center

BMEP ..... Brake Mean Effective Pressure

BTDC ..... Before Top Dead Center

CA ..... Crank Angle

CAS ..... Combustion Analysis System

CFR ..... Cooperative Fuel Research

CLD ..... Chemiluminescent Detector

CNG ..... Compressed Natural Gas

COV ..... Covariant

ECM ..... Engine Control Module

EGR ..... Exhaust Gas Recirculation

EVC ..... Exhaust Valve Close

EVO ..... Exhaust Valve Open

FID ..... Flame Ionization Detector

FSO ..... Full Scale Operation

HC ..... Hydrocarbons

HEF ..... H_2 Energy Fraction

HVF ..... H_2 Volume Fraction

IMEP ..... Indicated Mean Effective Pressure

IS ..... Indicated Specific

IVC ..... Intake Valve Close

IVO ..... Intake Valve Open

LCA ..... Life Cycle Analysis

LHV ..... Lower Heating Value

LVDT ..... Linear Variable Differential Transformer

MBT ..... Maximum Brake Torque

NDIR ..... Non-Dispersive Infrared

NMEP ..... Net Mean Effective Pressure

NTP ..... Normal Temperature and Pressure

PFI ..... Programmable Function Input

PPR ..... Pulse per Revolution

RPM ..... Revolutions per Minute

RTD ..... Resistive Temperature Detector

SI ..... Spark Ignition

SR ..... Steam Reformation

SSD ..... Sample Standard Deviation

STP ..... Standard Temperature and Pressure

S_L ..... Laminar Burning Velocity

S_T ..... Turbulent Burning Velocity

TDC ..... Top Dead Center

THC ..... Total Hydrocarbons

VED ..... Volumetric Energy Density

WOT ..... Wide Open Throttle

WS ..... Water Shift

GREEK SYMBOLS

η_{fc} ..... Fuel Conversion Efficiency

η_{GR} ..... Global Reaction Efficiency

λ ..... Relative Air/Fuel Ratio

CHAPTER 1

INTRODUCTION

While the environmental impact of the automobile has long been regarded as a relevant and important research topic, increasingly strict environmental regulations and ever-expanding automobile use are both increasing the impetus of developing a cleaner and more efficient automobile.

The typical pollutants in the exhaust stream of a four-stroke spark ignition (SI) automobile engine include CO, hydrocarbons (HC) and NO. While CO and HC are typically indicative of incomplete combustion, NO is a result of the elevated in-cylinder temperatures associated with complete combustion. Such a dichotomy also extends to the manner in which the individual pollutants are abated. To convert CO and HC to CO_2 and H_2O, an oxidative environment is required. In an automotive exhaust system, this is typically achieved through the presence of excess O_2 and an oxidizing catalyst which promotes the rapid oxidation of both CO and HC. However, the conversion of NO to N_2 and O_2 requires a reducing environment, normally accomplished with an O_2 deficit and a reducing catalyst. As it is necessary for all *three* of CO, HC and NO to be abated simultaneously in an automobile, a *three*-way catalytic converter is used.

Three-way catalytic converters typically use a combination of Pt and Rh as catalysts to simultaneously oxidize CO and HC (Pt), and to reduce NO (Rh). An O_2 sensor in the exhaust system is used as feedback in rapidly varying the air/fuel ratio between lean (to promote oxidation) and rich (to promote reduction) air/fuel mixtures in order that all three pollutants are simultaneously abated. An O_2 storage compound (typically CeO_2) acts as a buffer, allowing for continued oxidation of CO and HC during periods of rich operation. The simultaneous peak conversion efficiency of a typical three-way catalytic converter is quite high, with conversion rates exceeding 95%

for each pollutant (Shelef and McCabe, 2000). However, this peak conversion efficiency is limited to within a fine margin of a stoichiometric air/fuel ratio, thus precluding the potential efficiency gain associated with a lean air/fuel ratio. As catalysis is presently the only way in which current and future emissions regulations can be met (Kašpar et al., 2003), there is a strong incentive to increase the efficiency of engines operating with a stoichiometric air/fuel ratio.

A method which is currently used to increase part-load efficiency and decrease engine-out NO emissions of stoichiometric SI engines is exhaust gas recirculation (EGR). By returning a fraction of the exhaust products to the intake of the engine, the thermodynamic properties of the intake mixture are altered, resulting in desirable changes to the emissions and efficiency characteristics of the engine. The decrease in energy density and increase in bulk heat capacity associated with an exhaust diluted mixture equates to lower peak in-cylinder temperatures and thus, decreased NO emissions (Quader, 1971). The decreased mixture energy content also results in a reduction in the amount of intake throttling required to maintain a partial load, thus improving part-load efficiency (Nakajima et al., 1981).

While EGR is an effective way to improve efficiency and decrease NO emissions, its use results in a decrease in mixture laminar burning velocity which is proportional to the amount of EGR employed (Stone et al., 1998). While most engine designs can tolerate EGR mass fractions of 30% (Heywood, 1988, page 103), the use of large EGR fractions is limited by the onset of excessive cycle-to-cycle variations in combustion associated with a significantly decreased laminar burning velocity. Thus, the extent of emissions and efficiency improvements associated with EGR are limited by a reduction in burning rate. While it is possible to increase the burning rate of an engine through changes in combustion chamber geometry, in-cylinder turbulence levels and spark plug location, it is more desirable to develop a simple and flexible means of increasing the burning rate which is easily adapted to a variety of engine operating conditions and which can be applied to a current engine platform. One such method involves the addition of H_2, a fuel with a laminar burning velocity roughly one order of magnitude higher than conventional automotive fuels (Karim, 2003).

This study investigates the potential of H_2 addition as a means of extending the EGR limit of a natural gas fuelled SI engine at full-load. In particular, this study aims to determine the following:

(1.) How much H_2 is required to maintain an original, undiluted level of combustion stability for a given EGR mass fraction?

(2.) What effect does H_2 addition have on full-load indicated specific NO (ISNO) emissions as the tolerable EGR mass fraction is extended?

(3.) How is full-load fuel conversion efficiency affected as the tolerable EGR mass fraction is extended?

(4.) How far can the indicated mean effective pressure (IMEP) be depressed, at full-load, as the tolerable EGR mass fraction is extended?

(5.) How are full-load indicated specific CO_2 ($ISCO_2$) emissions affected as the tolerable EGR mass fraction is extended?

(6.) How do the CO_2 implications of H_2 production affect total $ISCO_2$ emissions?

Prior to the development and execution of the experimental agenda, an extensive literature review was performed to become familiar with previous work on the topics of EGR and H_2 addition. The results of the literature review are presented in Chapter 2 as the motivation and underpinning for the remainder of the study. The effect of both EGR and H_2 addition are discussed in the context of changes in laminar burning velocity and thus, flame kernel development. The resulting changes in cycle-to-cycle combustion variation as a result of an extended (or reduced) flame kernel development time are also considered. Finally, previous studies in which H_2 or more typically, reformer gas, were used as a means of extending the EGR limit of an SI engine are considered.

An overview of the design, construction and use of the experimental system is given in Chapter 3. A description of the entire experimental system is provided in eight consecutive sections which describe the individual subsystems of the apparatus, including (in order): the engine intake, fuelling, EGR, ignition, cylinder pressure measurement, torque measurement, emissions measurement and data acquisition systems. Following this, details of both the engine startup and experimental procedures are described.

All pertinent experimental results are presented and discussed in Chapter 4. A discussion of the data post-processing techniques is first included to better understand the subsequent results. The experimental results are discussed in three sections, including: the effect of spark timing on engine

performance; the effect of EGR addition on engine performance; and the effect of H_2 addition on exhaust diluted engine performance. The initial tests on spark timing were performed to determine the effect of spark timing uncertainty on total measurement uncertainty. A rigorous description and explanation of the observed findings is included for each set of presented data.

A list of conclusions and an outline of possible extensions of this research are included in Chapter 5. Observed findings are discussed in the context of answering the questions posed at the beginning of this chapter. The impact of the research findings is also discussed in relation to the practical consequences and requirements of using H_2 addition to extend the EGR limit in a production automobile. A discussion of possible improvements to both the experimental apparatus and procedure are given along with future research possibilities which the present study can support.

A set of appendices is included which gives additional information about the equipment and data analysis procedures used in the study. Appendix A includes a detailed description of all equipment used in the study, including model numbers and serial numbers, as well as a description of the operating principles of the gas analyzers. Appendix B describes the procedures used to calibrate individual transducers and includes representative calibration plots for each instrument used. A detailed error analysis of both calibration procedures and individual measurements is also included. Appendix C lists the physical properties of the domestic natural gas supply used in the experiments. The calculation method for determining the relative air/fuel ratio (λ) based on measured intake air and fuel flow rates is also included. Finally, Appendix D describes the method that was used in calculating the EGR mass fraction based on the measured "dry" CO_2 mole fraction of the engine intake mixture.

CHAPTER 2

REVIEW OF RELEVANT LITERATURE

The unique physical properties of H_2 brand it a natural choice for promoting combustion in adverse conditions. As a result, H_2 supplementation has been studied extensively as a way to increase the robustness of spark ignition (SI) engine operation for both lean and dilute mixtures. A majority of previous research focussed on the use of H_2 in extending the lean limit. However, this study deals exclusively with the use of H_2 as a means of exhaust gas dilution limit extension. Hence, a review of the underlying mechanisms of both H_2 addition and exhaust gas dilution will first be presented so as to underpin the following critical review and discussion of studies in which H_2 is used specifically for dilute limit extension in SI engines.

2.1 The Effect of Mixture Composition on Combustion

Each measure of performance in an SI engine is wholly dependent upon the combustion quality in a given cycle, and upon the cycle-to-cycle variations in combustion quality. While there are many factors which may affect combustion quality in an SI engine, a large portion may be attributed to the laminar burning velocity of the in-cylinder mixture which governs the initial stages of flame growth.

The laminar burning velocity is a fundamental property of a combustible mixture which describes the rate at which reactants move normally through the combustion wave surface (Glassman, 1987) and is essentially a measure of the rate of heat and mass diffusion through the reaction zone in a flame. The laminar burning velocity largely affects the combustion mechanism in an SI engine. It is thus prudent to investigate the effects of a change in laminar burning velocity as a result of a change in mixture composition if

engine performance is to be predicted and understood.

2.1.1 Exhaust Gas Dilution

Exhaust gas dilution has a significant effect on the laminar burning velocity of a mixture, which has been illustrated in previous studies (Gat and Kauffman, 1980; Stone et al., 1998; Elia et al., 2001). Stone et al. (1998) measured the laminar burning velocity of CH_4-diluent-air mixtures within a spherical combustion chamber in a series of free-fall experiments. A near-zero gravity environment was used to negate flame buoyancy effects, to minimize heat transfer to the chamber walls and to maximize the amount of useable data from each experiment. A diluent consisting of 85% N_2 and 15% CO_2 was used because it simulated both the molar mass and heat capacity of combustion products. A comprehensive set of least squares correlations was determined for various initial conditions and mixture compositions. At a stoichiometric equivalence ratio and initial conditions of 298 K and 1 atm, the addition of a 20% diluent fraction resulted in a decrease of laminar burning velocity of 65% - from 37.5 cm/s at an undiluted condition to 13 cm/s for a 20% dilute fraction.

Elia et al. (2001) performed further experiments in a spherical combustion chamber to determine the laminar burning velocity of CH_4-air-diluent mixtures. Correlations for burning velocity were determined which extended the range of unburned gas pressures and temperatures previously used by Stone et al. (1998). The addition of a 15% fraction of simulated combustion products (86% N_2 and 14% CO_2) to a stoichiometric CH_4-air mixture with initial conditions of 298 K and 1 bar, resulted in a decrease in laminar burning velocity of 55% - from 37.5 cm/s to 17.0 cm/s.

Beyond a decrease in laminar burning velocity, the use of exhaust gas recirculation (EGR) results in other changes in combustion which can affect the performance of an SI engine. Gat and Kauffman (1980) performed a series of experiments in a cylindrical combustion chamber to determine the effect of simulated exhaust gas on both laminar and turbulent burning velocities, ignition energy, heat flux and flame quenching behaviour of CH_4-air mixtures. It was shown that at a given turbulence intensity, the addition of simulated exhaust diluent results in a significant increase in the ratio of turbulent to laminar burning velocity (S_T/S_L), thus indicating that the addition of diluents primarily affects laminar burning velocity. The temperature time-history of an instrumented quenching surface within the combustion

chamber allowed for the calculation of heat flux and heat transfer, both of which decreased with diluent addition, mainly as a result of decreased adiabatic flame temperature. Further measurements showed that an increase in diluent fraction also causes increases in both flame quenching distance and the minimum energy required for ignition.

With the effect of simulated exhaust gas products on the combustion mechanism of CH_4-air determined for single events within constant volume combustion chambers, this knowledge can be applied in understanding phenomena in SI engine experiments. The decrease in laminar burning velocity, associated with an increase in exhaust gas dilution, has a strong effect on the rate and variability of the early phases of flame development in an SI engine. Matekunas (1983) performed a series of experiments on a single-cylinder research engine equipped with a transparent piston crown to determine the various modes of cycle-to-cycle variations in pressure development. The contribution of several parameters were investigated, including the amount of swirl production (achieved through the use of shrouded intake valves and specially designed intake ports), spark plug location and equivalence ratio. Through a combination of in-cylinder cinematography and pressure measurement it was determined that, as combustion quality approached the misfire limit, the rate of flame kernel growth is the governing factor in cycle-to-cycle variations in combustion. As a flame kernel is developing, it is vulnerable to local flow conditions which may convect the flame kernel toward the cylinder wall, resulting in increased heat loss from the flame and a reduction in the subsequent rate of flame propagation, typically due to an opposition from in-cylinder flows. An increase in flame kernel development time is then equatable to an increased likelihood of cycle-to-cycle variations in pressure development.

The primary factor which governs the rate of flame kernel development is the laminar burning velocity of the mixture within the vicinity of the spark plug electrode. It is during this time that the in-cylinder eddies are large in comparison to the flame kernel and do not distort the flame front to enhance its burning velocity, as in turbulent combustion (Lancaster et al., 1976). Thus, the reduction in laminar burning velocity associated with the use of exhaust gas dilution, as discussed by Gat and Kauffman (1980), Stone et al. (1998) and Elia et al. (2001), is presumed to cause an increase in cycle-to-cycle pressure development variations in an SI engine.

This effect is compounded when the variation in mixture composition within the spark plug gap is considered. Matsui et al. (1979) developed an

unobtrusive method of measuring the mixture composition within the spark plug gap for successive engine cycles in a running engine. Through the use of a rapid-acting solenoid needle valve, mixture samples were drawn from within the spark plug gap and transferred, via a N_2 flow line, to a quick response emissions test bench that was customized to be used with small gas samples. It was determined that an increased exhaust gas dilution fraction resulted in a marked rise in cycle-to-cycle variation in both the total hydrocarbon (THC) and CO_2 concentrations within the spark gap. As equivalence ratio and CO_2 dilution are both known to affect the laminar burning velocity of a CH_4-air mixture (Stone et al., 1998), it is supposed that this mechanism further increases variation in cycle-to-cycle pressure development as the EGR fraction is increased.

The effect of EGR on combustion stability in an SI engine has been studied directly by Kuroda et al. (1978). A set of experiments was performed on an instrumented cylinder of a production four-cylinder SI engine. The cylinder was equipped with a pressure transducer and four ionization detectors which were used to detect the arrival of the flame front at the cylinder wall. The addition of EGR was found to increase covariant indicated mean effective pressure (COV IMEP), hydrocarbon exhaust emissions and fuel consumption. A set of four combustion patterns was developed to describe the quality of combustion based on the indicated mean effective pressure (IMEP), the burn duration and ionization sensor data. The four combustion patterns are given as normal burn, slow burn, partial burn and misfire. It was determined that the addition of EGR always resulted in the appearance of 5% of total engine cycles being "slow burn" before additional EGR caused partial burn or misfire cycles. The use of a dual spark plug configuration was shown to greatly increase the EGR limit of the engine, resulting in greater improvements in NO emissions and fuel economy. Based on the previous discussion of flame kernel development, this is expected as a faster burning engine allows for a greater spark retard at a comparable dilution fraction, resulting in unburned gas conditions which are more conducive to flame initiation.

2.1.2 H_2 Addition

H_2 addition is another method that has been investigated as a means to improve flame kernel development and thus reduce cycle-to-cycle variations in pressure development.

The effect of H_2 addition to the laminar burning velocity of CH_4-air mix-

tures has been thoroughly investigated (Milton and Keck, 1984; Yu et al., 1986). Milton and Keck (1984) measured the laminar burning velocities of stoichiometric CH_4-air and H_2-air (among other) mixtures at various initial pressures in a constant volume spherical combustion bomb. As all experiments took place within a constant volume combustion bomb, the burning velocities at elevated pressures and temperatures were also measured. The burning velocity of H_2-air mixtures was given as being approximately one order of magnitude higher than that of CH_4-air. The laminar burning velocity of stoichiometric CH_4-H_2-air was measured for a H_2/CH_4 mole ratio of 2/1. The results showed that the burning velocity of the H_2-CH_4-air mixture was significantly higher than for CH_4-air, but lower than if the burning velocity was predicted based on the mole ratio and burning velocities of individual fuels within the mixture. A stoichiometric H_2-CH_4 mixture with a H_2/CH_4 ratio of 2/1 and initial conditions of 300 K and 1 atm resulted in an increase of laminar burning velocity of more than 200% - from 35 cm/s for stoichiometric CH_4, to 110 cm/s for the H_2/CH_4 blend.

Yu et al. (1986) further investigated the effect of adding different amounts of H_2 on the laminar burning velocity of CH_4-air (among other) mixtures at various equivalence ratios. Burning velocities were measured using a symmetrical counterflow arrangement in which flame stretch and heat loss are negated. The amount of H_2 added was given as a relative ratio and the measured laminar burning velocity at different equivalence ratios was related to this relative H_2 ratio. At a given equivalence ratio, the relative amount of H_2 added is linearly correlated to an increase in laminar burning velocity. For a given H_2 ratio, the laminar burning velocity peaks at an approximately stoichiometric equivalence ratio.

As discussed in Section 2.1.1, the laminar burning velocity governs the rate of flame kernel development, which has been shown to be directly related to cycle-to-cycle variation in pressure development for an SI engine operating near the misfire region. It is presumed that the increase in laminar burning velocity associated with H_2 addition should reduce these cycle-to-cycle variations in pressure development if misfire is incipient.

Heywood and Vilchis (1984) investigated the flame development of both H_2-air and C_3H_8-air flames using schlieren photography with a quartz walled square piston single-cylinder research engine. Testing for each fuel was conducted with the same operating and mixture conditions to isolate and study the effect of fuel chemistry on flame development and propagation. The H_2-air flames were shown to develop significantly faster, with a uniformity in

flame size, position and reaction zone distribution between cycles. Whereas the C_3H_8-air flames displayed significant cycle-to-cycle variations in each of these attributes. The effects of in-cylinder flow are visible in the photographs of C_3H_8-air flame development, with the center of the flame being convected away from the spark electrode in several instances.

A study on the effect of H_2 addition on flame development in an SI engine was performed by Rauckis and Mclean (1979). Using cylinder pressure data from a single-cylinder cooperative fuel research (CFR) engine operating with various fractions of H_2 and indolene, the effect of H_2 addition on the various stages of flame growth and propagation was investigated. Flame growth and propagation was divided into three categories based on the mass fraction burned: kernel growth duration (0-2% burned); flame development duration (2-10% burned); and combustion duration (10-90% burned). It was determined that H_2 addition resulted in a significant reduction in kernel growth duration at all equivalence ratios, with smaller (but still significant) reductions in both flame development duration and combustion duration. At an equivalence ratio of 1.0, a 15% H_2 energy fraction (HEF) resulted in a 28% decrease in duration of flame kernel growth, from 9.9 to 7.2° CA. This result is supported by previous studies which illustrated an increase in laminar burning velocity with the addition of H_2 (Milton and Keck, 1984; Yu et al., 1986) and by Heywood and Vilchis (1984) who showed the difference in flame development between H_2 and hydrocarbon fuels using schlieren photography.

2.2 H_2 Addition to Extend EGR Limit of an SI Engine

Having separately established the effects of both exhaust dilution and H_2 addition on flame development (and thus cycle-to-cycle variations in pressure development), the discussion turns to previous studies that used H_2 as a means of accommodating increased exhaust gas dilution fractions in SI engines.

A majority of previous studies of H_2 addition in SI engines focussed on lean (rather than dilute) limit extension. The reader can refer to review papers by Jamal and Wyszynski (1994) and Akansu et al. (2004) for further information on this topic. While a lean mixture can result in greater fuel economy increases when compared to exhaust diluted mixtures (Lumsden et al., 1997), its use precludes the application of (and increased robustness associated with) a three-way catalytic converter.

Smith and Bartley (2000) investigated the effect of H_2-rich "synthesis

gas" addition on the performance and EGR limit of a single-cylinder research engine. All tests were conducted at 1800 RPM, 11.0 bar brake mean effective pressure (BMEP) and wide open throttle (WOT) (load was maintained through supercharging). The synthesis gas that was produced had the following composition based on wet mole fractions: H_2 (29.7%), CO (15.1%), H_2O (3.4%), CO_2 (3.3%), CH_4 (1.2%), O_2 (0.0%) and N_2 (47.3%). The amount of synthesis gas used in the experiments was quantified as the mass fraction of total natural gas consumption that was used by the catalyst in its production. A 40% synthesis gas fraction resulted in a 44% increase in EGR tolerance - from 27% (for a baseline case) to 39%. The use of synthesis gas was not shown to noticeably affect indicated thermal efficiency for EGR fractions beyond 15%. As expected, an increased fraction of synthesis gas also resulted in a significant decrease in ignition delay (0-10% mass fraction burned) - especially at increased EGR fractions. The effect was present, although not as pronounced, for the remaining 10-90% mass fraction burn duration. The extension in EGR limit afforded by the synthesis gas resulted in a 40% decrease in NO_x emissions - from 680 to 156 ppm for a 40% synthesis gas fraction. Hydrocarbon emissions were also shown to decrease with an increase in synthesis gas while CO emissions were mostly unaffected. However, for a combination of high EGR and synthesis gas fraction, the significance of the CO present in the synthesis gas became apparent with a noticeable increase in CO emissions. While no limit was placed on what was considered "acceptable combustion quality" in this study, the COV IMEP remained at approximately 2% for all tests. As a result of there being no formal limit on combustion stability, it is noted that the EGR limits are likely somewhat higher than those reported in this study.

Allenby et al. (2001) studied the effect of both H_2 and simulated reformer product addition on the extension of the EGR limit of a single-cylinder SI research engine. Experiments were performed at three operating conditions: 1500 RPM at 2 bar IMEP; 2000 RPM at 2 bar IMEP; and 2000 RPM at 4 bar IMEP. At each condition, EGR and H_2 were added in succession to follow a constant COV IMEP of 5%, which was considered to be an acceptable combustion stability. The addition of H_2 required to extend the EGR limit was shown to be strongly dependent upon load and less so on engine speed. At 2000 RPM and 2 bar IMEP, H_2 addition of 22% resulted in a five fold increase in EGR limit - from 5 to 30%. When the load was increased to 4 bar at 2000 RPM, only an 11% H_2 fraction was required to sustain the same 30% EGR fraction. As expected, the larger EGR fractions supported

by H_2 addition resulted in further decreases in NO emissions. Results reported for hydrocarbon emissions show no discernible trend. A large portion of this study (which is not discussed here) was devoted to evaluating the performance of a reformer catalyst that was used to produce H_2-rich gas.

Quader et al. (2003) further studied the effect of both simulated and actual gasoline reformate addition on the lean and dilute limit of a single-cylinder SI research engine. The volumetric composition of the simulated reformer gas was 21% H_2, 24% CO and 55% N_2. All tests were performed at 1330 RPM, maximum brake torque (MBT) spark timing, with reformate/gasoline energy fractions of 0, 15, 30, 50 and 100%. Both the lean and dilute limits were bracketed using a series of equivalence ratios and EGR fractions at a value of COV IMEP no higher than 3%. Both light load (216 kPa NMEP) and heavy load (540 kPa NMEP) conditions were tested.

An increase in reformate fraction to 100% resulted in a 44% lean limit extension (from $\lambda = 1.47$ to $\lambda = 2.63$) and a 115% increase in the dilute limit (from 17% to 37%). The extension in both lean and EGR limits afforded by a 100% reformate fraction resulted in a one order of magnitude reduction of NO emissions in both cases. However, at a given relative dilution, the use of EGR resulted in greater decreases in NO emissions then for a lean mixture. EGR dilution also resulted in a slight decrease in hydrocarbon emissions while a lean mixture showed no noticeable trend. As expected, the use of a 100% reformate fraction resulted in near-zero hydrocarbon emissions in both cases. CO emissions remained relatively unaffected in both cases, except for large reformate fractions, where the CO contained in the fuel became apparent in the exhaust emissions. The thermal efficiency remained constant with EGR addition, while a lean mixture resulted in an approximate 5 to 10% gain in efficiency (when compared to EGR). Reformate addition caused a decrease in both flame initiation (0-10% mass fraction burned) and flame propagation (10-90% mass fraction burned) at a given relative dilution for both EGR and lean mixtures. However, the total burn duration was much higher for exhaust diluted mixtures than for lean mixtures. The total burn duration at the EGR limit *increased* from 86° CA for gasoline to 90° CA for 100% reformate, while *decreasing* by a similar amount for lean mixtures. All discussed results were similar for the high load (540 kPa NMEP) case, except for the following differences: a higher baseline dilution tolerance for both EGR and lean mixtures; higher thermal efficiency; and the requirement for supercharging to obtain the required load with 100% reformate.

Conte and Boulouchos (2004) performed a comprehensive study on the

effect of reformer gas addition on the performance, lean limit and dilute limit extension of an SI research engine. All tests were performed at 2000 RPM, 200 kPa and MBT spark timing. Simulated bottled reformer gas with the same composition used by Quader et al. (2003) (i.e. 21% H_2, 24% CO and 55% N_2) was used for all tests. Various reformate/gasoline energy fractions were tested at each of three operating points: $\lambda = 1.0$ with no EGR; $\lambda =$ lean limit with no EGR; and $\lambda = 1.0$ at EGR limit - only the results from the latter two cases will be discussed here. The limit for combustion stability in this study was chosen to be 10% COV IMEP.

As expected, an increase in reformate fraction resulted in extensions of both the lean and dilute limits. A 100% reformate fraction gave a 92% extension in lean limit (from $\lambda = 1.12$ to $\lambda = 2.15$) and an approximate ten-fold increase in EGR limit (from 5 to 51%). While the percentage values of both lean and dilute limit extension are much higher than those presented by Quader et al. (2003), this can be explained by observing two factors: first, the definitions of combustion stability vary from 10% COV IMEP, in the present study, to a value of 2% COV IMEP used by Quader et al. (2003); and second, the baseline values of both lean and EGR limit with no reformate are much lower in the present study, which may be attributed to the excessive valve overlap (and retained residual gas fraction) that is characteristic of the engine used in the study.

The amount of time required for flame initiation (0-5% mass fraction burned) and propagation (5 to 90% mass fraction burned) is shown to remain relatively constant at both the lean and EGR limit with increasing reformate fraction. As discussed previously (Matekunas, 1983), the mixture laminar burning velocity is the primary factor in governing cycle-to-cycle variations when misfire is incipient. Hence, at a constant combustion stability of 10% COV IMEP, the mixture laminar burning velocity is likely staying constant with increasing amounts of both reformate and excess air or EGR, thus resulting in a constant duration of all combustion phases. Specific CO emissions were shown to increase as the lean limit was extended, likely due to a decrease in post-combustion oxidation resulting with falling exhaust temperatures. CO emissions remained relatively constant for EGR dilution. As expected, both hydrocarbon and NO emissions were shown to significantly decrease with an increasing reformate fraction in both lean and EGR dilution cases, due (respectively) to a direct displacement of hydrocarbon fuel and a reduction in peak combustion temperature. As was also expected, EGR dilution had a greater effect than a lean mixture in reducing NO emissions for all

but a 100% reformate fraction where they were equally effective. Some basic efficiency calculations were performed to determine the global efficiency of a reformer and SI engine system. With a presumed reactor efficiency of 0.85 (based on the lower heating value (LHV) of the inlet and outlet streams), a maximum global efficiency gain of 13% can be obtained at both the lean and EGR limit with a 100% reformate fraction.

2.3 Summary

A discussion of previous studies has shown that, when misfire is incipient, the primary cause of cycle-to-cycle variations in pressure development is a decreased mixture laminar burning velocity. The rate of flame kernel development is governed by the laminar burning velocity and thus, a decrease in laminar burning velocity translates to an increased likelihood of the flame kernel being convected away from the spark plug electrode, resulting in varied heat transfer and flame development. Investigations using both constant volume combustion bombs and counterflow flame configurations have determined that the addition of exhaust gas diluents results in a decreased laminar burning velocity whereas increased laminar burning velocity is achieved through H_2 addition. The relation between laminar burning velocity and cycle-to-cycle variations in pressure development was established in single-cylinder SI engine experiments where the effects of EGR and H_2 addition were evaluated individually. The addition of EGR was shown to increase cycle-to-cycle variability in pressure development while H_2 addition decreased this variability.

Studies in which H_2 was investigated as a means of extending the dilute limit of an SI engine were also discussed. All but one study focussed on the use of H_2-rich simulated reformer gas as a means of dilute limit extension. In general, the addition of either H_2 or a H_2-rich gas was shown to extend the dilute limit, allowing for greater decreases in NO emissions while maintaining or slightly improving thermal efficiency.

While previous studies have been performed using simulated reformer gas, the presence of both CO and N_2 result in different emissions and dilution characteristics when compared to neat H_2 addition. Furthermore, the use of onboard reforming, while championing development of H_2-compatible SI engines, does little to promote the development of a H_2 infrastructure. Thus, the current study is being undertaken to demonstrate the effect of neat H_2 addition on the emissions and performance implications of an ex-

tended dilution limit in an SI engine. This study may be used to underpin the investigations of reformer gas addition and to promote the use of H_2-blended vehicle fuels as a means of significantly reducing emissions while maintaining or improving efficiency.

Chapter 3

Experimental System and Procedure

The aim of this study was to determine the effect of H_2 addition on the exhaust gas dilution limit of a spark ignition (SI) engine. Engine performance was quantified using four parameters: output torque, combustion stability, fuel conversion efficiency (η_{fc}) and exhaust emissions. Based on these metrics, a single-cylinder cooperative fuel research (CFR) engine was suitably modified and instrumented for this investigation. Several safety features were incorporated into the experimental design to account for the unique physical properties of H_2. Prior to the execution of any experiments, all instruments were carefully calibrated to ensure reliable results.

This chapter focuses on a description of the experimental design and the test procedures employed in determining the effects of H_2 addition and exhaust gas recirculation (EGR) on engine performance. Section 3.1 includes a summary of eight individual subsystems of the experimental apparatus, including (in order): engine intake, fuelling, EGR, ignition, cylinder pressure measurement, torque measurement, emissions measurement and data acquisition systems. An overview of the experimental procedures used in conducting this study is given in Section 3.2.

3.1 Instrumented Engine

All experiments were conducted on an instrumented single-cylinder CFR engine, the specifications of which are given in Table 3.1. A schematic of the CFR engine and all associated modifications and instrumentation is given in Figure 3.1.

Table 3.1: CFR Engine Specifications

Engine Model	Waukesha CFR
Engine Type	Water cooled, four stroke, single-cylinder, SI
Displacement [cc]	612
Bore [mm]	82.6
Stroke [mm]	114.3
Compression Ratio	11.5
Combustion Chamber	Disc cylinder head, flat-top piston
Intake Valve [mm][1]	31.8
Exhaust Valve [mm]	31.8
Valve Timing	
EVO	40 [°BBDC]
IVO	10 [°ATDC]
EVC	15 [°ATDC]
IVC	34 [°ABDC]

[1] Intake valve is unshrouded

3.1.1 Intake System

The intake system was designed with three factors in mind: the accurate and continuous measurement of intake air mass flow rate and temperature, intake pressure and EGR mass fraction; promotion of mixing between external EGR and intake air; and incorporation of suitable safety features to accommodate H_2 fuel usage.

At the upstream side of the intake system, an inlet filter (3.1-1)[1] was installed to prevent contaminants from reaching downstream components. A thermal mass flow meter (3.1-2) was used to measure the mass flow rate of intake air. Details of the mass flow meter calibration, a typical calibration plot and a differential error analysis are given in Appendix B. As is typical with industrial instrumentation, the air mass flow meter produced a current output of 4-20 mA. To obtain the necessary voltage signal, a known resistance (250 Ω) was applied across the meter output leads and the voltage across these leads measured.

To prevent upstream convection of the inherent intake flow fluctuations

[1]Parenthesized numbers refer to the figure number in which the component appears and the individual component label within that figure.

of a single-cylinder engine, a 205 litre pulsation barrel (3.1-3) was installed downstream of the intake air mass flow meter. The temperature of the intake air stream was measured downstream of the pulsation barrel using a 1.6 mm diameter sheathed and ungrounded type-T thermocouple (3.1-4).

While this investigation only focussed on testing at wide open throttle (WOT), a 12.7 mm butterfly valve (3.1-5) was incorporated as an intake throttling device for two reasons: first, to allow for future part-load testing; and second, to permit a means of quickly shutting off air flow to the engine if required.

An intake plenum (3.1-6) was constructed out of a length of 90 mm diameter schedule 40 carbon steel pipe. To promote mixing of EGR and intake air, the EGR was introduced directly downstream of the throttling valve. The EGR-air sample was then drawn from the downstream side of the intake plenum (3.1-33), at which point it was presumed that adequate mixing of the EGR and intake air had taken place. Further details of the EGR system, including measurement and calculation procedures, are given in Section 3.1.3. The pressure of the intake plenum was measured using a Validyne diaphragm differential pressure transducer (3.1-7) with a range of ± 138 kPa. The calibration procedure, a representative calibration plot and a differential error analysis of this pressure transducer are all included in Appendix B. To minimize the risk of H_2 ignition within the intake system, the plenum was mounted at a positive angle to ensure that any fuel would remain close to the intake port of the running engine. Furthermore, the downstream joint of the intake plenum was designed to minimize the resulting pressure rise if any fuel were to ignite within the intake system.

Both H_2 and natural gas were introduced directly upstream of the engine intake port using horizontally opposed Bosch electronic natural gas fuel injectors (3.1-23, 3.1-24). Further details of the fuelling system are given in Section 3.1.2. The temperature of the air-fuel-EGR mixture was then measured immediately upstream of the intake port with a 1.6 mm diameter sheathed and ungrounded type-T thermocouple (3.1-8).

Prior to the execution of any experiments, the entire intake system was checked for leaks. Because it is difficult to detect a vacuum leak while the engine is running, the intake system was pressurized and checked for leaks while the engine was shut off. All temperature, pressure and sample ports on the intake system were plugged and the entire intake system was pressurized to approximately 15 kPa. The system was inspected using a leak detection solution and any leaks were remedied. The system was again pressurized and

it was determined that there were no further leaks.

3.1.2 Fuelling System

The fuelling system was designed to allow computer control and measurement of the individual mass flow rates of H_2 and natural gas. Several safety features were incorporated into the fuelling system to account for the use of high-pressure H_2 and natural gas. A schematic of the fuelling system is given in Figure 3.2.

Both H_2 and natural gas were taken from pressurized cylinders (3.2-1, 3.2-10). Industrial grade H_2 was obtained from Praxair while the natural gas cylinder was filled from a high pressure domestic natural gas supply. A detailed description of the physical properties of both fuels is given in Appendix C. Both natural gas and H_2 are regulated to a pressure of 550 kPa - natural gas via an electronic two-stage pressure regulator (3.2-11) and H_2 via a manual two-stage diaphragm pressure regulator (3.2-2) prior to usage. To prevent the unintended flow of H_2 and natural gas, each was routed through normally closed solenoid shut-off valves (3.2-3, 3.2-12). Downstream of the shut-off solenoid valves, both the temperature and pressure of the gases are measured using 1.6 mm diameter sheathed and ungrounded type-T thermocouples (3.2-5, 3.2-14) and bourdon tube pressure gauges (3.2-4, 3.2-13). The mass flow rate of each gas was measured using thermal mass flow meters (3.2-6, 3.2-15). The calibration procedure, a typical calibration plot and a differential error analysis for each thermal mass flow meter are all given in Appendix B. To prevent the mass flow meters from being affected by upstream convection of flow fluctuations, plenums (3.2-7, 3.2-16) were placed downstream of each flow meter. Ball valves were then installed downstream of each fuel plenum (3.2-8, 3.2-17) to provide a rapid means of shutting off the fuel supply when desired. Beyond the ball valves, each fuel was routed directly to respective electronic fuel injectors (3.1-23, 3.1-24) using braided stainless steel flexible tubing.

All control of fuelling was accomplished with a custom single-cylinder, two-fuel engine control module (ECM) based on crankshaft position as determined by a variable reluctance sensor (3.1-27) and a 36-1 tooth crankshaft mask. The control of individual injector pulse width and thus fuel mass flow rate was achieved by updating the table values within the ECM via a personal computer.

Prior to engine operation, the entire fuel system was purged with N_2 to

maintain O_2 levels below the rich flammability limits of each fuel. The fuel system was repeatedly purged with N_2 whenever components needed to be removed for service or replacement, or for any other reason where it was believed that O_2 may have entered the fuel system.

To prevent the accumulation of H_2 within the crankcase, a pressurized supply of N_2 (3.1-32) was introduced to the crankcase and the exiting gases (3.1-35) were monitored to ensure that the O_2 content remained below the rich flammability limit of H_2.

3.1.3 EGR System

The EGR system was designed to ensure that a well-mixed air-EGR mixture was achieved prior to both the measurement and consumption of the intake mixture. To accomplish this, a portion of the hot exhaust products was recycled to the upstream end of the intake plenum, directly downstream of the throttle valve. The temperature of the EGR was initially reduced using a shell and tube heat exchanger (3.1-19) which was connected to the domestic hot water supply. The temperature of the cooled EGR was measured immediately downstream of the heat exchanger using a 1.6 mm diameter sheathed and ungrounded type-T thermocouple (3.1-20). To accurately control the amount of EGR inducted into the intake plenum, both small and large gate valves (3.1-21, 3.1-22) were installed in parallel upstream of the intake plenum.

To measure the mass fraction of EGR, a gas sample was drawn from the downstream end of the intake plenum (3.1-33), at which point it was presumed that sufficient mixing between the air and exhaust streams had taken place. Based on the measured dry CO_2 mole fraction, the mass fraction of EGR was calculated. A detailed example of this calculation is given in Appendix D. Further details of the emissions measurement system are also included in Section 3.1.7.

While the residual fraction (internal EGR) was not measured directly, the conditions of the exhaust products were monitored to show that differences in residual fraction between experiments were negligible. The exhaust gas temperature was measured directly downstream of the exhaust port using a 1.6 mm diameter sheathed and grounded type-J thermocouple (3.1-14) while the exhaust pressure was measured using a Validyne diaphragm differential pressure transducer (3.1-15) with a range of ± 69 kPa. The calibration procedure, a representative calibration plot and a differential error analysis of

this pressure transducer are all included in Appendix B.

3.1.4 Ignition System

The original 110 volt AC ignition system of the CFR engine was used for all experiments. The ignition coil (3.1-10) was relocated so that a minimal length of shielded wire was required to connect it to the spark plug (3.1-12). This was done to minimize the electrical noise transmitted to the surrounding instrumentation and data acquisition systems during spark discharge.

The spark plug used was an NGK AB-6, the gap of which was set to 0.64 mm. This spark plug is considered to be in the middle of the "heat" scale, which describes the temperature that the insulator tip maintains during engine operation. While a "cool" spark plug may prevent the pre-ignition of fuels with a propensity to do so (e.g. H_2), it also inhibits flame kernel development through increased heat transfer. Thus, a spark plug in the middle of the heat scale was chosen to balance the opposing requirements of H_2 addition and exhaust gas dilution.

The spark timing was adjusted using a 12 volt automotive inductive timing light and the manual spark adjustment located on the side of the CFR engine.

3.1.5 Cylinder Pressure Measurement

All cylinder pressure measurements were obtained with a Kistler model 6043A water cooled piezoelectric pressure transducer (3.1-13). The pressure transducer was mounted in an access port, at the top of and normal to the cylinder wall. The cylinder pressure transducer was calibrated over a range of 0 to 50 bar by the manufacturer. Further details on the accuracy and calibration of the cylinder pressure transducer are included in Appendix B.

A closed-loop cooling system was designed, based on the work of Atkins (2004), especially for the pressure transducer using a water tank, vinyl tubing and a diaphragm pump which met the necessary flow requirement of 0.5 LPM. As the output of the pressure transducer was in units of pC/bar, the use of an MTS model 1104CA charge amplifier was necessary to obtain a voltage output.

To relate the cylinder pressure to crankshaft position, a BEI rotary incremental encoder with a resolution of 0.1° CA was mounted to the crankshaft of the engine. The output of both the rotary encoder and the cylinder pres-

sure charge amplifier were connected to an MTS combustion analysis system (CAS), which processed the cylinder pressure and crankshaft position measurements in real-time.

Prior to performing any experiments, it was necessary to align the absolute position of the crankshaft with the index pulse of the rotary encoder, in order that the MTS CAS have a reference of absolute crankshaft position. A detailed overview of this alignment procedure and a representative calibration plot is given in Appendix B. Further details of data acquisition with the MTS CAS system are given in Section 3.1.8.

3.1.6 Torque Measurement

The power output of the engine was absorbed with an eddy current dynamometer (3.1-30). In order to directly measure the brake torque of the engine, an Eaton model 3168 load cell (3.1-31) was used to measure the force generated at a measured distance from the centerline of the dynamometer. The calibration procedure of the load cell, a representative calibration plot, the technique used to determine the centerline distance and a differential error analysis are all included in Appendix B.

3.1.7 Emissions Measurement

The emissions measurement system was designed to accurately determine gas compositions based on samples from the intake plenum and exhaust system. The results of this analysis are necessary in quantifying several important measures of engine performance. The EGR mass fraction is determined based on the CO_2 concentration in the intake plenum sample, whereas both pollutant emissions and a confirmation of mixture stoichiometry and fuel composition can be determined from an analysis of the exhaust products. A schematic of the emissions measurement system is given in Figure 3.3.

Both the intake plenum and exhaust product samples (3.1-33, 3.1-34) were routed to the emissions analyzers via 6 mm stainless steel and teflon tubing. To desiccate the samples prior to reaching the emissions analyzers, they were first routed through shell-and-tube heat exchanges (3.3-3, 3.3-4) which were supplied with domestic cold water. Any condensed water was captured in glass beakers (3.3-5, 3.3-6). Diaphragm vacuum pumps (3.3-7, 3.3-8) were then used to transport the gas samples to the various gas analyzers 3.3-15 to 3.3-19). Solenoid valves (3.3-9, 3.3-10) were installed and connected such that

they were open when the respective upstream vacuum pump was running. A three-way switch was connected to the vacuum pump-solenoid valve circuit which allowed for the independent sampling of either the intake or exhaust mixture. As several of the gas analyzers required a specific sample flow rate, needle valves (3.3-12 to 3.3-14) were installed upstream of the gas analyzers to control individual flow rates. A bypass valve (3.3-26) was also used to route excess sample gases to the building exhaust system.

A chemiluminescent detector (CLD) (3.3-15) was used to measure the concentration of NO in the gas sample. The CLD analyzer required that the gas sample inlet pressure be between 40 and 170 kPa and the flow rate be between 2 and 4 LPM. Hydrocarbon emissions were measured with a flame ionization detector (FID) (3.3-16). Similar to the CLD analyzer, the FID analyzer required that the gas inlet pressure be between 40 and 170 kPa with an inlet flow rate of 2.5 to 5.5 LPM. The FID analyzer can be used to measure either total hydrocarbon (THC) emissions or CH_4 emissions; THC emissions are measured in this study. Both CO_2 and CO concentrations in the gas sample were measured using a non-dispersive infrared (NDIR) analyzer (3.3-18). The NDIR analyzer requires that the sample flow rate be between 0.5 and 2 LPM, with no specification on required sample pressure. Finally, the O_2 concentration of the gas sample was determined using a paramagnetic detector (3.3-19). The paramagnetic detector required that the sample flow rate be 1 LPM with no requirement on sample pressure. Detailed descriptions of the operating principles of each gas analyzer are given in Appendix A.

Prior to the start of any experiments, the gas analyzers were calibrated using mixtures of bottled calibration gases (3.3-22 to 3.3-25) which were blended to the appropriate concentrations using a multi-gas calibrator (3.3-20). Further details of the calibration procedure of the gas analyzers, representative calibration plots and differential error analyses are all given in Appendix B. The warm-up and operating procedures of the gas analyzers are discussed in Section 3.2.

3.1.8 Data Acquisition System

The data acquisition system consisted of two separate subsystems: a Labview system which was used to measure and record data which required a moderate sampling rate (i.e. < 10 kHz); and an MTS CAS which was used to measure cylinder pressure data at 0.1° CA intervals over consecutive engine cycles in real-time. Both Labview and MTS CAS systems were interfaced to a personal

computer to display and store the experimental results. A schematic of the entire data acquisition system is included in Figure 3.4.

3.1.8.1 Labview System

The Labview data acquisition system was used to obtain all measurements save cylinder pressure. All signals were connected to three 12-bit multifunction PCI data acquisition boards via shielded connector blocks, as shown in Figure 3.4. Wiring schematics for each connector block are given in Figures 3.5, 3.6 and 3.7.

While most measurements were taken with a temporally based sample rate, the inherent gas exchange fluctuations of a single-cylinder engine required that some signals be measured with a sample rate based on crankshaft position, thus allowing for accurate and consistent averaging over a given number of engine cycles. Figure 3.5 shows the wiring schematic of the shielded connector block which was used to obtain measurements based on crankshaft position. The 0.1° CA resolution afforded by the crankshaft encoder was deemed excessive for these measurements and so a "decade counter" integrated circuit was used to supply a 1° CA pulse train to the appropriate programmable function input (PFI) of the connector block (pin 38). To trigger a sequence of measurements based on crankshaft position, a one pulse-per-revolution (PPR) signal was taken from the crankshaft encoder and connected to PFI0 (pin 11) of the connector block.

Bias resistors were used to allow for the differential measurement of floating ground signals while rejecting common mode voltage. The value of bias resistors (10 kΩ in this study) is chosen to balance electrical noise suppression with common mode voltage rejection; the minimum resistance which gave acceptable noise rejection was chosen in this study.

As all temperature measurements were accomplished with thermocouples, it was necessary to establish a datum of known temperature to which the thermocouple readings could be referenced. This was achieved through the use of an integrated resistive temperature detector (RTD) which was present on each of the connector blocks. When activated, the RTD cold junction compensator occupied the first channel of the data acquisition board. The wiring diagrams of the connector blocks used for temperature measurement are shown in Figures 3.6 and 3.7. The first channel of each board (pins 68 and 34) was occupied by cold junction compensation.

An overview of the Labview code execution is given as a flowchart in

Figure 3.8. The measurements based on crankshaft position execute first and are shown within the dashed rectangle. Here the raw voltages from four transducers are measured once per 1° CA over five complete engine cycles (1800° CA). Upon completion, the data from each transducer is averaged over the five engine cycles and predetermined calibration coefficients are applied to the average value to provide meaningful results. This process is then repeated for each of the other transducers, except that the sample rate is now time based. Again, several measurements (typically 100) are obtained from a given transducer, after which the data is averaged and calibration coefficients are applied. Several parameters are then calculated based on the acquired data; namely the H_2 energy fraction (HEF), relative air/fuel ratio (λ) and the EGR mass fraction. Finally, all relevant data is written to a single row in a spreadsheet. Further details regarding experimental procedure and the use of the Labview code are included in Section 3.2.

3.1.8.2 MTS CAS

The MTS CAS was used to obtain cylinder pressure measurements over a consecutive number of engine cycles in real-time. The MTS CAS was connected directly to a personal computer via a PCI-BNC network card, as shown in Figure 3.4. A schematic wiring diagram for the MTS CAS is also included in Figure 3.9. To determine absolute crankshaft position, both the 1 PPR and 3600 PPR signals from the BEI crankshaft encoder were connected to the MTS CAS. A calibration was then required to relate absolute crankshaft position to piston TDC; an overview of this calibration procedure and a representative calibration plot are given in Appendix B.

The cylinder pressure transducer signal was connected to the MTS CAS through an MTS 1104CA charge amplifier. Both the cylinder pressure and crankshaft position were measured for a consecutive number of engine cycles (typically 100). Upon completion of data acquisition, the raw data were post-processed to provide meaningful results. The post-processed data included values of: cylinder pressure, engine speed, crankshaft position, cylinder volume and indicated mean effective pressure (IMEP). The mean, standard deviation, maximum and minimum values of cylinder pressure, IMEP and engine speed were also calculated, thus allowing for a quantification of combustion stability. The raw data were retained for further analysis.

3.2 Test Procedure

It was necessary to follow a regimented procedure when performing engine experiments to ensure the consistency and accuracy of the collected data. The test procedure is described here in two parts, including both the startup and experimental procedures.

3.2.1 Startup Procedure

At the start of each day, the barometric pressure was measured with a mercury barometer and used to update both the Labview and MTS CAS programs. Several measurements depended on atmospheric pressure: the absolute intake and exhaust pressures; the gas properties within the exhaust sample line; and the datum from which the piezoelectric cylinder pressure transducer readings were based. The humidity of the air within the engine lab was also measured and recorded at the beginning of each day using a wet sling psychrometer. This value was updated in the Labview program because humidity affects several calculated properties of the intake mixture.

The bottled supply gases for each of the emissions analyzers were then opened and the analyzers were allowed to warm up for a minimum of one hour before they were used for either calibration or experimentation. It should be noted that a minimum of 30 minutes of warm-up was required for the FID analyzer before flame ignition was typically successful. Following ignition, the FID analyzer was allowed to warm-up for one additional hour. All remaining instrumentation was also warmed up for a minimum of one hour.

After all instrumentation had warmed up, the CFR engine was motored with the eddy current dynamometer. The appropriate valves were then opened on the natural gas fuel supply system, the natural gas fuel injector pulse width was set to an approximate value and the spark timing was adjusted to get the CFR engine to run. Once running, the eddy current dynamometer was set to absorb the power of the CFR engine and the engine speed was set to the desired value. The fuel injector pulse width was adjusted until a stoichiometric air/fuel ratio was indicated and the engine was allowed to warm-up until both the coolant and oil temperatures had reached steady state (typically two hours).

While the engine was warming up, daily instrument preparation and calibration was performed. The emissions analyzers were each calibrated using

bottled gases and a multi-gas calibrator. The strain gauge bridge present in the dynamometer load cell was also balanced using the load cell conditioner. The zero and span on each of the intake and exhaust pressure transducers were set at the beginning of each week, although it was eventually noted that this was not required as the values remained relatively constant. A detailed description of the calibration procedures and representative calibration plots for the above instrumentation are included in Appendix B.

3.2.2 Experimental Procedure

Once all instrumentation had been calibrated and both the engine oil and coolant temperatures had reached steady state, it was possible to begin the experiments.

After selecting HEF and EGR mass fractions to test, the amount of EGR was first set to an approximate value by adjusting the large gate valve (3.1-22). The pulse width of both the natural gas and H_2 fuel injectors were then changed until the approximate HEF was obtained, while also paying attention to maintaining a stoichiometric air/fuel ratio. To obtain the desired final values of both HEF and EGR mass fraction was to perform a somewhat tedious iterative process, with the amount of EGR affecting the amount of gaseous fuel injected and vice versa. Upon achieving the desired HEF and EGR fractions, the engine was allowed to run for a minimum of five minutes. Once stable engine operation had been confirmed, an initial spark timing sweep was performed to bracket an approximate value of maximum brake torque (MBT) spark timing. The spark timing was then adjusted, in intervals of 2° CA, over this region and the value of MBT spark timing was determined. All experiments took place at MBT spark timing for a particular HEF and EGR mass fraction.

Data acquisition was then accomplished in three steps. As the intake plenum mixture was already being sampled by the gas analyzers (to set EGR mass fraction), the Labview code discussed in Section 3.1.8.1 and shown in Figure 3.8 was executed for 100 iterations. This data was stored as an "upstream" Labview data file for a given HEF and EGR mass fraction. The emissions sampling system was then switched to draw a gas sample from the exhaust system. After allowing the gas analyzers one minute to stabilize, the Labview code was executed for another 100 iterations, with the resulting data being stored as a "downstream" Labview data file.

Once the upstream and downstream data had been obtained using the

Labview data acquisition system, the MTS CAS was used to acquire cylinder pressure data, at 0.1° CA intervals, for 100 consecutive engine cycles. This data was immediately post-processed to give values of cylinder pressure, engine speed, crankshaft position, cylinder volume and IMEP.

The above outlined three-step data acquisition procedure was then followed for all desired HEF and EGR mass fraction combinations.

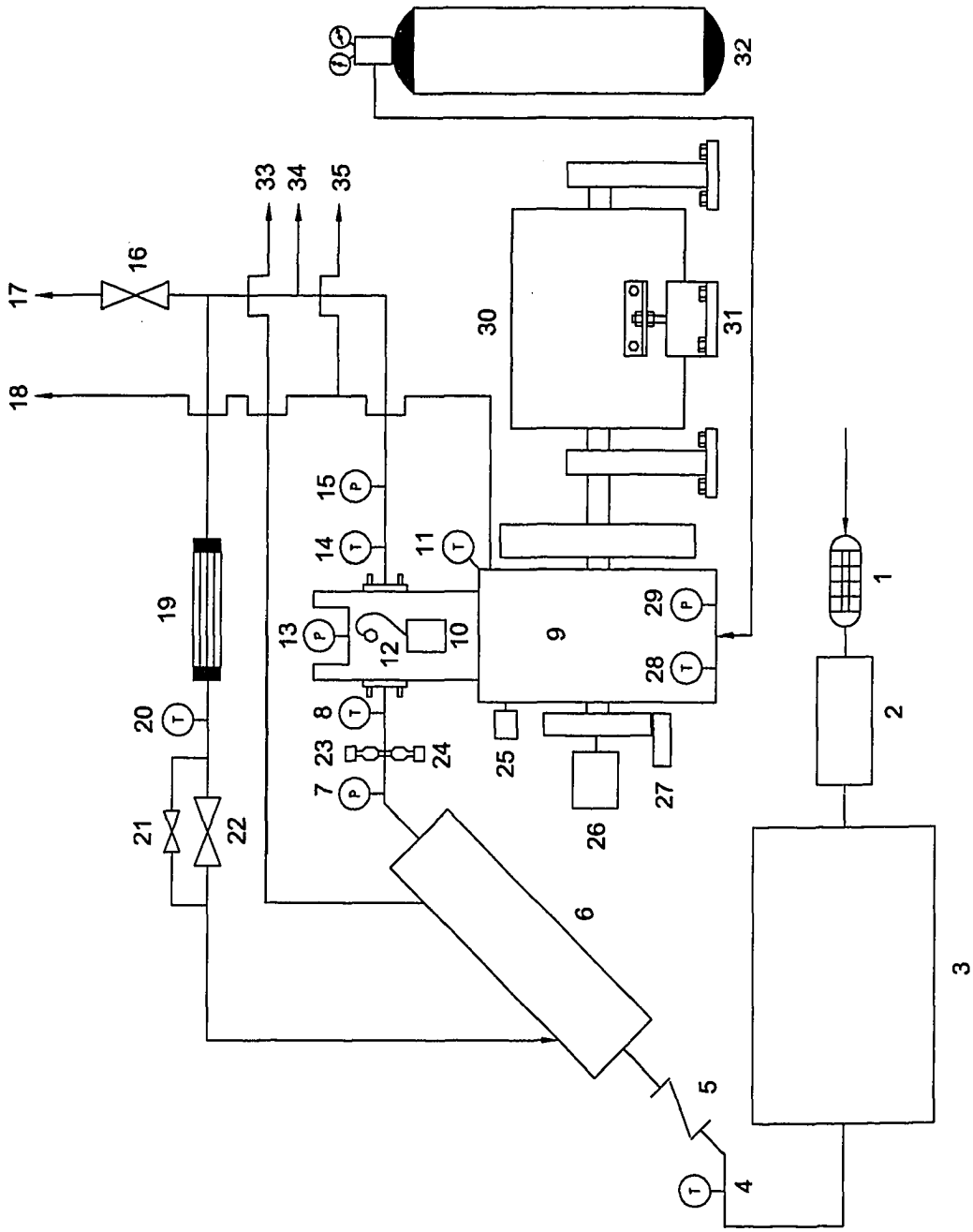

Figure 3.1: Schematic of CFR engine and associated instrumentation. All labels are defined in Table 3.2.

Table 3.2: CFR Schematic Label Descriptions

Label	Description[1]
1	Intake air filter
2	Intake air mass flow meter
3	Intake pulsation barrel
4	Intake air thermocouple
5	Intake throttle valve
6	Intake plenum
7	Intake pressure transducer
8	Intake mixture thermocouple
9	CFR engine
10	Ignition coil
11	Coolant thermocouple
12	Spark plug
13	Cylinder pressure transducer
14	Exhaust thermocouple
15	Exhaust pressure transducer
16	Exhaust back pressure gate valve
17	Exhaust to building exhaust
18	Crank case ventilation to building exhaust
19	EGR cooler
20	Cooled EGR thermocouple
21	Small (6 mm) gate valve for fine EGR control
22	Large (25 mm) gate valve for coarse EGR control
23	H_2 fuel injection
24	Natural gas fuel injection
25	Camshaft hall effect sensor
26	Crankshaft rotary encoder
27	Variable reluctance crankshaft sensor
28	Oil sump thermocouple
29	Oil pressure gauge
30	Eddy current dynamometer
31	Dynamometer force transducer
32	N_2 for crankcase purging during H_2 operation
33	Intake plenum mixture to emissions measurement system
34	Exhaust to emissions measurement system
35	Crankcase vapour to emissions measurement system

[1] Detailed descriptions and serial numbers of equipment are given in Appendix A

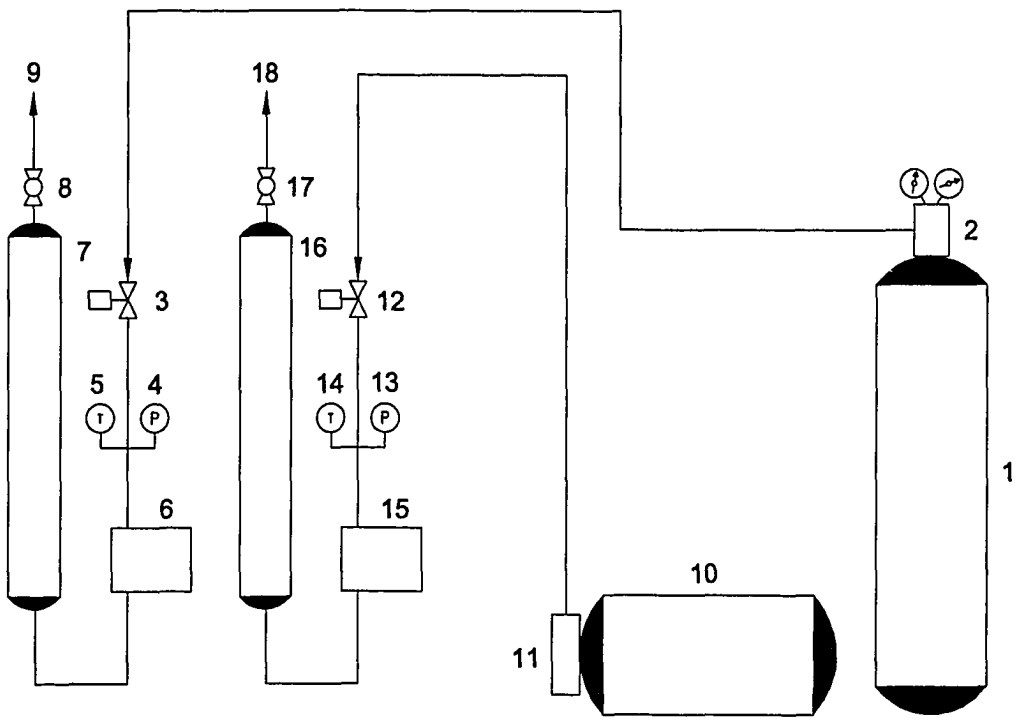

Figure 3.2: Schematic of CFR engine gaseous fuelling system. All labels are defined in Table 3.3.

Table 3.3: Fuelling System Schematic Label Descriptions

Label	Description[1]
1	H_2 fuel cylinder
2	Two-stage H_2 pressure regulator
3	H_2 solenoid shut-off valve
4	H_2 pressure gauge
5	H_2 thermocouple
6	H_2 thermal mass flow meter
7	H_2 plenum
8	H_2 ball shut-off valve
9	H_2 to CFR engine (3.1-23)
10	Natural gas fuel tank
11	Electronic two-stage natural gas pressure regulator
12	Natural gas solenoid shut-off valve
13	Natural gas pressure gauge
14	Natural gas thermocouple
15	Natural gas thermal mass flow meter
16	Natural gas plenum
17	Natural gas ball shut-off valve
18	Natural gas to CFR engine (3.1-24)

[1] Detailed descriptions and serial numbers of equipment are given in Appendix A

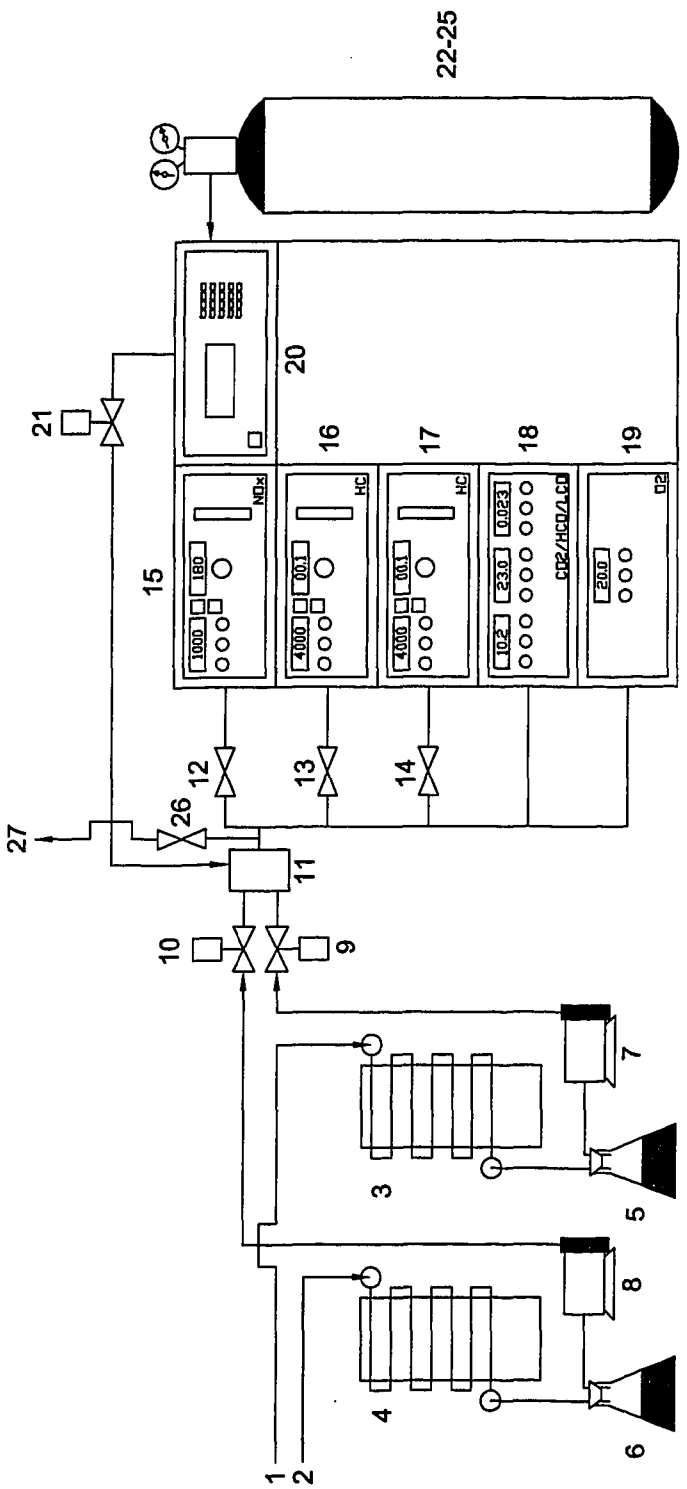

Figure 3.3: Schematic of emissions measurement system. All labels are defined in Table 3.4.

Table 3.4: Emissions Measurement System Schematic Label Descriptions

Label	Description[1]
1	Exhaust emissions from CFR engine (label 34 in Figure 3.1)
2	Intake plenum sample from CFR engine (label 33 in Figure 3.1)
3	Exhaust water knockout
4	Intake water knockout
5	Exhaust water storage beaker
6	Intake water storage beaker
7	Exhaust sample vacuum pump
8	Intake sample vacuum pump
9	Exhaust solenoid valve
10	Intake solenoid valve
11	Distribution block
12	CLD[2] flow adjustment needle valve
13	FID[3] flow adjustment needle valve
14	HFID[4] flow adjustment needle valve
15	CLD analyzer
16	FID analyzer
17	HFID analyzer
18	Non-dispersive infrared analyzer
19	Paramagnetic analyzer
20	Multi-gas calibrator
21	Multi-gas calibrator solenoid valve
22	Paramagnetic calibration gas (79.05% N_2, 20.95% O_2)[5]
23	CLD calibration gas (4021 ppm NO, balance N_2)
24	FID, HFID and low range infrared calibration gas (4.97% CO_2, 4000 ppm CO, 5030 ppm CH_4, balance N_2)
25	High range infrared calibration gas (20.2% CO_2, 2.45% CO, balance N_2)
26	Bypass control valve
27	Bypass to building exhaust

[1] Detailed descriptions and serial numbers of equipment are given in Appendix A

[2] Chemiluminescent detector

[3] Flame ionization detector

[4] Heated flame ionization detector

[5] All gas compositions are given as volume fractions

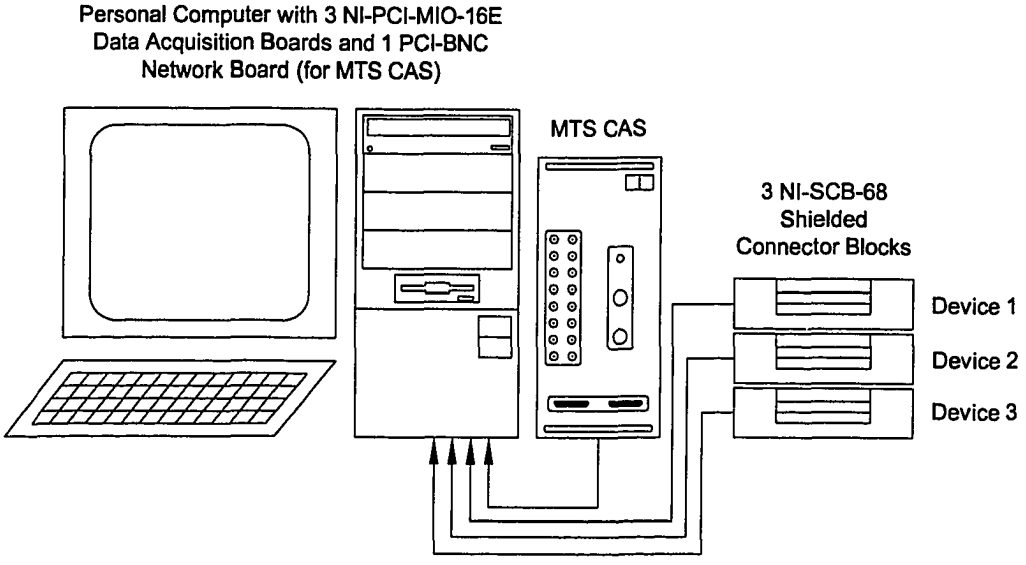

Figure 3.4: Schematic of data acquisition system

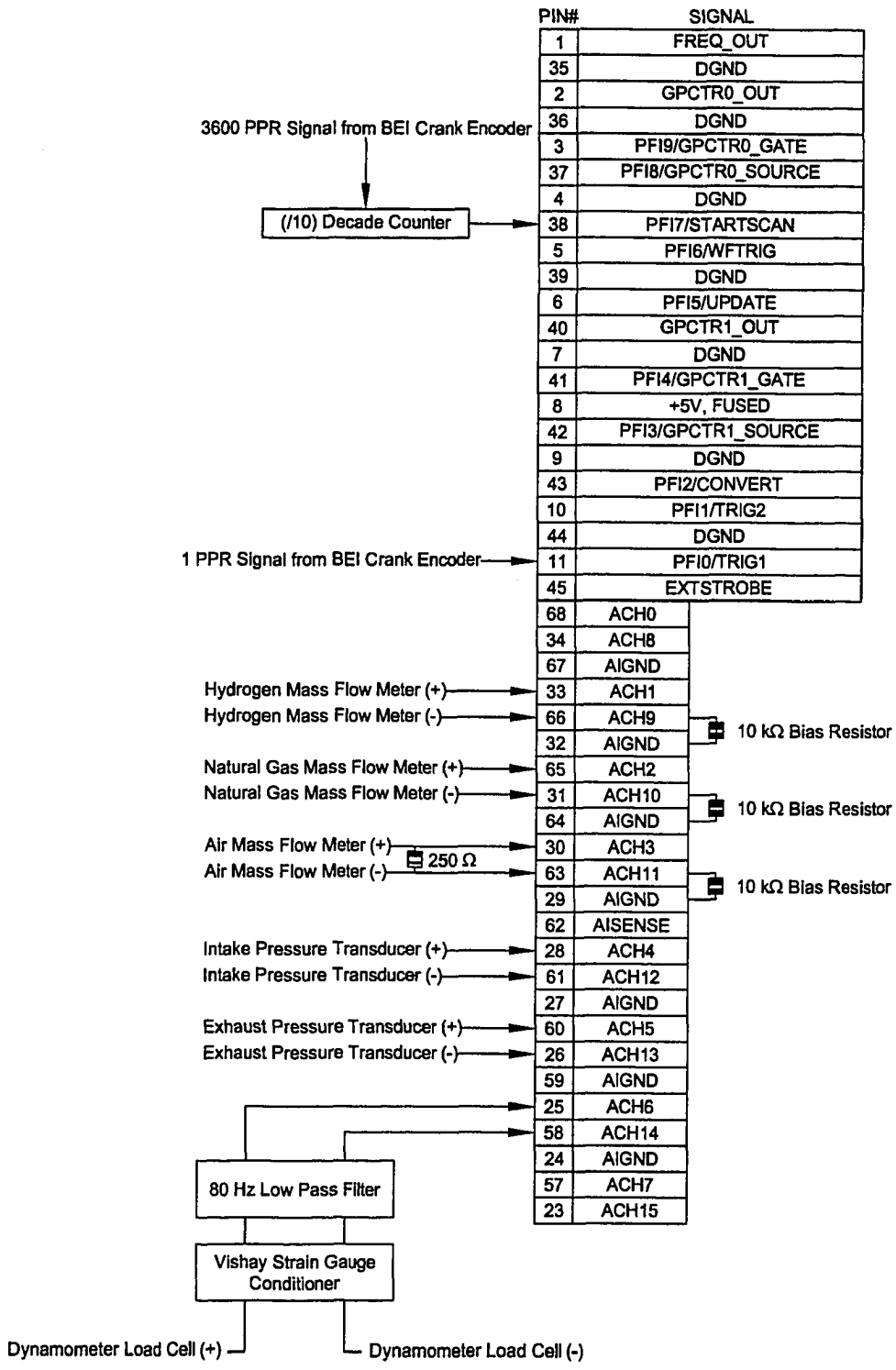

Figure 3.5: Wiring diagram for NI-SCB-68 (Device 1)

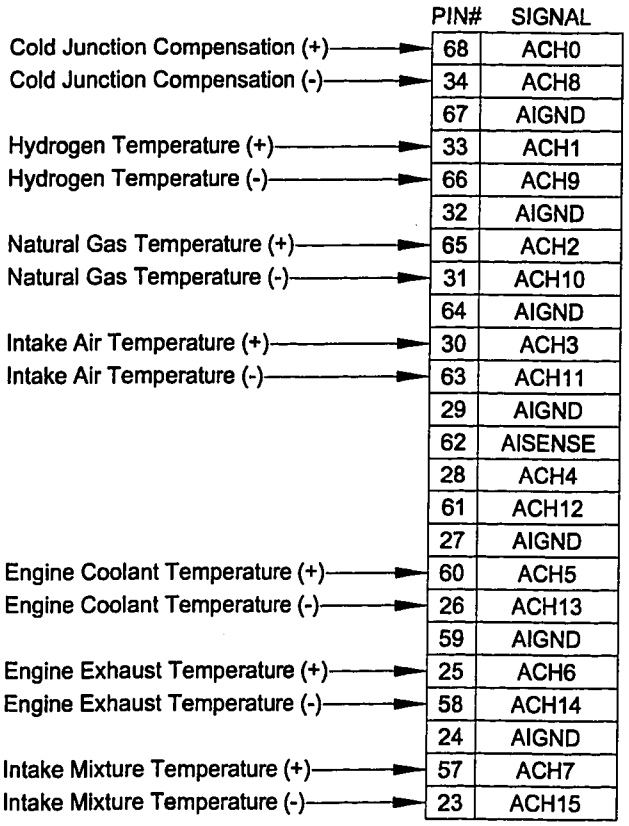

Figure 3.6: Wiring diagram for NI-SCB-68 (Device 2)

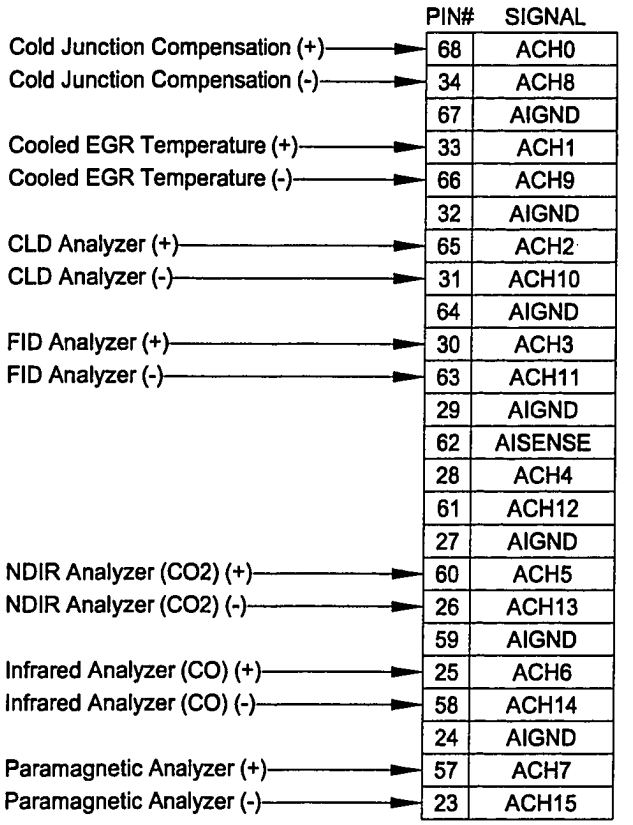

Figure 3.7: Wiring diagram for NI-SCB-68 (Device 3)

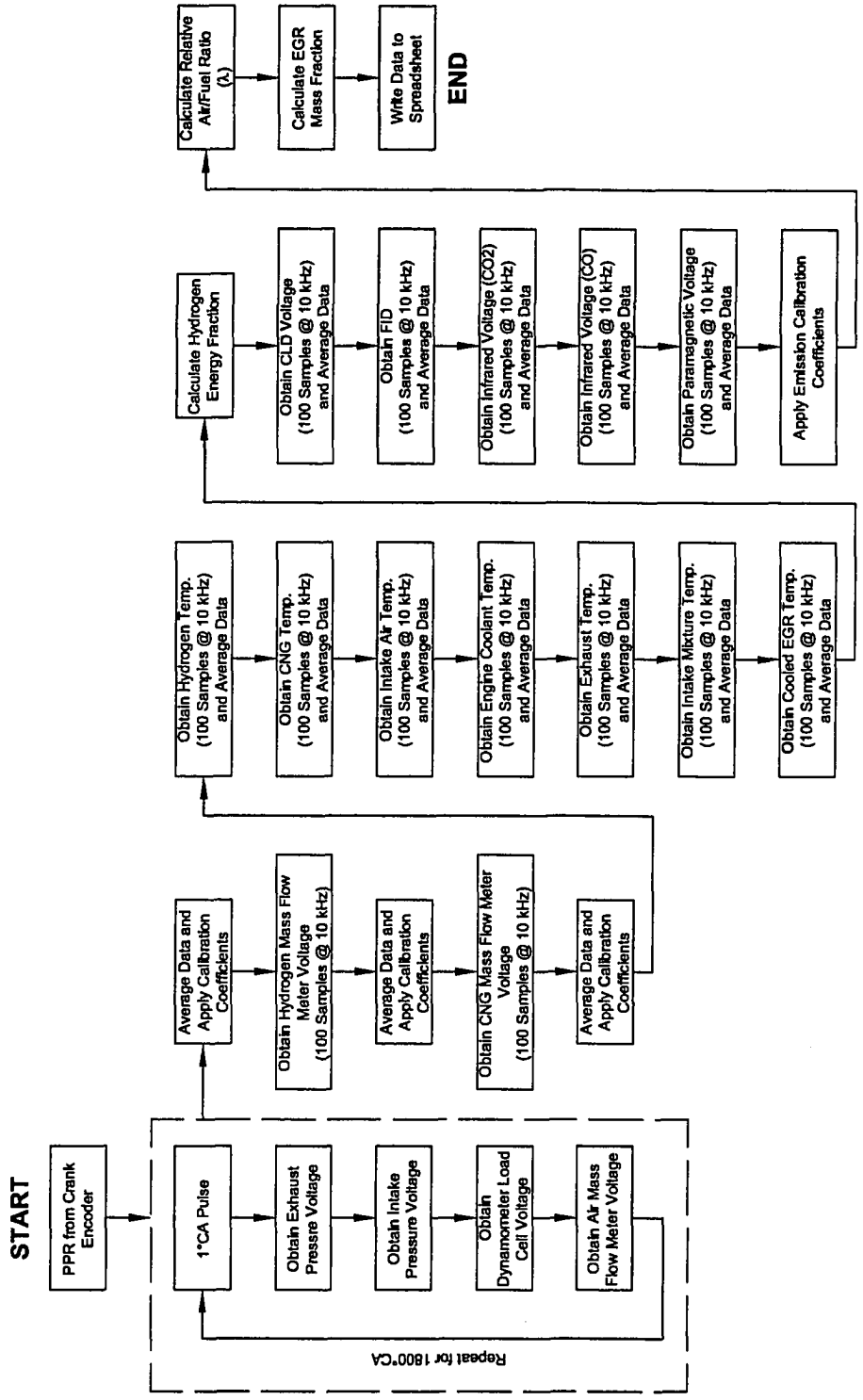

Figure 3.8: Labview execution flowchart

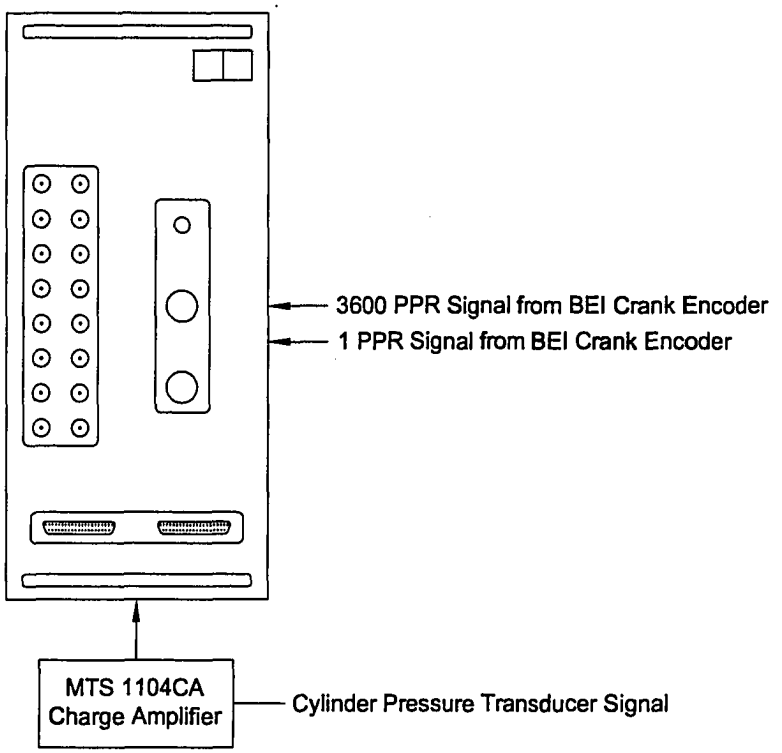

Figure 3.9: Wiring diagram for MTS CAS

Chapter 4

Results and Discussion

To determine the effect of H_2 addition on the exhaust gas dilution limit of a spark ignition (SI) engine, a series of experiments was performed on a single-cylinder cooperative fuel research (CFR) engine.

Prior to dilution limit testing, initial experiments were run to measure the uncertainty in the measured values of engine performance and the uncertainty in setting the maximum brake torque (MBT) spark timing. Two sets of experiments were completed to form 95% confidence intervals for the mean values of each measured engine performance value, as well as for MBT spark timing.

With the confidence intervals established, an initial set of experiments was performed to determine the effect of spark timing on the performance of the engine for an undiluted base condition. Performance was quantified using four measures: output torque, combustion stability, fuel conversion efficiency (η_{fc}) and pollutant emissions. These four performance metrics were the basis for all subsequent experiments. The previously measured uncertainty in spark timing was then translated to an uncertainty in each measured variable. The fraction of the total system uncertainty (as determined by the initial repeatability trials) owing to spark timing was then calculated.

With the relative effect of spark timing on the total system uncertainty established, the first set of experiments was performed to determine the effect of exhaust gas recirculation (EGR) dilution on the performance of the CFR engine with natural gas fuelling.

Finally, a set of experiments was performed to determine the effect of H_2 addition on exhaust diluted engine performance. The amount of H_2 required to return the combustion stability to an original, undiluted value at varying exhaust dilution fractions was also determined.

4.1 Data Post-Processing

4.1.1 Exhaust Emissions

Upon completion of all experiments, it was necessary to post-process the measured exhaust emissions data. As a portion of the water in the exhaust emissions was removed prior to analysis, it was necessary to convert the measured "dry" (some water still exists in the sample line) molar fractions to a wet specific mass emission rate. Specific emissions with units of [g/kW h] are typically used to allow a fair comparison of emission results from different types and sizes of engines, as well as engines operating at different conditions.

It is first necessary to calculate the dry molar fractions of each exhaust component from the measured emissions data. This is straightforward for NO, total hydrocarbon (THC), CO_2, CO and O_2 emissions as they are all measured directly. The mole fraction of water present in the sample line downstream of the water knockout can be calculated as:

$$y_{H_2O,dry} = \frac{P_{sat@T_{line}}}{P_{line}} \tag{4.1}$$

where $P_{sat@T_{line}}$ is the saturated vapour pressure at the measured sample line temperature and P_{line} is the measured sample line pressure. The dry mole fraction of N_2 can then be determined by subtracting all other measured[1] and calculated product mole fractions from unity, as:

$$y_{N_2,dry} = 1 - y_{NO,dry} - y_{THC,dry} - y_{CO_2,dry} - y_{CO,dry} - y_{H_2O,dry} \tag{4.2}$$

To calculate the amount of water that was originally present in the exhaust stream, it is necessary to work back from the combustion equation using the dry molar fractions. The combustion equation including the natural gas composition given in Table C.1, H_2 and all measured and calculated products, is given as:

[1]The mole fraction of H_2 was not measured in this study as it is expected to be low during stable combustion, due mainly to its inherent reactivity.

$$a\,H_2+$$
$$b\,(0.007778\,CO_2 + 0.01934\,N_2 + 0.9539\,CH_4 + 0.01901\,C_2H_6)+$$
$$d\,(O_2 + 3.773\,N_2 + e\,H_2O) \rightarrow$$
$$f\,H_2O + g\,CO_2 + h\,O_2 + i\,CO + j\,NO + k\,CH_4 + m\,N_2 \quad (4.3)$$

The number of moles of water present in the intake air can be calculated as:

$$e = n_{H_2O} = \frac{4.773\,P_{vap}}{P_{atm} - P_{vap}} \quad (4.4)$$

where P_{vap} is the vapour pressure of the intake air and P_{atm} is the measured atmospheric pressure. Using the measured and calculated product dry mole fractions and the number of moles of water present in the intake air, it is now possible to balance each element in Equation 4.3, allowing for the determination of the unknown reactant coefficients and the amount of water originally present in the exhaust. The elemental balances are given as:

$$\text{C:} \quad b = \frac{y_{CO_2,dry} + y_{CO,dry} + y_{THC,dry}}{0.9997} \quad (4.5)$$

$$\text{N:} \quad d = \frac{y_{NO,dry} + 2\,y_{N_2,dry} - 0.03868\,b}{7.546} \quad (4.6)$$

$$\text{O:} \quad f = 0.01556\,b + d\,(2+e) - 2\,y_{CO_2,dry} - 2\,y_{O_2,dry} - y_{CO,dry} - y_{NO,dry} \quad (4.7)$$

$$\text{H:} \quad a = f + 2\,y_{THC,dry} - 1.965\,b - e\,d \quad (4.8)$$

A correction factor for the actual amount of water in the exhaust stream can now be calculated as:

$$y_{wet,corr} = 1 + (f - y_{H_2O,dry}) \quad (4.9)$$

The wet mole fractions of each exhaust component are now determined as:

$$y_{wet} = \frac{y_{dry}}{y_{wet,corr}} \quad (4.10)$$

To calculate the wet indicated specific mass emissions, it is first required to convert the wet mole fraction emissions to wet mass fractions. The molar mass of the exhaust is calculated as:

$$M_{exh} = \frac{\sum_{i=1}^{n} M_i \, y_{i,wet}}{\sum_{i=1}^{n} y_{i,wet}} \tag{4.11}$$

where $y_{i,wet}$ and M_i are the wet mole fraction and molar mass of individual exhaust components, respectively. To satisfy conservation of mass, the mass flow rate of exhaust can be calculated as:

$$\dot{m}_{exh} = \dot{m}_{air} + \dot{m}_{H_2} + \dot{m}_{CNG} \tag{4.12}$$

where $\dot{m}_{air}$, $\dot{m}_{H_2}$ and $\dot{m}_{CNG}$ are the mass flow rates of the intake air, H_2 fuel and natural gas fuel, respectively.

The mole rate of exhaust is then:

$$\dot{n}_{exh} = \frac{\dot{m}_{exh}}{M_{exh}} \tag{4.13}$$

Finally the mass flow rate of each exhaust component is calculated as:

$$\dot{m}_i = y_{i,wet} \, \dot{n}_{exh} \, M_i \tag{4.14}$$

The indicated specific mass emissions of individual exhaust components can now be determined as:

$$IS_i = \frac{3600 \, \dot{m}_i}{P_{ind}} \tag{4.15}$$

where P_{ind} is the indicated output power of the engine in [kW], as calculated from the cylinder pressure data, and $\dot{m}_i$ is the wet mass emission rate of an individual exhaust component in [g/s]. The resulting indicated emissions are then in [g/kW h].

4.1.2 Chauvenet's Criterion

The final step in post-processing the data involved the elimination of suspect data that occurred due to random errors. Occasionally there would be points

of data which were obviously incorrect by several orders of magnitude, likely as a result of an isolated and unknown problem with the data acquisition system. To easily and consistently remove these from the raw data sets, Chauvenet's Criterion was used (Taylor, 1997, pp. 166-169).

If it is assumed that the measured data follow a Gaussian distribution, the probability of a single datum occurring at a certain distance from the mean value of the data set can be calculated. If the probability of this datum occurring over a given number of measurements is low, then the datum is rejected.

For a Gaussian distribution, the number of standard deviations between the mean value of the data set and the datum being investigated, can be determined as:

$$d = \frac{x - \bar{x}}{\sigma_x} \tag{4.16}$$

where: x = datum
$\bar{x}$ = mean value of data
σ_x = sample standard deviation of data

The probability that a single measured value lay within $\bar{x} \pm d\sigma$ is calculated as the area under the normal distribution centered upon $\bar{x}$, between $-d\sigma$ and $+d\sigma$, or:

$$P_{in} = \frac{1}{\sqrt{2\pi}} \int_{-d}^{d} e^{\frac{-z^2}{2}} dz \tag{4.17}$$

So it follows that the probability of the single measured value laying outside $\bar{x} \pm d\sigma$ is:

$$P_{out} = 1 - P_{in} \tag{4.18}$$

Chauvenet's Criterion states that a single datum may not deviate any more than that which causes the number of expected occurrences in N measurements to be more than 0.5. That is:

$$N \cdot P_{out} \leq 0.5 \tag{4.19}$$

where N is the number of measurements in the data set. In this case, 100 measurements were taken at each test point, resulting in the requirement that

Table 4.1: Statistical Effects of Applying Chauvenet's Criterion

Average percentage change in mean value	0.55
Maximum percentage change in mean value	110
Average percentage change in SSD	3.6
Maximum percentage change in SSD	100
Average number of rejected points (per 100)	0.36
Maximum number of rejected points (per 100)	4.0

$P_{out} \leq 0.005$, or that any single datum cannot lie beyond 2.81 σ from $\bar{x}$. As all testing was performed at steady-state conditions and 100 samples were taken at each test point, Chauvenet's Criterion only rejects acute outliers. However, any researcher should be wary of rejecting individual data points without a specific reason and so a comparison was made between data sets before and after the use of Chauvenet's Criterion. Table 4.1 shows the statistical results of the application of Chauvenet's Criterion on all data sets.

As expected, the application of Chauvenet's Criterion to steady state test conditions and 100 sample data sets resulted in an average change in mean and sample standard deviation (SSD) values of only 0.55 and 3.6% respectively. The maximum change in mean and SSD values of 110% and 100% were due to single faulty thermocouple readings on the order of $1x10^4$ °C within a data set. The isolation of these occurrences is also reflected in the average and maximum number of rejected readings per 100 measurements, 0.36 and 4.0 respectively.

4.2 The Effect of Spark Timing on Engine Performance

To understand the effect of spark timing on engine performance, and to determine how much of the total uncertainty in each measurement had been translated through a variance in spark timing, a series of engine experiments was conducted. All engine conditions were kept constant at the values listed in Table 4.2, with the exception of spark timing, which was varied over an interval with MBT timing occurring approximately in the center of the range.

Table 4.2: CFR Engine Operating Conditions

Engine Speed	1200±1 RPM
Compression Ratio	11.5
Fuel	Compressed Natural Gas
Throttle Position	Fully Open
Spark Timing	MBT±2°
Relative Air/Fuel Ratio, λ	1.00±0.02
Atmospheric Pressure	93.50±0.7 kPa
Atmospheric Vapour Pressure	1.50±0.2 kPa
Oil Temperature	70±5°C
Water Temperature	99±1°C

4.2.1 Output Torque

Measurements of engine torque have been normalized for engine displacement and reported as indicated mean effective pressure (IMEP) in this study. Figure 4.1 shows that IMEP reaches a maximum value at MBT spark timing (12° BTDC). As is typical, the difference between adjacent IMEP values near peak output is relatively small, making the determination of MBT timing difficult. The uncertainty in spark timing of ±2° CA has a limited effect on IMEP as shown in the hatched region in Figure 4.1. Here the spark timing uncertainty accounts for only 19% of the total uncertainty in IMEP. It is believed that uncertainty in the air/fuel ratio was responsible for a large part of the remaining error.

The IMEP is directly related to the cylinder pressure history for a given engine cycle. To better understand the relation between IMEP (and all other performance metrics) and spark timing it is prudent to examine how cylinder pressure development varies with spark timing. Figure 4.2 shows the development of cylinder pressure for 100 consecutive engine cycles at three spark timings: retarded (6° BTDC), MBT (12° BTDC) and advanced (18° BTDC).

A retarded spark timing as seen in Figure 4.2(a) results in low peak pressure and sustained pressure during the expansion stroke, thus resulting in reduced IMEP. In contrast, an advanced spark timing as in Figure 4.2(c) results in a rapid pressure rise during the compression stroke and a very

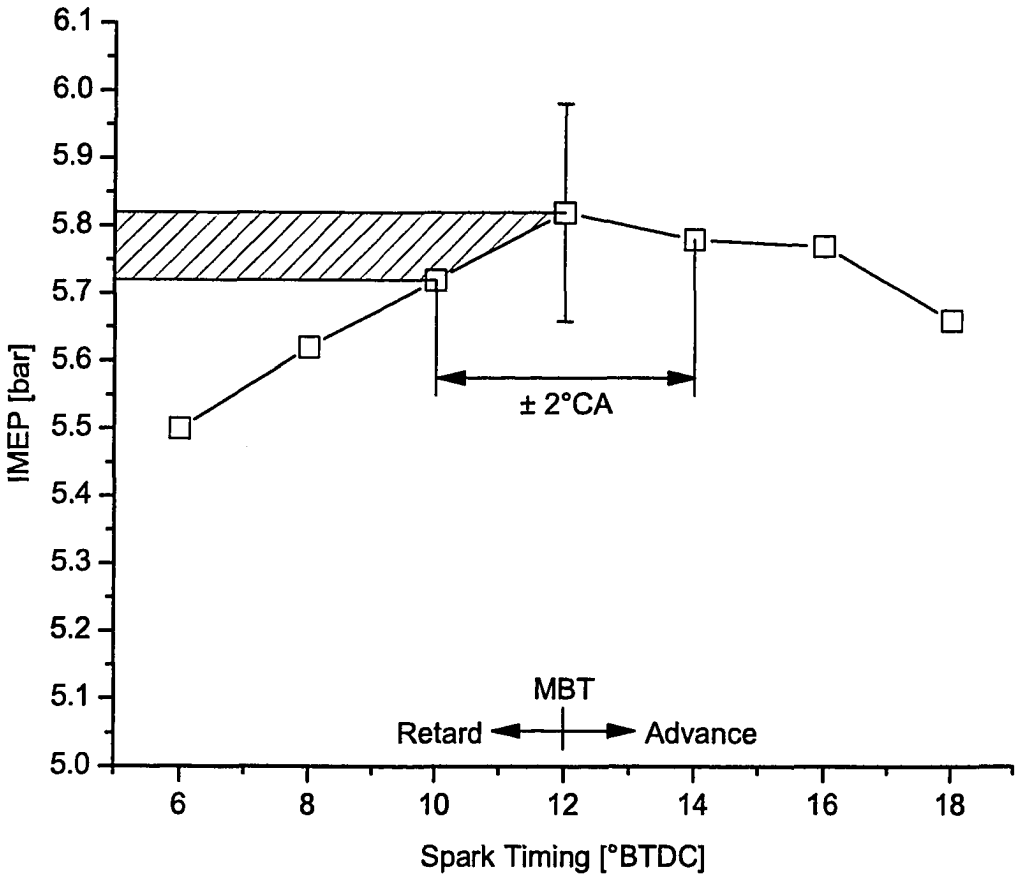

Figure 4.1: The effect of uncertainty in MBT spark timing on IMEP. The hatched region indicates a 95% confidence interval resulting from a ±2° CA variance in determining MBT spark timing. The error bar indicates a 95% confidence interval for the measured value of IMEP based on repeated experiments at MBT spark timing.

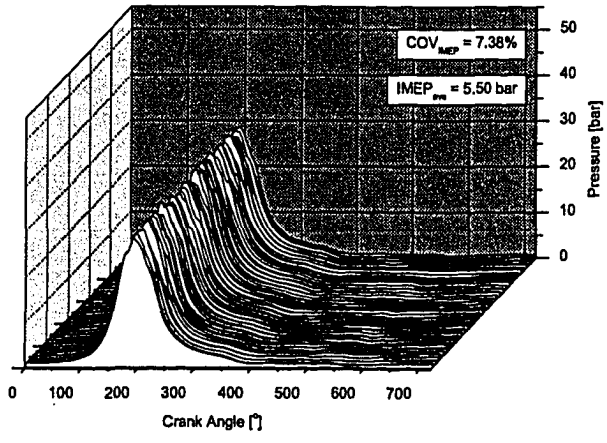

(a) 6° BTDC

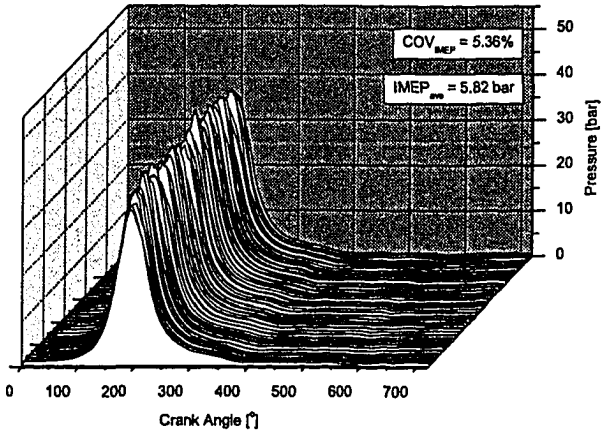

(b) 12° BTDC (MBT)

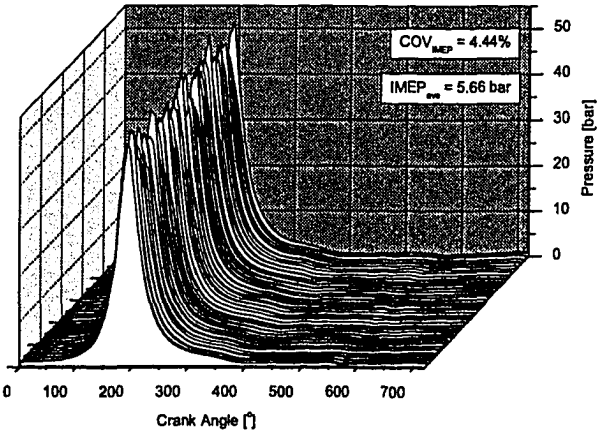

(c) 18° BTDC

Figure 4.2: The effect of spark timing on cylinder pressure history. Data is given for 100 consecutive engine cycles.

high peak pressure. The excessive negative work which occurs during the compression stroke also causes a decreased IMEP. The cylinder pressure data for MBT spark timing is represented in Figure 4.2(b). Here the negative work during the compression stroke is balanced with an optimal amount of combustion occurring during the expansion stroke, thus resulting in a maximum value of IMEP.

4.2.2 Combustion Stability

Combustion stability plays a central theme in this study and it is discussed here as a dependent variable of spark timing. In this study, the measure of combustion stability used is the covariant indicated mean effective pressure (COV IMEP) for a set of 100 consecutive engine cycles. The effect of spark timing on COV IMEP is shown in Figure 4.3. Here it is seen that an advance in spark timing generally decreases COV IMEP. However, if data had been taken at further advances in spark timing, the COV IMEP would likely have begun to rise. It has been observed that COV IMEP reaches a minimum value at approximately MBT timing, where further advances cause a rise in COV IMEP whose steepness is proportional to the burning rate of the engine (Ozdor et al., 1994).

The fraction of total uncertainty in COV IMEP attributable to uncertainty in spark timing is shown in Figure 4.3 to be 34%. However, the measured value of COV IMEP at 14° BTDC, while within the error limits, is likely high which causes the error attributed to spark timing to be conservative. If this suspect point had followed the observed trend in COV IMEP, a majority of the uncertainty in COV IMEP would be due to spark timing with the remainder likely caused by variance in the air/fuel ratio.

At MBT timing the value of COV IMEP is 5.36 $\pm$ 1.05 bar, as shown in Figure 4.3. This range of combustion stability is considered acceptable for the remainder of experiments. If a change in parameters causes the combustion stability to rise out of this range, it is considered to be unacceptable and is labeled as such with an 'X' symbol.

4.2.3 Fuel Conversion Efficiency

Spark timing has a direct and well known effect on η_{fc}; the results from this study are shown in Figure 4.4. It is shown that the peak η_{fc} coincides with MBT spark timing. If the spark timing is advanced from MBT, the amount

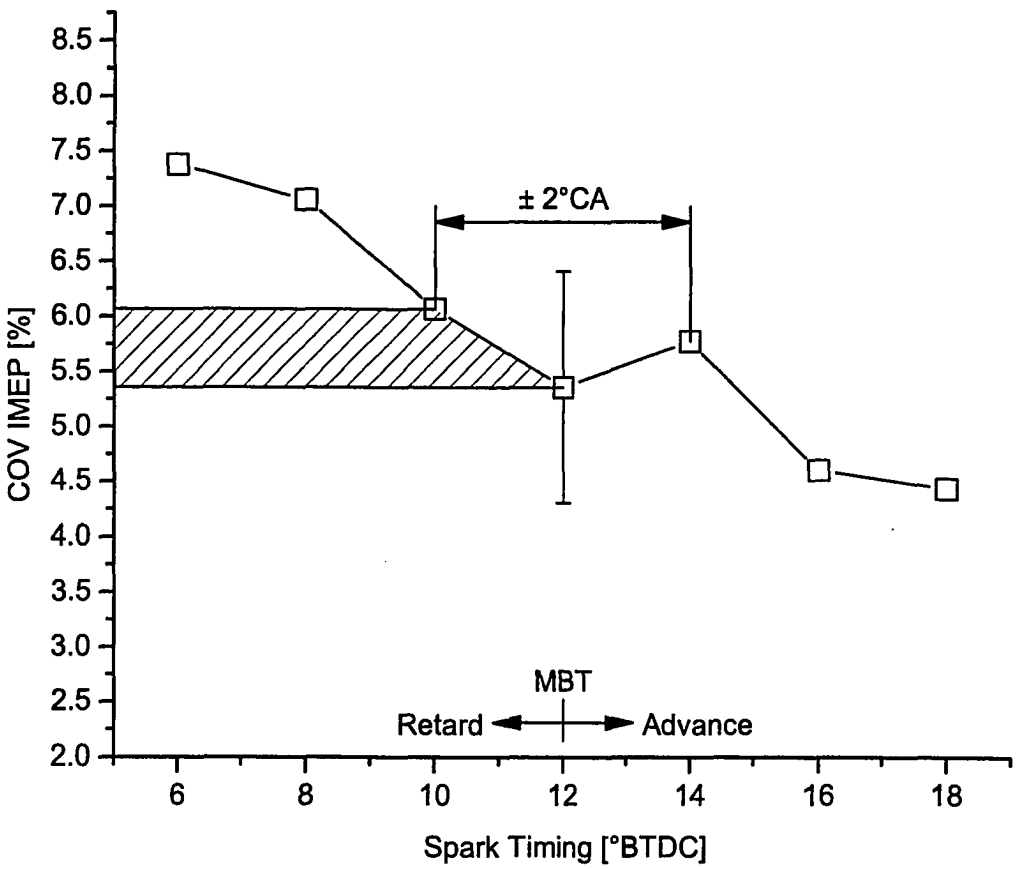

Figure 4.3: The effect of uncertainty in MBT spark timing on COV IMEP. The hatched region indicates a 95% confidence interval resulting from a ±2° CA variance in determining MBT spark timing. The error bar indicates a 95% confidence interval for the measured value of COV IMEP based on repeated experiments at MBT spark timing.

of negative work exerted *against* the piston by the cylinder contents is too large, resulting in a decreased η_{fc}. Whereas, if the spark timing is retarded from MBT, peak cylinder pressures are reduced as a greater portion of the combustion is still occurring during the expansion stroke, again resulting in a reduced η_{fc}. The reduction in η_{fc} associated with a retarded spark timing can also be seen in an increased exhaust temperature, as shown in Figure 4.5. Similar predicted results for η_{fc} and exhaust temperature, as functions of spark timing, have been previously observed (Heywood et al., 1979).

The uncertainty in η_{fc} due to spark timing is shown in Figure 4.4 as 26% of the total uncertainty. The remaining uncertainty can be attributed to variations in air/fuel ratio. However, the uncertainty in exhaust temperature illustrated in Figure 4.5 can be wholly accounted for by the uncertainty in spark timing.

4.2.4 Pollutant Emissions

To determine the effect of spark timing on pollutant emissions, and to determine the emissions implications associated with accurately determining the MBT spark timing, the exhaust stream was analyzed for three pollutants: NO, CO and total hydrocarbons. It was found that the accuracy to which the MBT spark timing was determined had profound implications on the level of NO emissions produced. Spark timing was also shown to have an effect on both CO and THC emissions.

4.2.4.1 Nitric Oxide

It is commonly known that spark timing greatly affects the NO emissions of an SI engine; Figure 4.6 illustrates the results obtained in this study. As the spark timing is advanced from MBT, a greater fraction of fuel combusts before TDC, resulting in higher peak pressures and thus higher peak in-cylinder temperatures. Contrariwise, as the spark timing is retarded, a smaller fraction of fuel burns before TDC, resulting in lower peak pressures and in-cylinder temperatures. This behaviour is seen in the cylinder pressure data presented in Figure 4.2. As it is well established that the kinetics which govern the production of NO have a strong dependence upon temperature (Lavoie et al., 1970), it is expected that as the peak in-cylinder temperature increases, so too does the peak NO concentration. Figure 4.6 shows that an advance in spark timing of 6° from MBT results in an increase in specific NO

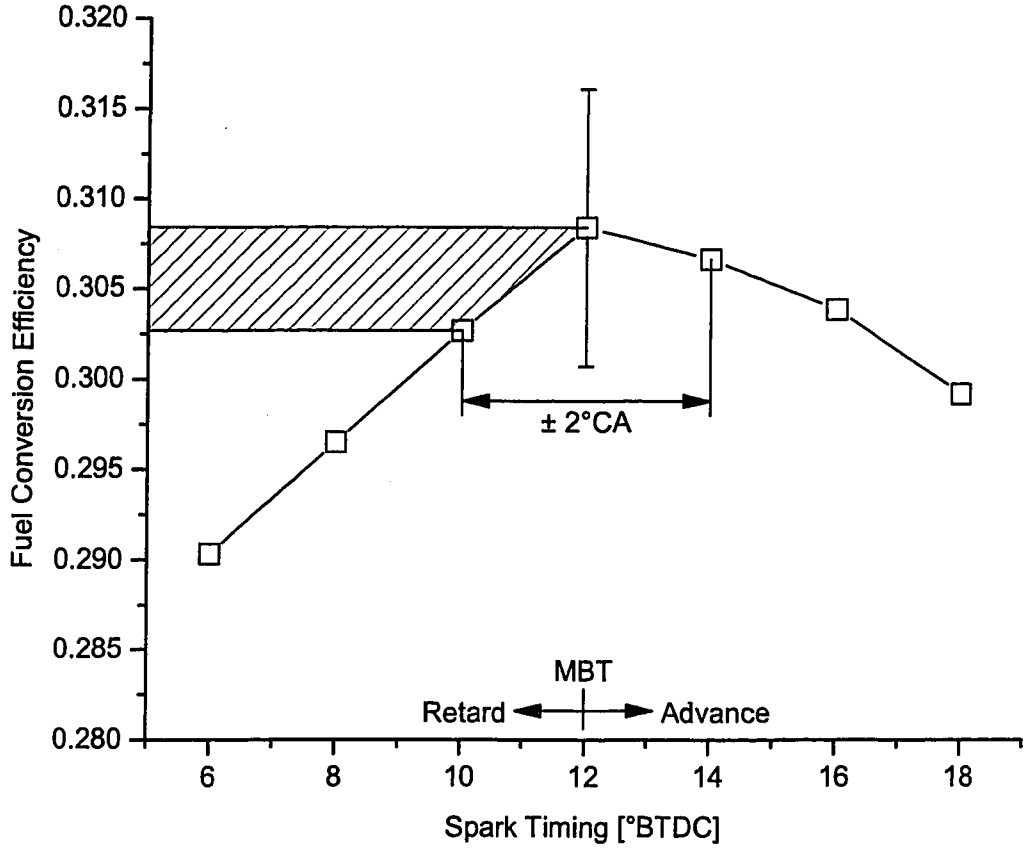

Figure 4.4: The effect of uncertainty in MBT spark timing on fuel conversion efficiency. The hatched region indicates a 95% confidence interval resulting from a ±2° CA variance in determining MBT spark timing. The error bar indicates a 95% confidence interval for the measured value of fuel conversion efficiency based on repeated experiments at MBT spark timing.

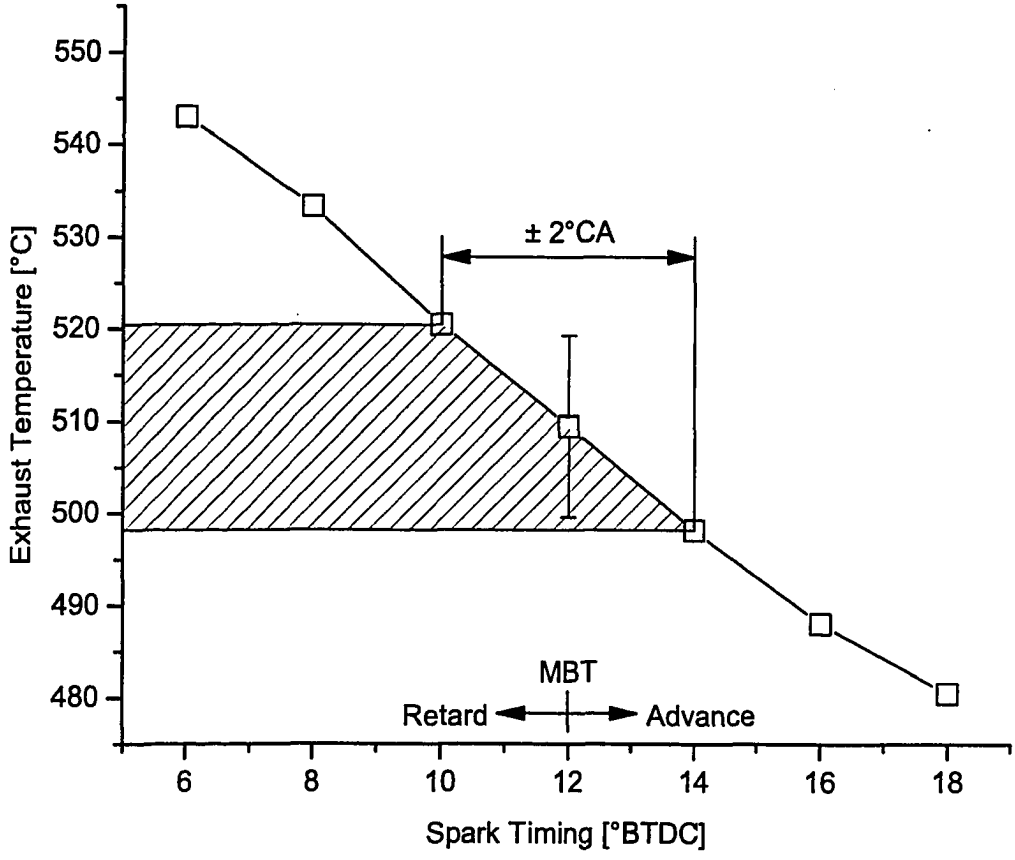

Figure 4.5: The effect of uncertainty in MBT spark timing on exhaust gas temperature. The hatched region indicates a 95% confidence interval resulting from a ±2° CA variance in determining MBT spark timing. The error bar indicates a 95% confidence interval for the measured value of exhaust gas temperature based on repeated experiments at MBT spark timing.

emissions of 55% whereas retarding the spark timing by 6° results in a 43% decrease.

Beyond the relation between spark timing and NO emissions, Figure 4.6 also reveals the effect of an uncertainty in determining MBT spark timing on measured NO emissions. The hatched area in Figure 4.6 represents the change in measured NO emissions resulting from an uncertainty of MBT spark timing of ±2° CA. This uncertainty in MBT spark timing translates to a possible 19% increase or 17% decrease in NO emissions. The measured total uncertainty (based on repeated trials) of NO emissions, as indicated by the error bar in Figure 4.6, is only ±14%.

Clearly the system uncertainty is expected to be at least as high as the contribution from an uncertainty in MBT spark timing. One possible explanation for the disparity is the inherent bias encountered when setting the spark timing in repeated trials of system uncertainty. This would result in a lower total uncertainty in NO emissions, as spark timing is a major contributing factor.

Regardless of the discrepancy in uncertainties, the effect of spark timing on indicated NO emissions has been demonstrated. The total uncertainty in measured NO measurements has been shown to be mostly due to an uncertainty in spark timing, thus underscoring the importance of a proper spark timing strategy.

4.2.4.2 Carbon Monoxide

Spark timing also has an effect, albeit less pronounced, on CO emissions. Typically, CO emissions are a function of the air/fuel ratio, with the effect of spark timing being minor in comparison. In an SI engine, the in-cylinder concentration of CO remains equilibrated for local conditions until the middle stages of the expansion stroke. Through the later stages of the expansion stroke and the exhaust stroke, CO concentrations are kinetically controlled by the oxidation of CO to CO_2 (Heywood, 1988, pp. 592-596). Because the rate of CO oxidation is primarily a function of temperature, spark timing plays a role in determining how much post-combustion oxidation occurs.

The relation between spark timing and CO emissions is illustrated in Figure 4.7. It can be seen that as the spark timing is advanced, CO emissions increase, likely due to the reduced levels of post-combustion oxidation associated with a decreasing exhaust temperature. However, the trend of increasing CO emissions with advanced spark timing is not significantly beyond

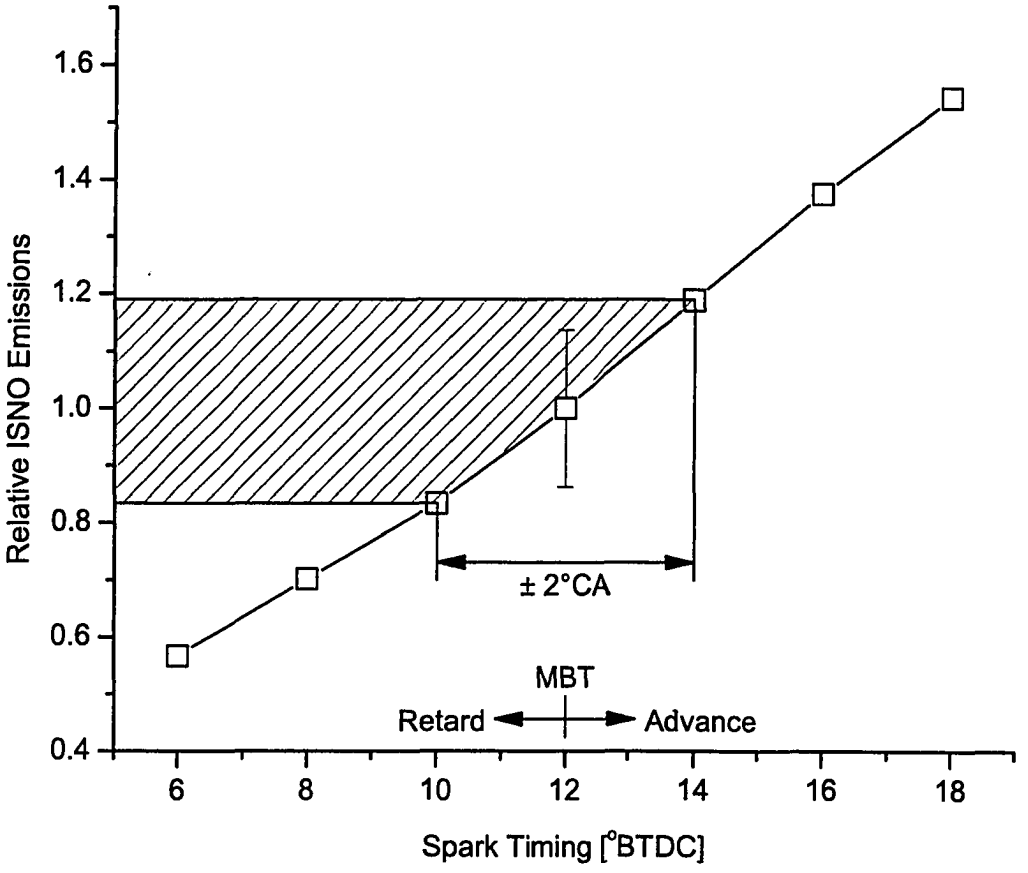

Figure 4.6: The effect of uncertainty in MBT spark timing on relative ISNO emissions. Values are relative to MBT spark timing. The hatched region indicates a 95% confidence interval resulting from a ±2° CA variance in determining MBT spark timing. The error bar indicates a 95% confidence interval for the measured value of relative ISNO emissions based on repeated experiments at MBT spark timing.

the measurement uncertainty, making the distinction of a trend difficult. A previous study has suggested that spark timing plays a negligible role in CO emissions, especially when compared with variations in air/fuel ratio (Hagen and Holiday, 1962). This is reinforced when noting that the uncertainty in spark timing only accounts for a minor fraction of total uncertainty. Figure 4.7 indicates that the uncertainty in spark timing, as indicated by the hatched region, only accounts for 33% the total uncertainty in CO measurements. It is reasonably presumed that a large part of the remaining total uncertainty is due to a variance in the air/fuel ratio.

4.2.4.3 Total Hydrocarbons

The effect of spark timing on THC emissions is shown in Figure 4.8. Similar to the trend of CO emissions, an advanced spark timing results in increased THC emissions. There are several mechanisms responsible for hydrocarbon emissions and spark timing plays a role in several of them.

The first and most important source of hydrocarbon emissions comes from the cylinder crevice volumes where it has been estimated that 38% of THC emissions are produced (Cheng et al., 1993). As the spark timing is advanced, a larger mass of fuel/air mixture is forced into these crevice volumes as a result of higher peak pressures, as is shown in Figure 4.2(a). While an increased cylinder pressure also increases the rate of blow-by, it has been shown that it is not sufficient to compensate for the increased mass of hydrocarbons compressed into the crevice volumes (Daniel, 1970). As the cylinder pressure falls and the hydrocarbons in the crevice volumes are released into the cylinder, they are further oxidized within the cylinder and exhaust system. However, this process of post-combustion oxidation is largely dependent upon the in-cylinder temperature during the expansion stroke and the resulting exhaust temperature, both of which are decreased with an advance in spark timing. The negative effect of an advanced spark timing on hydrocarbon emissions is thus further compounded by temperature effects.

The sensitivity of hydrocarbon emissions to an uncertainty in spark timing is shown as the hatched region in Figure 4.8. It can be seen that 47% of the total uncertainty in relative indicated THC emissions is due to an uncertainty in spark timing. As with CO, the remaining uncertainty is likely due to variations in air/fuel ratio.

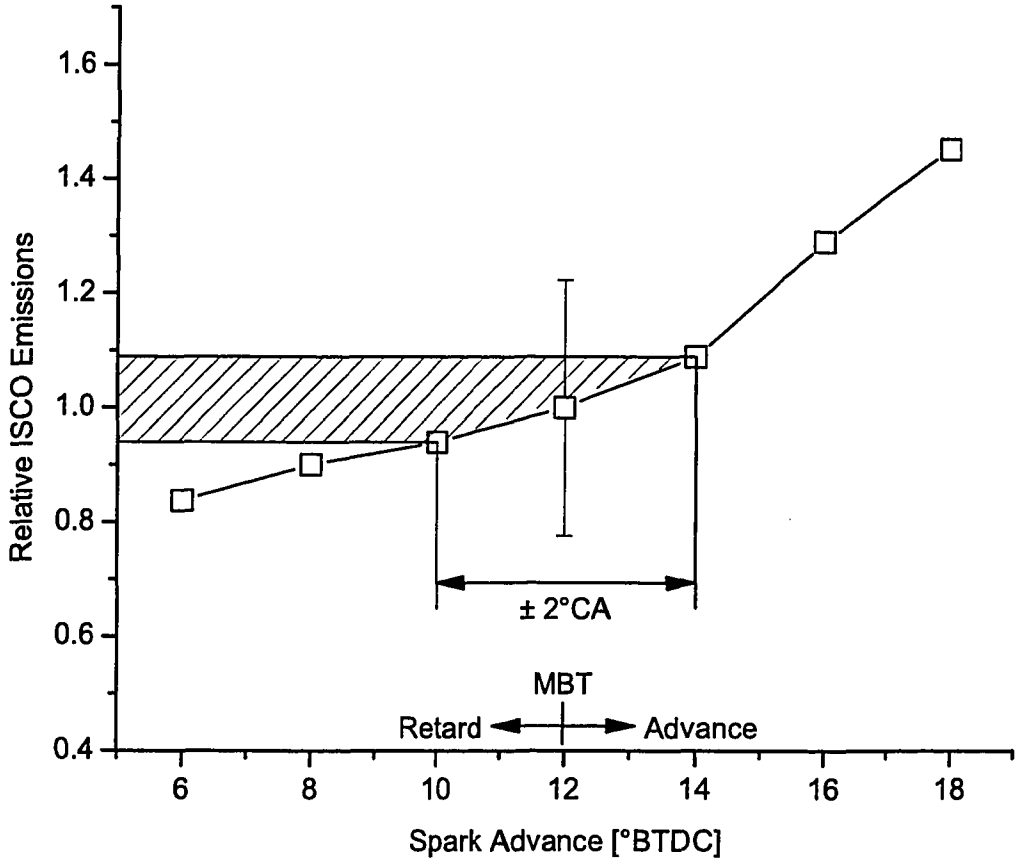

Figure 4.7: The effect of uncertainty in MBT spark timing on relative ISCO emissions. Values are relative to MBT spark timing. The hatched region indicates a 95% confidence interval resulting from a ±2° CA variance in determining MBT spark timing. The error bar indicates a 95% confidence interval for the measured value of relative ISCO emissions based on repeated experiments at MBT spark timing.

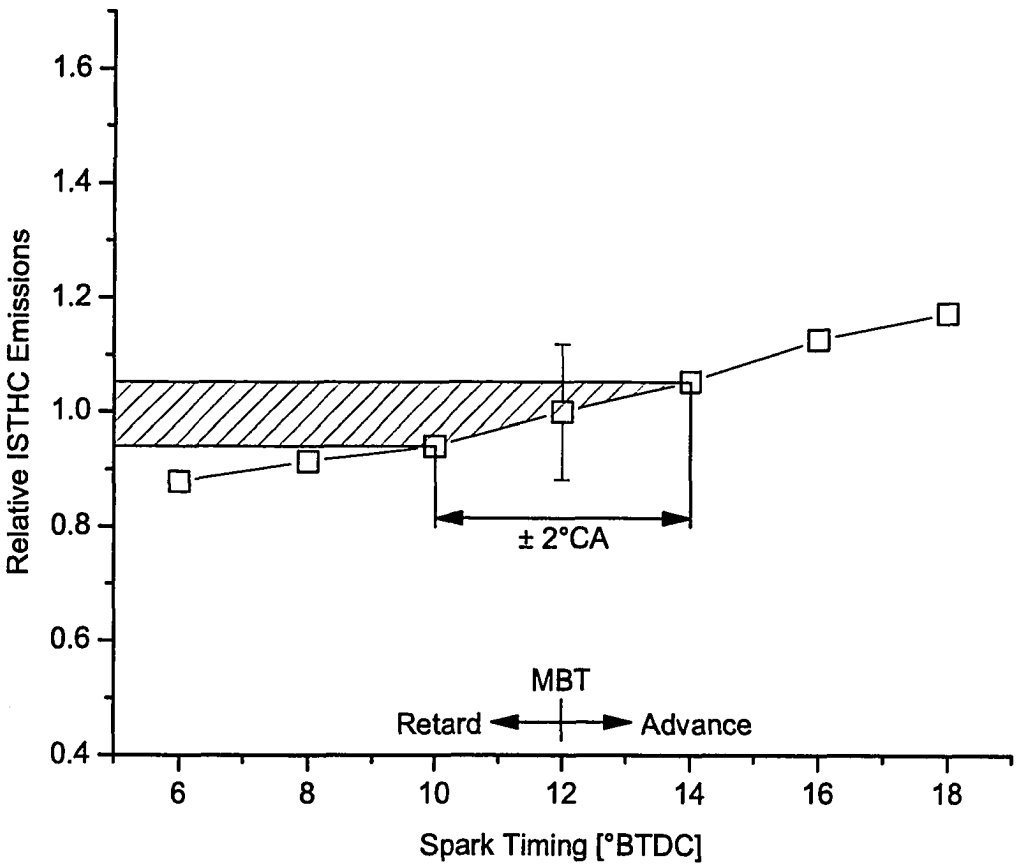

Figure 4.8: The effect of uncertainty in MBT spark timing on relative ISTHC emissions. Values are relative to MBT spark timing. The hatched region indicates a 95% confidence interval resulting from a ±2° CA variance in determining MBT spark timing. The error bar indicates a 95% confidence interval for the measured value of relative ISTHC emissions based on repeated experiments at MBT spark timing.

4.3 The Effect of EGR on Engine Performance

In this study, 'EGR' refers to external EGR where the products of combustion are returned to the intake of the engine via an external pathway. In reality, the total amount of exhaust gas dilution which occurs is the sum of any external EGR and the residual gas (prompt EGR) which is retained between engine cycles. Thus, any EGR mass fraction reported in this study is lower than the total amount of in-cylinder diluent content. However, the primary factors which affect the residual gas fraction (Fox et al., 1993) have remained constant between experiments, thus qualifying external EGR as a suitable measure of overall exhaust dilution in this study.

The use of EGR in SI engines has been studied and employed extensively as a means of controlling NO emissions in production automotive SI engines (Jääskeläinen and Wallace, 1994). Given its popularity and widespread use, it is prudent to investigate other performance implications of EGR use. However, this prudence has been shown previously and the effect of EGR on almost every metric of engine performance has been investigated. The purpose of this section is thus to form a datum, from which the effects of H_2 addition on an exhaust diluted engine may be measured.

4.3.1 Output Torque

In an SI engine, torque is typically controlled by limiting the amount of air/fuel mixture that is inducted per cycle by means of a throttle valve. The use of EGR results in a similar torque reduction through its direct displacement of air/fuel mixture which would have otherwise been combusted. The effect of EGR on IMEP is illustrated in Figure 4.9.

Here it is shown that a reduction in IMEP of 12.9% is achieved (at wide open throttle) solely through the use of EGR without any appreciable loss of combustion stability. As torque control is normally achieved through throttling, there is an appreciable loss in η_{fc} associated with a reduction in IMEP. Thus the accomplishment of any reduction in IMEP without the use of a flow restriction is desired as efficiency losses are largely negated. The effects of EGR on η_{fc} are discussed further in Section 4.3.3. As the EGR fraction is increased beyond 15%, the IMEP drops sharply due to the onset of partial burn and misfiring cycles, negatively affecting THC and CO emissions as well as η_{fc}.

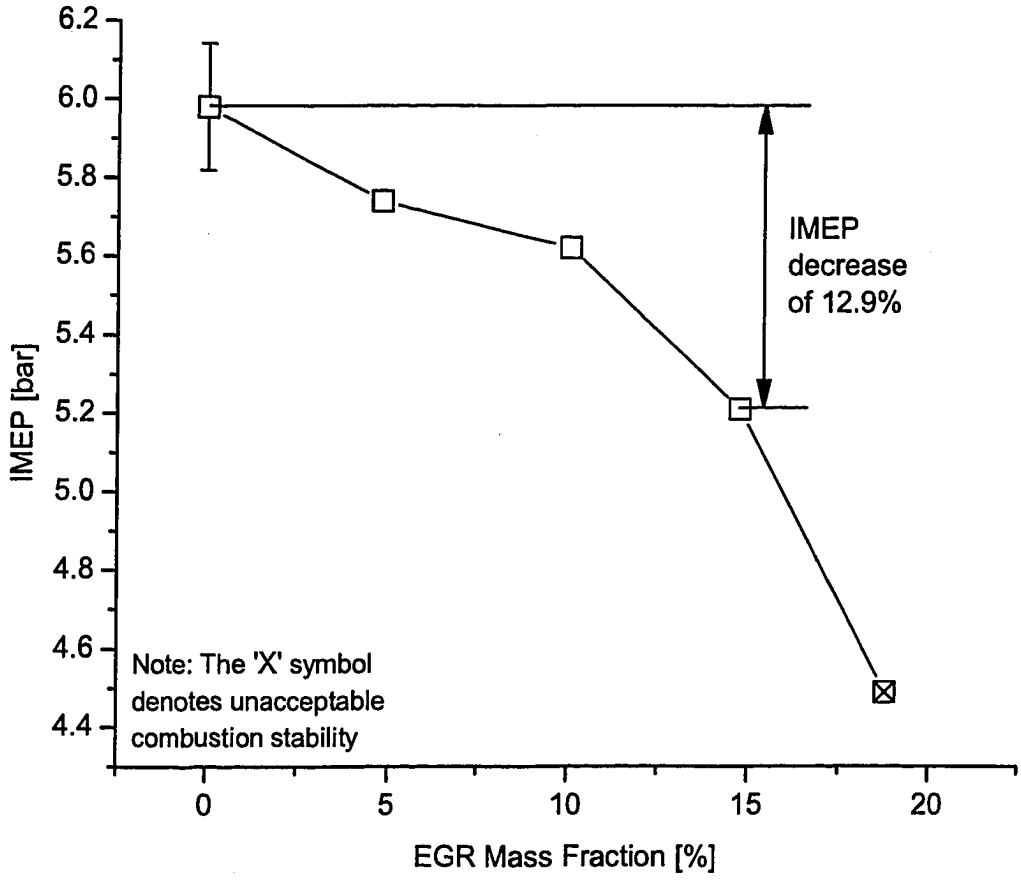

Figure 4.9: The effect of EGR on IMEP. The error bar represents a 95% confidence interval for an undiluted base condition. The symbol containing an 'X' indicates that the COV IMEP has exceeded the upper error bound of the undiluted base condition (6.54%) and the combustion stability is thus considered unacceptable.

4.3.2 Combustion Stability

Combustion stability is a measure of the magnitude of cycle-to-cycle variations both in the development and propagation of the flame. These variations can be attributed to a great number of mechanisms, many of which are affected by the addition of EGR (Ozdor et al., 1994).

One of the known effects of EGR addition is the observed decrease in mixture laminar burning velocity. Experiments have been performed in combustion chambers that have demonstrated a decrease in laminar burning velocity with the addition of simulated exhaust gas products (Gat and Kauffman, 1980; Stone et al., 1998; Elia et al., 2001). The laminar burning velocity is an important characteristic of a mixture as it governs the initial stages of flame kernel development.

Until the flame kernel has reached the size of the turbulent eddies present in the cylinder, its growth is dictated by the laminar burning velocity of the mixture (Lancaster et al., 1976). It is during this development stage where the flame kernel is vulnerable to subtle changes in local mixture composition and flow field characteristics, as evidenced by cycle-to-cycle variations which occur at ideal operating conditions without the presence of EGR (Gatowski et al., 1984). And seeing as the temporal history of the flame kernel acts as the underpinning for the remaining flame development and propagation, it is desirable to ensure that the development of the flame kernel is consistent and prompt. Any delay in flame kernel growth represents additional opportunity for the kernel to be convected away from the electrode, resulting in varying flame characteristics and thus development times (Matekunas, 1983). Therefore, a reduced laminar burning velocity is not desirable if cycle-to-cycle variations are to be minimized.

This is illustrated in a previous study that found significant variation in the rate of flame kernel growth in the presence of EGR (Cho et al., 1992). While a change in spark timing can be sufficient to maintain a suitable combustion phase for a decreased burning velocity, it is not adequate to eliminate cycle-to-cycle variations in flame kernel development. Uncertainty in flame kernel development is compounded with the addition of EGR, not only through an increase in development time, but also with additional variation in local mixture composition. Using a specially designed sampling system, composition measurements have been made of the mixture in the vicinity of the spark gap. It has been determined that the addition of EGR results in greater cycle-to-cycle variation of both hydrocarbon and CO_2 concentra-

tion within the spark gap (Matsui et al., 1979). Although not included in this study, it can be extended that increased variation in mixture composition near the spark plug would result in increased cycle-to-cycle variability through reductions in laminar burning velocity.

Subsequent to the development of the flame kernel, the flame propagation is governed by the turbulent burning velocity. During this stage, mixture inhomogeneities and the presence of EGR have a lesser effect on cycle-to-cycle variations. It has been shown that the decreased rate of flame propagation associated with a 'slow burn' engine can be compensated for by maintaining an MBT spark timing without significantly affecting the angles at which either 50% mass fraction had burned or maximum cylinder pressure occurred (Matekunas, 1983). Thus, a change in burning velocity is not necessarily affecting cycle-to-cycle variations, assuming that a suitable combustion phase has been maintained with an adjustment in spark timing. The effect of EGR fraction on MBT spark timing in this study is shown in Figure 4.10. Here it is shown that the addition of EGR requires an advance in spark timing to accommodate the increased combustion duration while maintaining MBT. Another study has shown that the ratio of turbulent to laminar burning velocity (S_L/S_T) rises with both increased EGR fraction and turbulence intensity (Gat and Kauffman, 1980). Thus, at a given turbulence intensity, the addition of EGR does not significantly affect the turbulent burning velocity. The changes in spark advance required to maintain MBT spark timing in Figure 4.10 are then likely due to the effect of EGR on flame kernel development where S_L is a governing factor.

The effect of EGR on combustion stability in this study is illustrated in Figure 4.11. It is shown that the COV IMEP remains within the error bounds of the undiluted base condition until the EGR mass fraction exceeds 15%. As the fraction of EGR is increased further to 19%, the COV IMEP sharply increases to 36% as a result of partial burn and misfiring cycles. The variation in pressure history for both an undiluted mixture and a 19% EGR fraction is shown in Figure 4.12. The disparity in combustion stability is apparent in the additional variance in peak pressure for the dilute mixture as shown in Figure 4.12(b). What is not apparent in Figure 4.12 are the partial burn and misfiring cycles which are ultimately increasing the value of COV IMEP for the dilute mixture. A histogram of COV IMEP values for the same 100 consecutive engine cycles displayed in Figure 4.12 is shown in Figure 4.13. Here a 19% EGR mass fraction is shown to have resulted in an

approximate 10% misfire[2] rate and a decrease in mean IMEP of 25%. The presence of partial burn cycles is also visible in Figure 4.13(b) near an IMEP of 3 bar.

4.3.3 Fuel Conversion Efficiency

The addition of EGR affects the η_{fc} of an SI engine through several mechanisms. Those that act to improve η_{fc} include reductions in pumping (at constant load), cooling and dissociation losses, whereas η_{fc} is decreased through a reduction in the degree of constant volume combustion and an increase in cycle-to-cycle combustion variations (Nakajima et al., 1981).

However, it is important to note that the reduction in pumping losses through the addition of EGR is only observed when comparing constant load conditions. Thus, pumping losses are not expected to have an effect on η_{fc} for this study as all tests were performed at wide open throttle (WOT). This is partially revealed in Figures 4.14 and 4.15 which show the effect of EGR mass fraction on η_{fc} and exhaust gas temperature respectively. It is seen that both η_{fc} and exhaust gas temperature stay relatively constant until 15% EGR, at which point both decrease. As a reduction in pumping losses is not applicable in this case, it is presumed that there are additional competing mechanisms which are causing η_{fc} and exhaust gas temperature to remain relatively constant while combustion stability is acceptable.

Additional mechanisms which act to raise η_{fc} after the addition of EGR are due to a reduced mixture energy density, which results in decreased peak cylinder temperatures. This has two effects in improving η_{fc}: first, reduced peak temperatures equate to reduced heat losses to the cylinder walls; second, the amount of energy diverted to temperature dependent endothermic dissociation reactions decreases. However, the addition of EGR also results in mechanisms which act to reduce η_{fc}, creating increased cyclical variations in flame development and a decrease in constant volume combustion. The competition between these mechanisms results in the observed trends of relatively constant η_{fc} and exhaust gas temperature as shown in Figures 4.14 and 4.15. A previous study has also shown that for slow burn engines at moderate loads (as in this study), any gains in η_{fc} resulting from the use of EGR are minimal (Nakajima et al., 1981).

[2]A misfire is defined as an IMEP value less than zero.

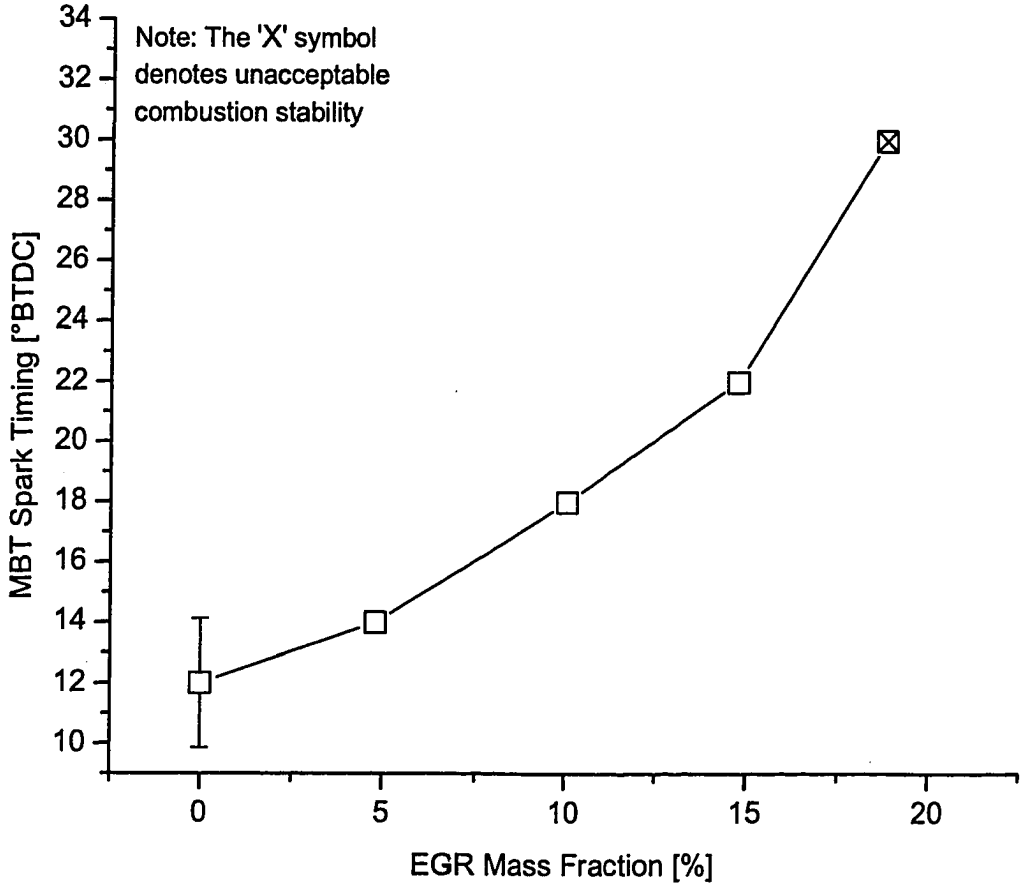

Figure 4.10: The effect of EGR on MBT spark timing. The error bar represents a 95% confidence interval for an undiluted base condition. The symbol containing an 'X' represents that the COV IMEP has exceeded the upper error bound of the undiluted base condition (6.54%) and the combustion stability is thus considered unacceptable.

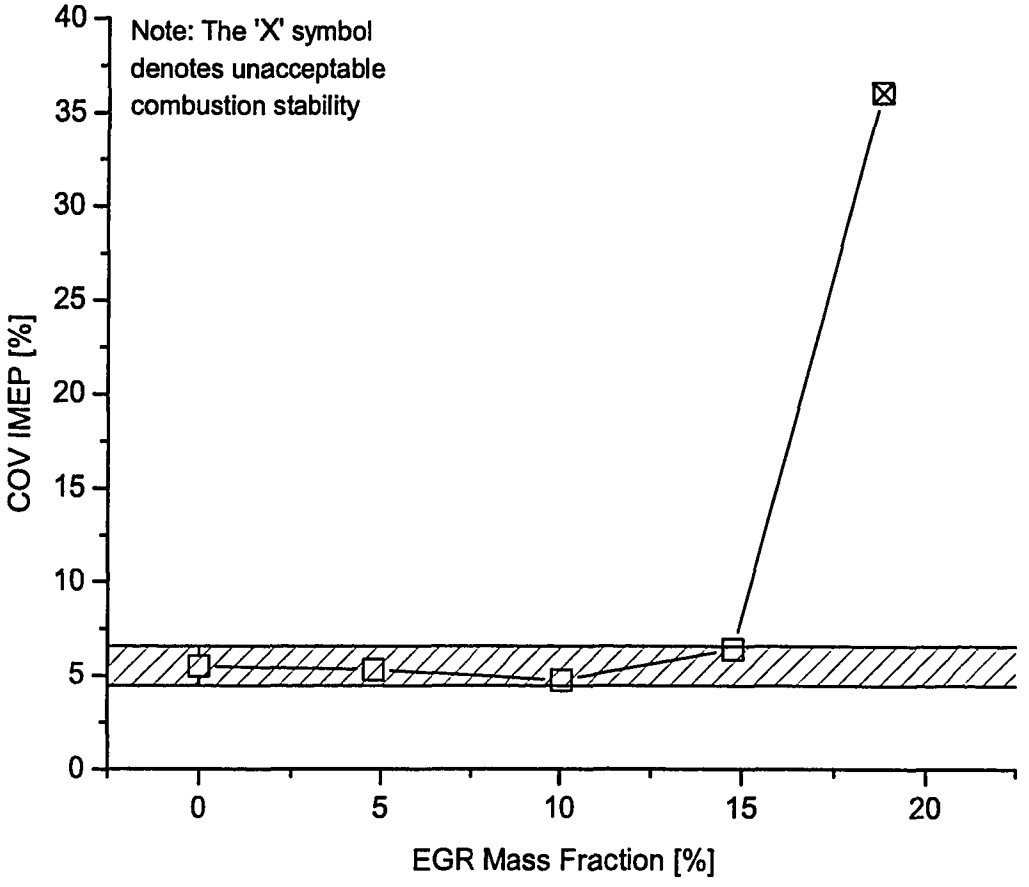

Figure 4.11: The effect of EGR on COV IMEP. The error bar represents a 95% confidence interval for an undiluted base condition. The symbol containing an 'X' represents that the COV IMEP has exceeded the upper error bound of the undiluted base condition (6.54%) and the combustion stability is thus considered unacceptable.

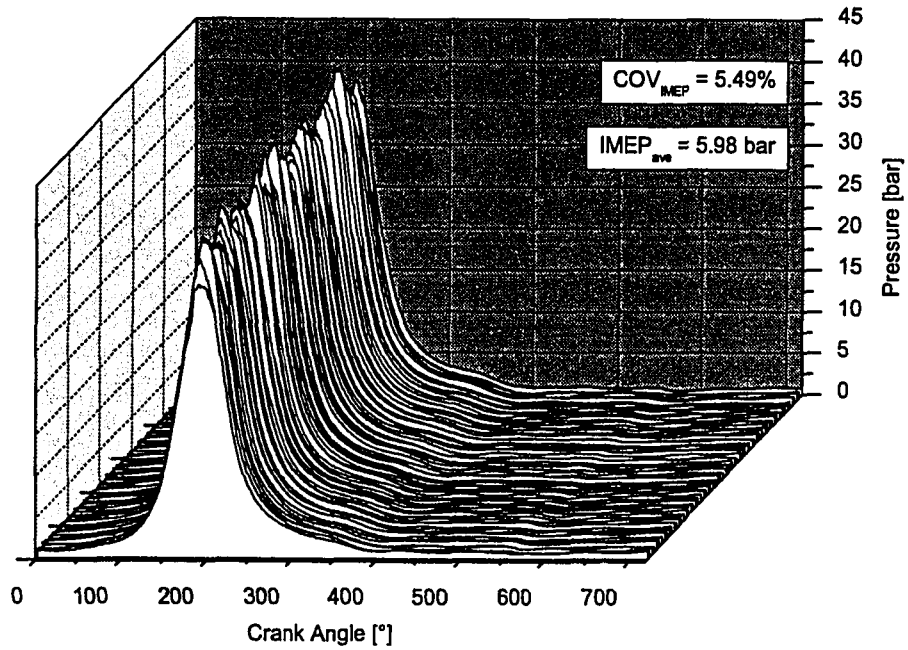

(a) $0\%_{mass}$ EGR

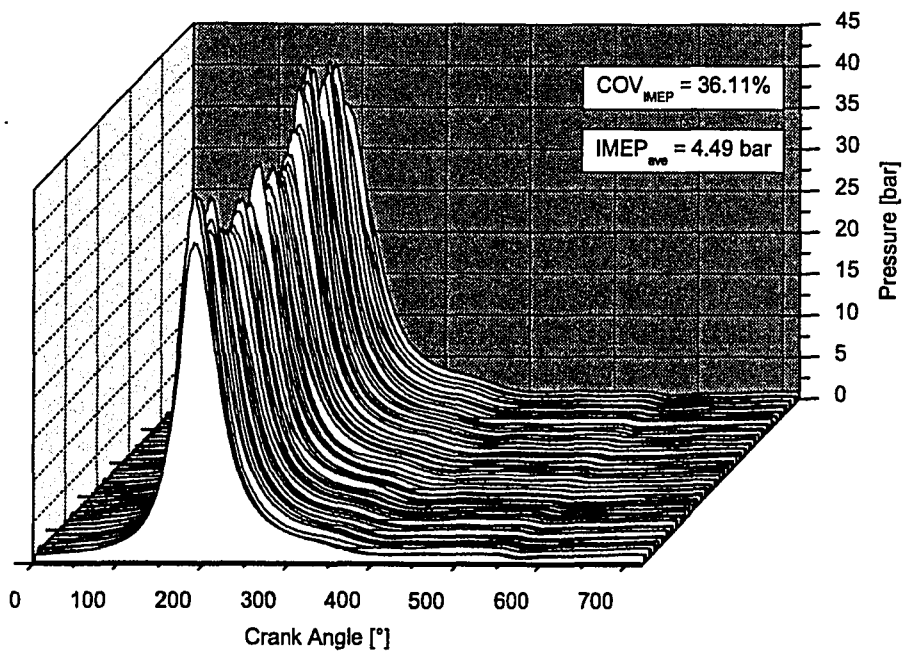

(b) $19\%_{mass}$ EGR

Figure 4.12: The effect of EGR on cylinder pressure history is shown in 100 consecutive cylinder pressure traces.

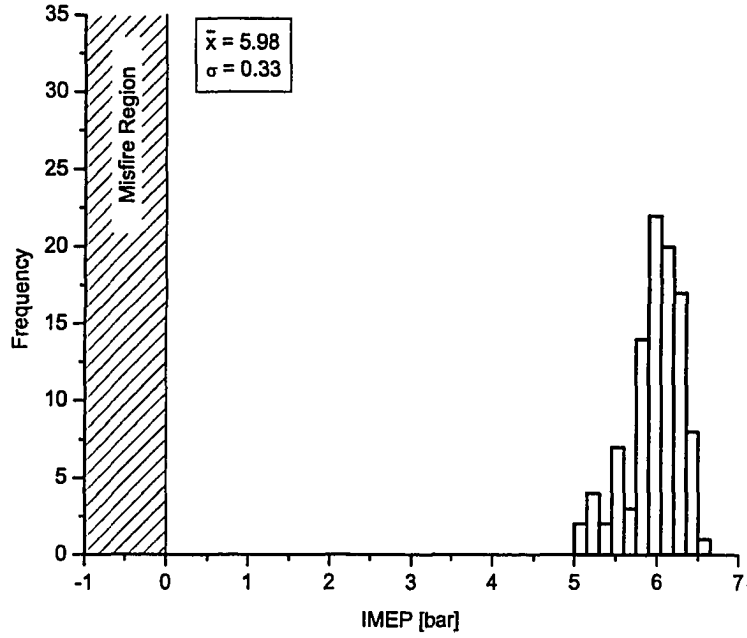

(a) $0\%_{mass}$ EGR

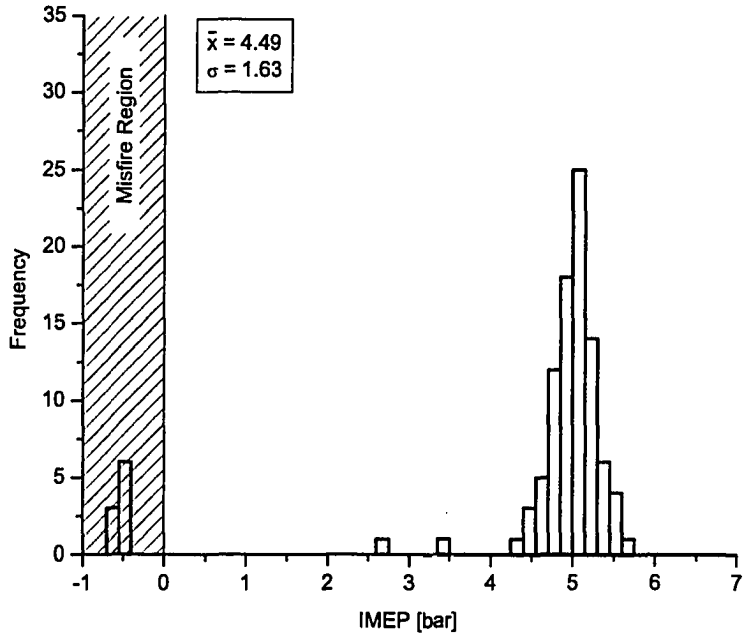

(b) $19\%_{mass}$ EGR

Figure 4.13: The effect of EGR on the distribution of IMEP. Data is shown for 100 consecutive engine cycles.

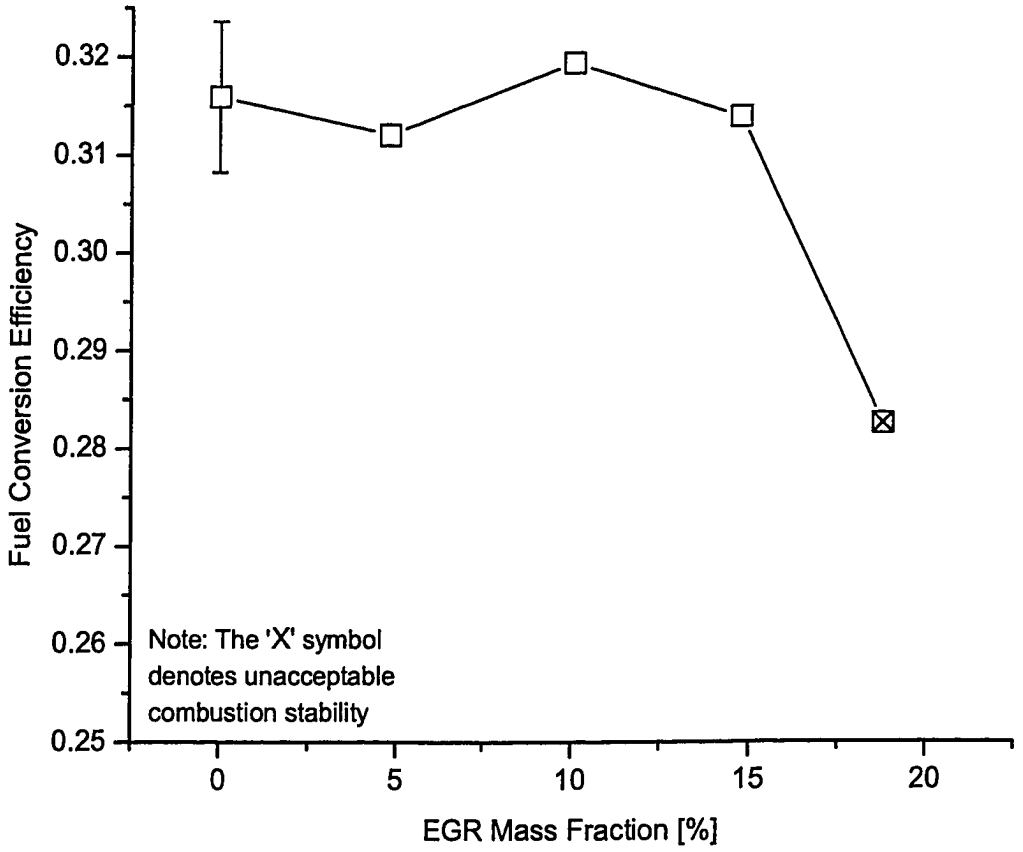

Figure 4.14: The effect of EGR on fuel conversion efficiency. The error bar represents a 95% confidence interval for an undiluted base condition. The symbol containing an 'X' indicates that the COV IMEP has exceeded the upper error bound of the undiluted base condition (6.54%) and the combustion stability is thus considered unacceptable.

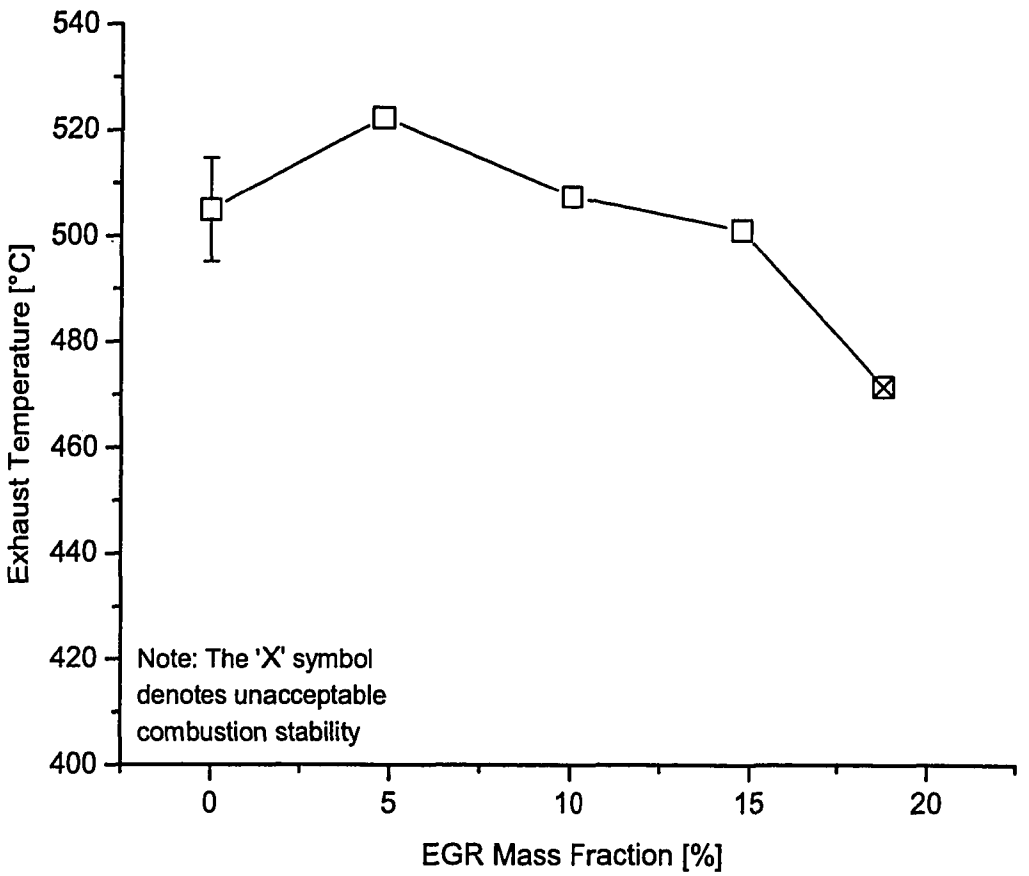

Figure 4.15: The effect of EGR on exhaust temperature. The error bar represents a 95% confidence interval for an undiluted base condition. The symbol containing an 'X' indicates that the COV IMEP has exceeded the upper error bound of the undiluted base condition (6.54%) and the combustion stability is thus considered unacceptable.

4.3.4 Pollutant Emissions

The use of EGR is one of the most effective methods to obtain significant reductions in NO emissions in SI engines and its use is widespread in production engines. EGR also has a smaller effect on both CO and THC emissions.

4.3.4.1 Nitric Oxide

As discussed in Section 4.2.4.1, it is commonly known that the formation of NO in SI engines depends on both temperature and O_2 availability. Previous studies have shown that the production of NO is kinetically controlled and that concentrations remain 'frozen' above equilibrium values early in the expansion stroke (Lavoie et al., 1970). As the kinetics that govern NO production are exponentially dependent upon temperature, any factor which affects the time-history of temperature or O_2 concentration will have an impact on NO emissions.

The addition of EGR, as was discussed in Section 4.3.3, results in decreased peak temperatures through a decrease in the energy density of the cylinder contents. The effect of various diluents on the formation of NO has been investigated and it has been determined that the reduction in NO emissions is proportional to the product of the mass flow rate and specific heat of the diluent (Quader, 1971). The reduction in NO emissions as a result of EGR dilution is shown for this study in Figure 4.16. Here it is shown that a reduction of 81% in indicated specific NO (ISNO) emissions, from 8.0 to 1.5 g/kW h, was achieved while maintaining suitable combustion stability. While NO emissions were reduced further, to 1.0 g/kW h at 19% EGR, the associated drop in combustion stability had an adverse effect on torque output, η_{fc} and THC emissions.

4.3.4.2 Carbon Monoxide

The formation of CO, as discussed in Section 4.2.4.2, is equilibrated throughout the combustion process and only becomes rate controlled through the later stages of the expansion stroke (Heywood, 1988, pp. 592-596). Thus the temperature time-history through the expansion and exhaust strokes plays a role in both the equilibrium concentration of CO and the subsequent amount of post combustion oxidation which occurs. Thus, as discussed in Section 4.3.3, the addition of EGR results in a lower temperature time-history during the early stages of the expansion stroke and, because of the increase in

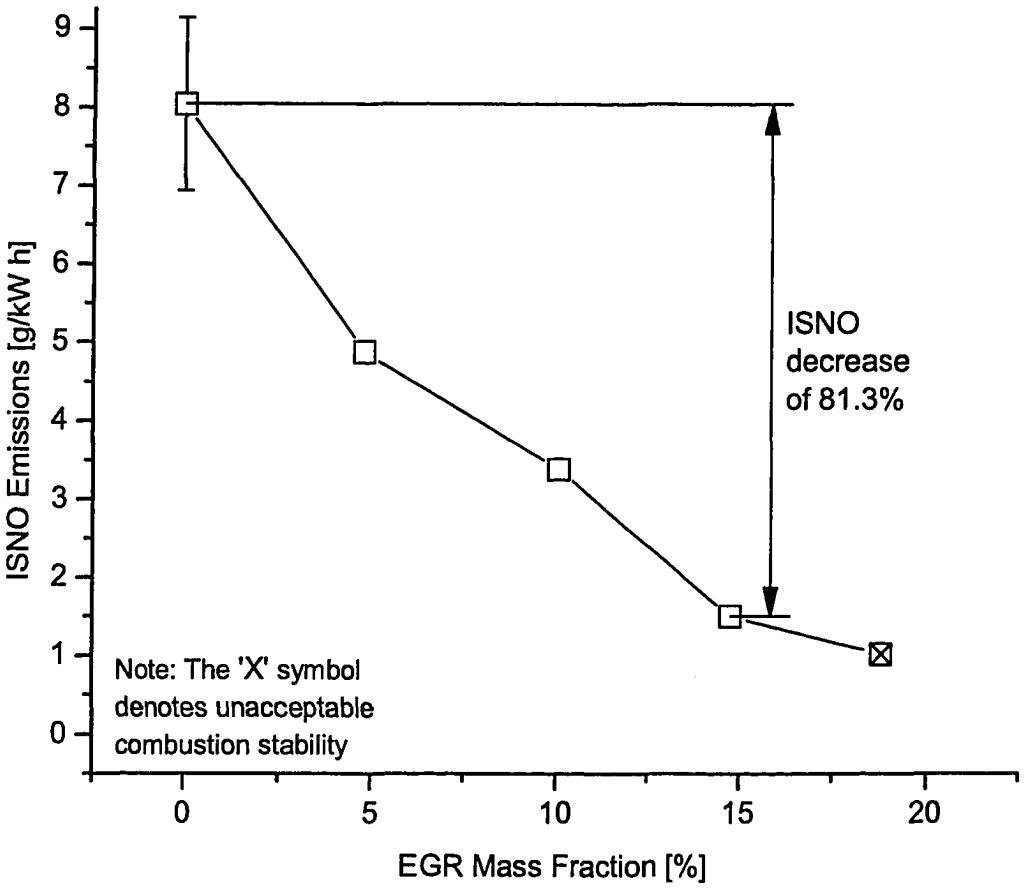

Figure 4.16: The effect of EGR on ISNO emissions. The error bar represents a 95% confidence interval for an undiluted base condition. The symbol containing an 'X' indicates that the COV IMEP has exceeded the upper error bound of the undiluted base condition (6.54%) and the combustion stability is thus considered unacceptable.

bulk heat capacity and reduction in heat transfer to the cylinder wall, sustained elevated temperatures through the later stages of the expansion stroke and exhaust stroke. It may then be presumed that an increase in EGR will result in lower equilibrium CO concentrations during combustion and similar levels of post combustion oxidation as a result of a sustained temperature throughout the expansion and exhaust strokes.

The effect of EGR on indicated specific CO (ISCO) emissions for this study is shown in Figure 4.17. Here CO emissions have been reduced by 35%, from 6.9 to 4.5 g/kW h. However, this trend is only slightly outside the uncertainty in CO measurements thus requiring further experiments to confirm. As the EGR fraction is raised to 19%, the influence of slow burning and misfiring cycles is evident in the rise in CO emissions. Also note that these are specific emissions and so any reduction in torque compounds an increase in emission concentration.

4.3.4.3 Total Hydrocarbons

As stated in Section 4.2.4.3, the crevice mechanism is the primary source for THC emissions (assuming that the engine is operating without partial burn or misfire cycles). During the expansion stroke, as in-cylinder pressure decreases and unburned mixture is released from the crevice volume, the amount of post combustion oxidation that occurs is what ultimately determines the amount of THC emissions. Thus any change in factors which affect either the mass of hydrocarbons compressed into the crevice volume or the level of post combustion oxidation which occurs afterward, will have an effect on THC emissions.

To demonstrate the improvement in pumping losses as a result of EGR addition, many studies performed testing at a constant load with MBT spark timing. As the EGR fraction is increased at a constant load, and MBT spark timing is maintained, the total mass inducted into the engine cylinder is increased and thus peak pressures also increase (Nakajima et al., 1981). As stated above, increased peak cylinder pressures also increase the mass of unburned mixture which is compressed into crevice volumes, thus requiring greater levels of post combustion oxidation to maintain similar levels of THC emissions.

The addition of EGR has been found to negatively affect factors which reduce post combustion oxidation. A previous study has found that, in the absence of slow burn and misfire engine cycles, two factors play a role in

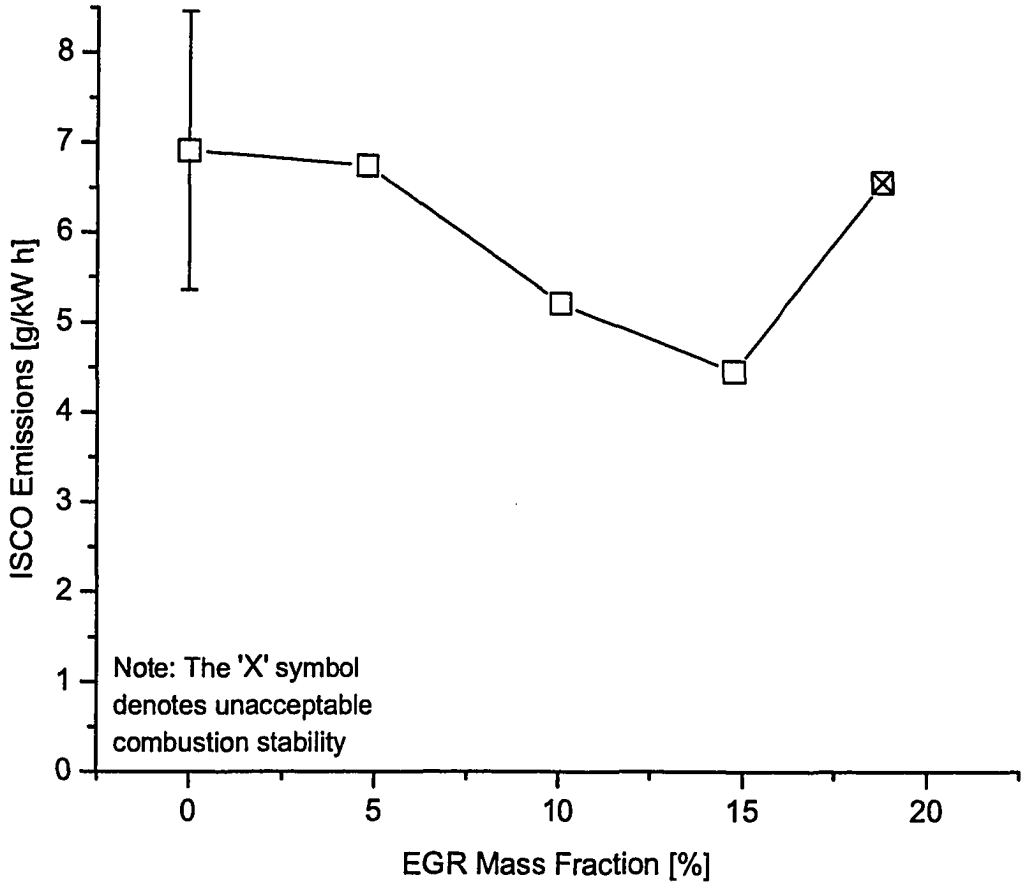

Figure 4.17: The effect of EGR on ISCO emissions. The error bar represents a 95% confidence interval for an undiluted base condition. The symbol containing an 'X' indicates that the COV IMEP has exceeded the upper error bound of the undiluted base condition (6.54%) and the combustion stability is thus considered unacceptable.

determining engine-out THC emissions: first, the post combustion temperature time-history which affects rates of post combustion oxidation; second, the reactivity of the post combustion gases which may be altered with the addition of EGR, also resulting in varying levels of post combustion oxidation (Jääskeläinen and Wallace, 1994). This study also found that, with sufficient increases in combustion duration, it is possible to negate the dilution effects of EGR and obtain an increase in THC emissions with an *increase* in exhaust temperature. Assuming an absence of partial burn and misfiring cycles, this finding confirms that the oxidative environment of post combustion gases is compromised with the addition of EGR, thus resulting in increased THC emissions. As the EGR fraction is increased further, the onset of partial burn and misfiring cycles results in a sharp increase in specific THC emissions, as a result of both increased THC concentration and reduced engine torque output.

The indicated specific THC (ISTHC) emissions as a result of EGR fraction are shown in Figure 4.18 for this study. Here it is shown that THC emissions remain relatively constant until the onset of partial burn cycles at an EGR fraction of 15%. As the EGR fraction is increased further to 19%, THC emissions increase sharply due to the presence of slow burn and misfiring cycles.

4.4 The Effect of H_2 Addition on Exhaust Diluted Engine Performance

Having established a datum of diluted engine performance in Section 4.3, the use of H_2 as a means of restoring combustion stability and extending the dilution limit is investigated. The goal of this study was to determine the minimum amount of H_2 required to maintain an undiluted combustion stability at each EGR fraction. H_2 addition is only applied at EGR fractions where the COV IMEP exceeded the upper error bound of the undiluted condition. The amount of H_2 used is presented as a H_2 energy fraction (HEF). Using the lower heating value (LHV) of each fuel, the HEF is equivalent to the fraction of total fuel energy that was provided by H_2.

There exists a distinct dichotomy in the use of H_2 as an SI engine fuel: several of its physical properties give it a marked advantage over conventional fuels while these same properties necessitate specialized infrastructure and safety measures to be developed and used. A comparison of applicable physical properties of H_2 and CH_4 is given in Table 4.3. Any properties spe-

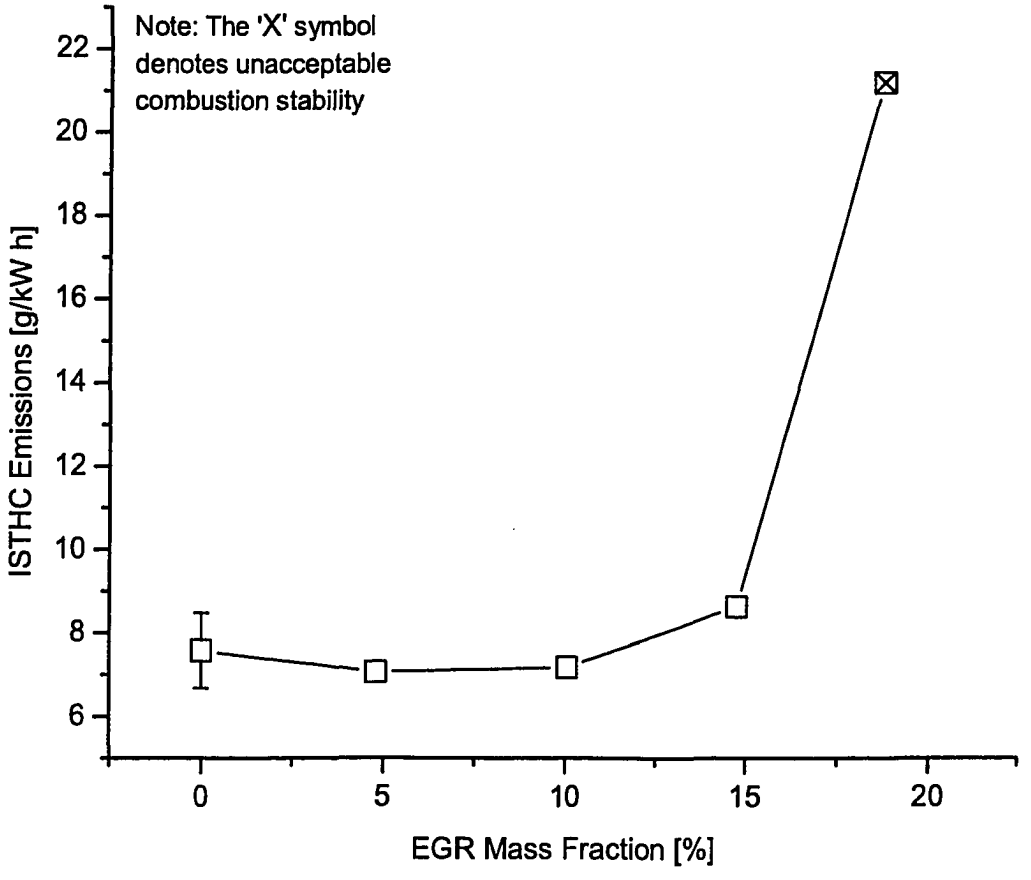

Figure 4.18: The effect of EGR on ISTHC emissions. The error bar represents a 95% confidence interval for an undiluted base condition. The symbol containing an 'X' indicates that the COV IMEP has exceeded the upper error bound of the undiluted base condition (6.54%) and the combustion stability is thus considered unacceptable.

cific to the natural gas used in this study are given in place of CH_4 and are indicated as such.

4.4.1 Output Torque

As noted in Table 4.3, H_2 has a very high LHV (119.93 MJ/kg) and a very low density (0.0838 kg/m^3) when compared with natural gas and all other gaseous fuels. This results in equivalent volumes having much less energy and equivalent masses having much more energy than other gaseous fuels. However, the stoichiometric air/fuel ratio (by mass) of H_2 is roughly double that of natural gas, resulting in values of volumetric energy density (VED) of stoichiometric mixtures which vary by only 7% between the two fuels. Previous studies have shown that this difference in VED results in a loss in IMEP, when H_2 is added to a natural gas fuelled SI engine (Nagalingam et al., 1983).

However, in this study H_2 is only added when combustion instability has increased beyond the undiluted base condition, as caused by the onset of slow burn and misfire cycles. As was discussed in Section 4.3.2, the addition of EGR reduces laminar burning velocity and thus increases both flame kernel development time and cycle-to-cycle variations in flame development. Thus the addition of H_2 is used to restore the original combustion stability by increasing the mixture laminar burning velocity. The difference in stoichiometric VED between the two fuels does not have as significant an effect on performance as does the exclusion of slow and partial burn cycles. Thus the addition of H_2 results in an increased IMEP at each EGR fraction, as shown in Figure 4.19. Here it is seen that a reduction in IMEP of 30% at WOT is possible with the use of a 17% HEF and a 30% EGR mass fraction, while still maintaining suitable combustion stability.

4.4.2 Combustion Stability

H_2 addition is a means of restoring suitable combustion stability through the maintenance of a consistent and prompt flame kernel development period. The lack of a stable flame kernel development undermines other measures of engine performance, including torque output, efficiency and emissions (Ozdor et al., 1994).

As was discussed in Section 4.3.2, the use of EGR results in greater cycle-to-cycle variations in flame kernel development through an observed reduc-

Table 4.3: Physical Properties of H_2 and CH_4

Property	H_2	CH_4
Density at NTP [kg/m^3][1,2,3]	0.0838	0.6966
Lower heating value (LHV) [MJ/kg][2,3]	119.93	49.82
Volumetric fuel/air ratio of stoichiometric mixture at NTP [m^3/m^3][1,2,3]	0.2950	0.1004
Stoichiometric air/fuel ratio [kg/kg][3]	34.3	17.2
Volumetric energy density (VED) of stoichiometric mixture at NTP [kJ/m^3][1,3,4]	2913	3133
Diffusion coefficient in air at NTP [cm^2/s][1,2]	0.63	0.16
Combustion range [$\%_{vol}$ in air][2]	4-75	5.3-1.5
Minimum ignition energy in air [mJ][2]	0.02	0.29
Quenching distance at 1 atm [cm][2]	0.060	0.203
Laminar burning velocity in air at NTP [cm/s][1,2]	265-325	37-45

[1] NTP conditions are 293 K and 101.3 kPa
[2] (Das, 1996)
[3] Atco Gas Daily Analysis, 2003-11-25
[4] (Bauer, 1999)

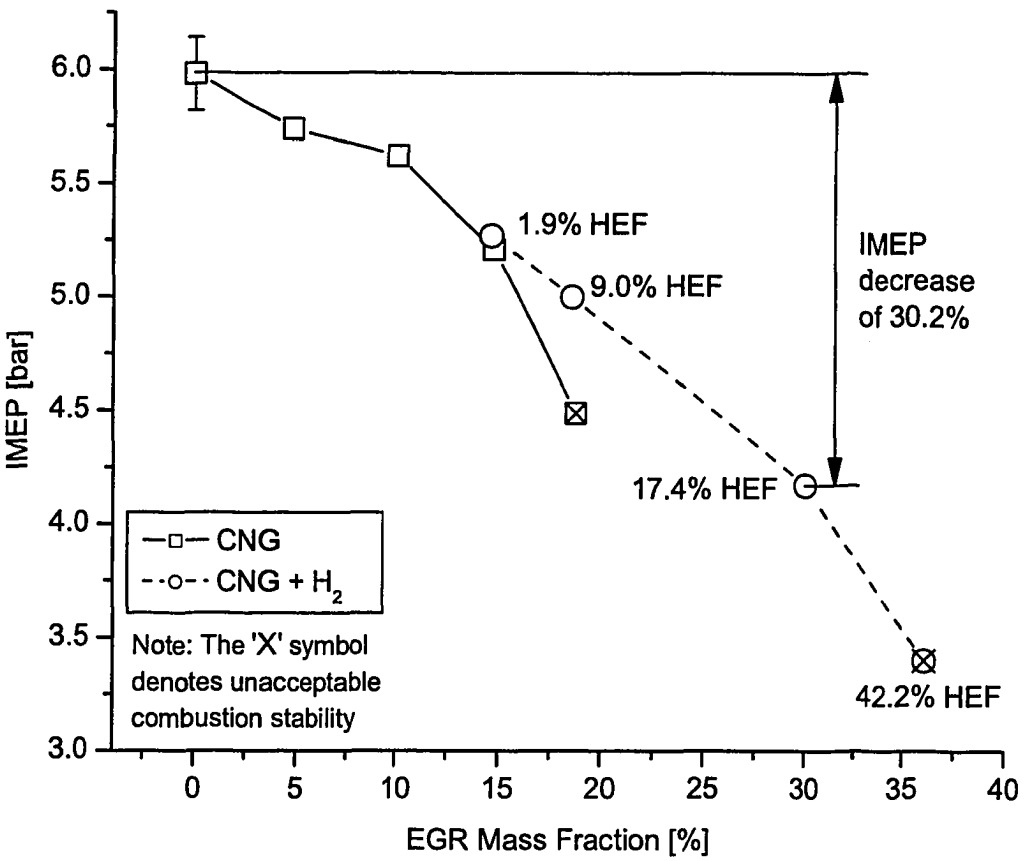

Figure 4.19: The effect of H_2 addition on exhaust diluted IMEP. The amount of H_2 employed at each point is listed as a H_2 energy fraction (HEF). The error bar represents a 95% confidence interval for an undiluted base condition. The symbols containing an 'X' indicate that the COV IMEP has exceeded the upper error bound of the undiluted base condition (6.54%) and the combustion stability is thus considered unacceptable.

tion in mixture laminar burning velocity and fluctuations in mixture composition within the spark gap. Thus, to restore combustion stability, it is necessary to reduce flame kernel development time and ensure that there is a homogeneous mixture composition within the spark gap, or at least make any mixture inhomogeneities irrelevant to the development of the flame kernel.

A previous study investigated the effect of H_2 addition on the combustion phases of a CFR engine operating with an indolene base fuel (Rauckis and Mclean, 1979). The combustion phases were split into three categories: 0 to 2 percent mass fraction burned (kernel growth duration); 2 to 10 percent mass fraction burned (flame development duration); and 10 to 90 percent mass fraction burned (combustion duration). It was found that the addition of H_2 causes a significant reduction in kernel growth duration, with a progressively lesser effect on both the flame development and combustion durations. The reduction in kernel growth duration was a function of the amount of H_2 used and the equivalence ratio, with leaner mixtures and higher amounts of H_2 yielding the biggest reductions. For a stoichiometric mixture, the flame kernel growth duration was decreased by approximately 28%, from 9.9 to 7.2° CA, with a 15% HEF.

A subsequent study has compared the growth rate and cycle-to-cycle variation of flame kernel development for both C_3H_8 and H_2 using schlieren photography (Heywood and Vilchis, 1984). The shape of the developing H_2 flame kernel was more spherical and less irregular than that of C_3H_8. Further, the spatial distribution of the reaction zone was also shown to be more regular for the H_2 flame kernel. Cycle-to-cycle variations of the flame kernel development were much reduced for H_2, with the flame always staying centered at the spark plug electrode. It was concluded that while the in-cylinder flow conditions and residual gas inhomogeneities were comparable for both H_2 and C_3H_8, the faster development of the H_2 flame kernel resulted in less cycle-to-cycle variation in the rate and location of the flame development.

The decreased flame development period associated with H_2 is apparent in Figure 4.20 which shows the effect of H_2 addition on MBT spark timing. It is shown that at an equivalent EGR fraction, the addition of H_2 reduces the spark advance necessary to maintain MBT. At an EGR mass fraction of 19%, the use of a 9% HEF reduced the MBT spark timing by 40%, from 30°to 18° BTDC.

The resulting reduction in cycle-to-cycle variations in flame development associated with a shortened flame kernel growth duration is shown in Figure 4.21. While an increased EGR mass fraction decreases combustion stability,

Table 4.4: H_2 Required to Maintain Combustion Stability

EGR Mass Fraction [%]	HEF [%]	HVF [%]	HEF / EGR [-]
14.8	0	0	0
18.6	9.0	23.5	0.484
30.0	17.4	39.5	0.580

as was discussed in Section 4.3.2, the addition of H_2 acts to oppose this trend. Through the incremental addition of H_2, an undiluted combustion stability is maintained to an EGR mass fraction of 30%. The improvement of combustion stability through H_2 addition is also illustrated in Figure 4.22 as a comparison of the cylinder pressure time histories for two cases: 19% EGR with no H_2 and 19% EGR with a 9% HEF. The variation between adjacent cylinder pressure traces is shown to decrease with the addition of H_2. The IMEP values associated with these pressure traces are also shown as a histogram in Figure 4.23. It is clear that the addition of H_2 eliminates any misfiring or slow burning cycles, as evidenced by the 11% increase and 81% decrease in the respective mean and SSD values of IMEP.

The amount of H_2 required to sustain combustion stability at various levels of EGR dilution is given in Table 4.4.

4.4.3 Fuel Conversion Efficiency

As discussed in Section 4.3.3, the addition of EGR affects η_{fc} in an SI engine through several mechanisms: positively through the reduction of cooling and dissociation losses and negatively through an increase in cycle-to-cycle combustion variation and a reduced degree of constant volume combustion. The addition of H_2 to an exhaust diluted SI engine influences several of these mechanisms, mainly through the maintenance of the mixture laminar burning velocity.

The effect of H_2 addition on the η_{fc} of an EGR diluted SI engine is illustrated in Figure 4.24. It is shown that H_2 addition results in a relatively constant η_{fc} until a 19% EGR mass fraction, where a significant improvement in η_{fc} is shown for a HEF of 9%. As the EGR fraction increases to 30%, the η_{fc} gradually decreases to the lower error bound of the undiluted condition. Beyond an EGR fraction of 30%, the onset of slow burn and misfire cycles results in a sharp decrease in η_{fc}.

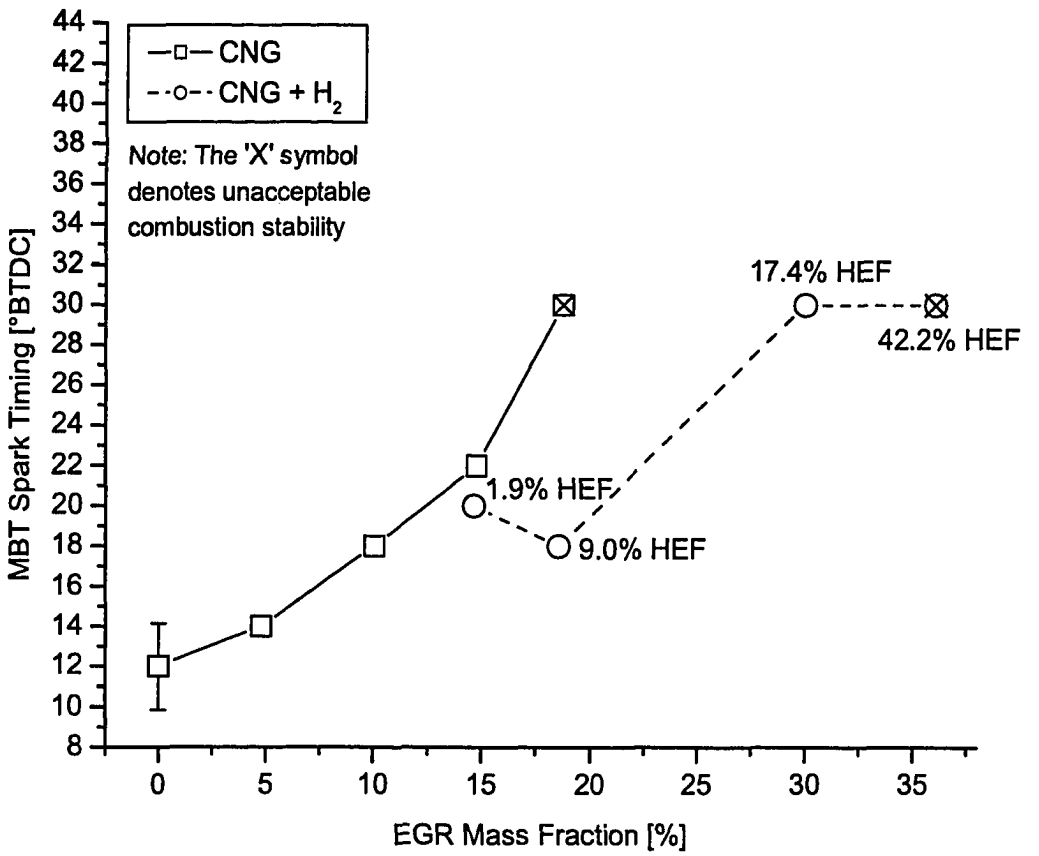

Figure 4.20: The effect of H_2 addition on exhaust diluted MBT spark timing. The amount of H_2 employed at each point is listed as a H_2 energy fraction (HEF). The error bar represents a 95% confidence interval for an undiluted base condition. The symbols containing an 'X' indicates that the COV IMEP has exceeded the upper error bound of the undiluted base condition (6.54%) and the combustion stability is thus considered unacceptable.

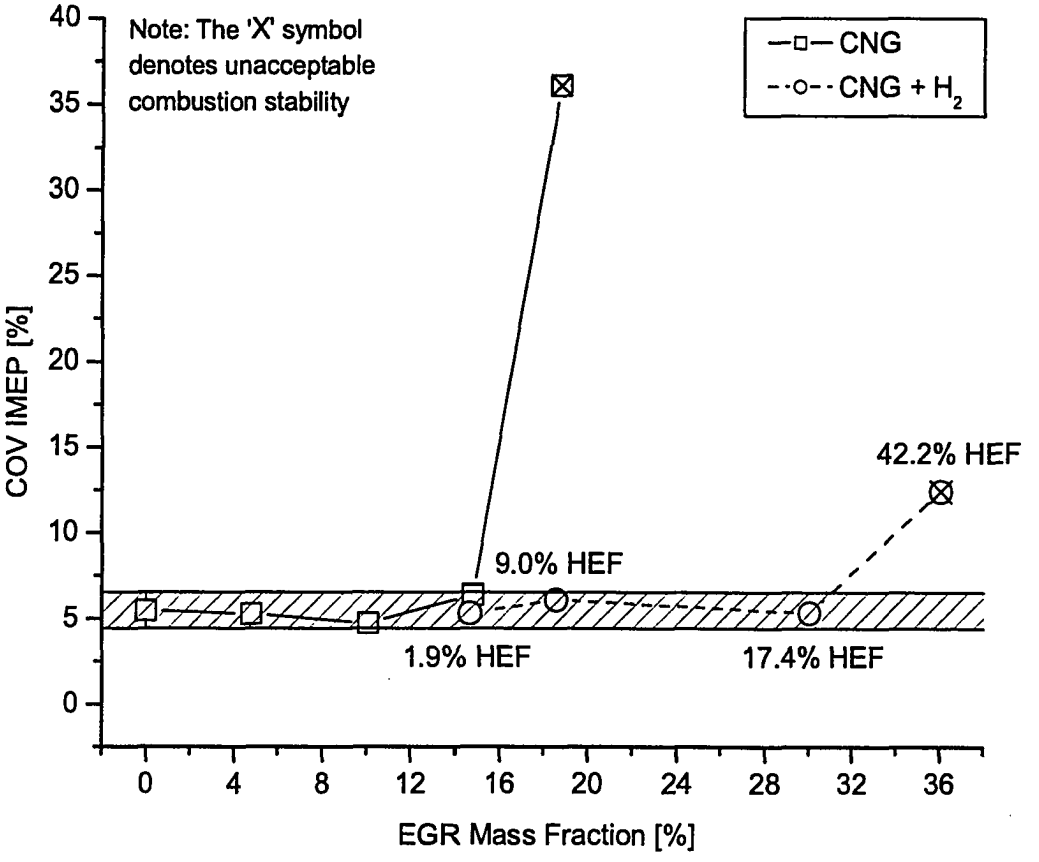

Figure 4.21: The effect of H_2 addition on exhaust diluted COV IMEP. The amount of H_2 employed at each point is listed as a H_2 energy fraction (HEF). The error bar represents a 95% confidence interval for an undiluted base condition. The symbols containing an 'X' indicates that the COV IMEP has exceeded the upper error bound of the undiluted base condition (6.54%) and the combustion stability is thus considered unacceptable.

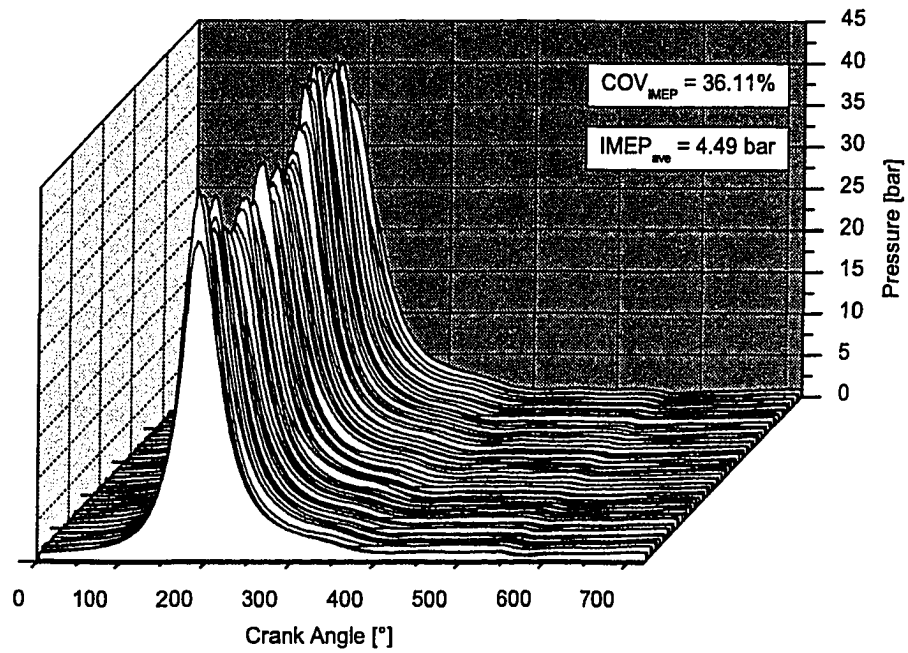

(a) 19%$_{mass}$ EGR, 0%$_{energy}$ H_2

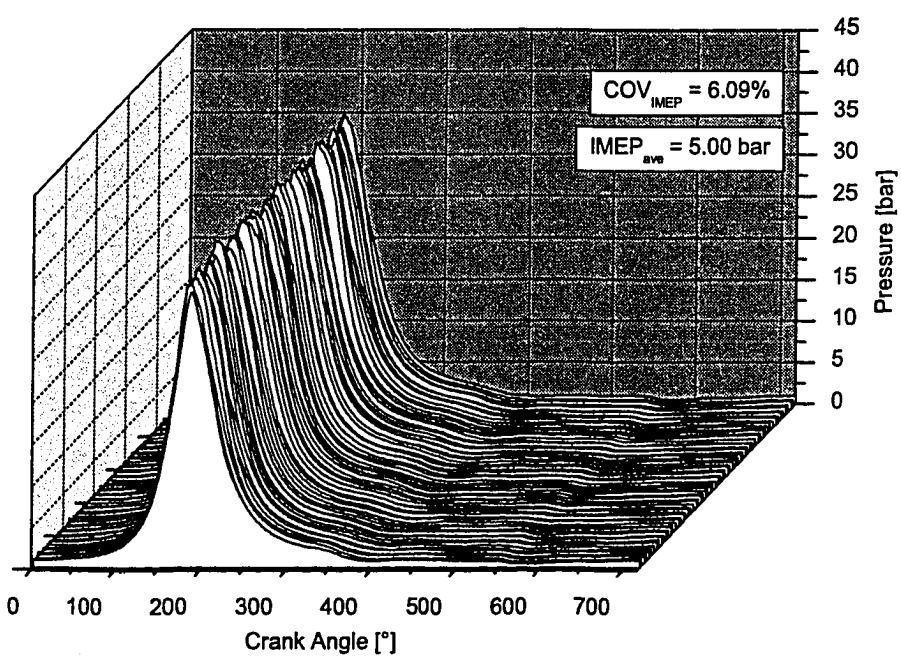

(b) 19%$_{mass}$ EGR, 9%$_{energy}$ H_2

Figure 4.22: The effect of H_2 addition on exhaust diluted cylinder pressure history is shown in 100 consecutive cylinder pressure traces.

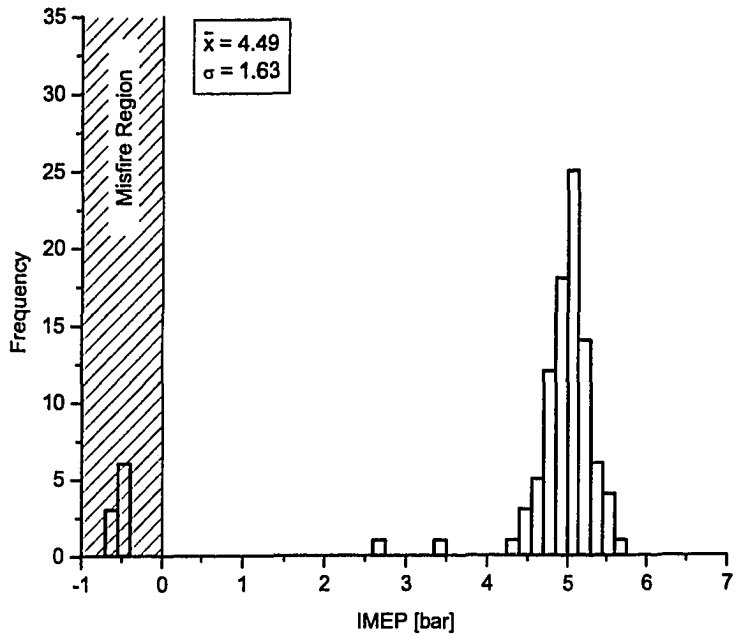

(a) $19\%_{mass}$ EGR, $0\%_{energy}$ H_2

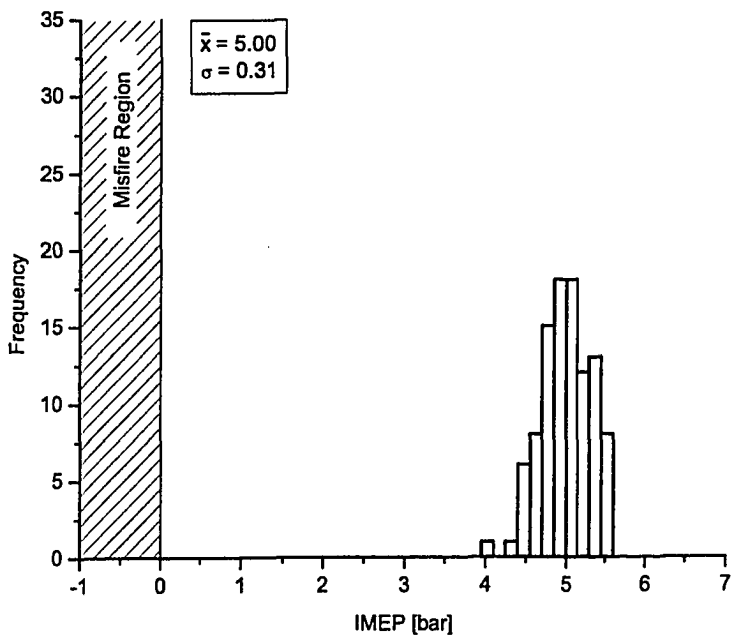

(b) $19\%_{mass}$ EGR, $9\%_{energy}$ H_2

Figure 4.23: The effect of H_2 addition on the distribution of exhaust diluted mean effective pressure. Data is shown for 100 consecutive engine cycles.

These trends in η_{fc} are also reflected in the exhaust gas temperature, which is given in Figure 4.25. As for η_{fc}, the exhaust gas temperature remains relatively constant up to a 19% EGR mass fraction, beyond which it decreases significantly. From 0 to 19% EGR, the constant values of η_{fc} and exhaust gas temperature suggest the following: the addition of H_2 is maintaining a constant flame propagation rate; the tendency for lower exhaust temperatures (through decreased bulk mixture energy density with EGR) is being balanced by the higher peak temperatures associated with H_2 combustion and increased burn duration. Beyond 19% EGR, the exhaust gas temperature decreases significantly while η_{fc} only shows a slight decrease. Here the decreased bulk mixture energy content dominates, thus resulting in a decrease in exhaust gas temperature. The slight decrease in η_{fc} is an indication that slow burn cycles are developing. As the EGR fraction further increases to 36%, sharp reductions in both η_{fc} and exhaust gas temperature indicate the presence of slow burn and misfire cycles.

4.4.4 Pollutant Emissions

While this section has been relegated to the end of the chapter, it is of significant importance. The combination of EGR dilution and H_2 addition in an SI engine operating stoichiometrically has very attractive emissions characteristics, further so upon application of a three-way catalytic converter. An additional subsection on indicated specific CO_2 ($ISCO_2$) emissions is also included to illustrate the benefits of H_2 supplementation on greenhouse gas emission reductions.

4.4.4.1 Nitric Oxide

The trend in NO emissions originally established in Figure 4.16 is extended to higher EGR mass fractions with the use of H_2 supplementation. While a previous study has found that H_2 supplementation causes increased NO emissions (Nagalingam et al., 1983), likely caused by the elevated peak temperatures associated with H_2 combustion, this effect is negated in this study through the use of large EGR fractions. Figure 4.26 shows that ISNO emissions are further reduced through the use of H_2 supplementation, to a minimum value of 0.10 g/kW h at an EGR fraction of 30% and a HEF of 17% while still maintaining suitable combustion stability. A further reduction in NO emissions, to less than 0.01 g/kW h, is achieved at 36% EGR with a

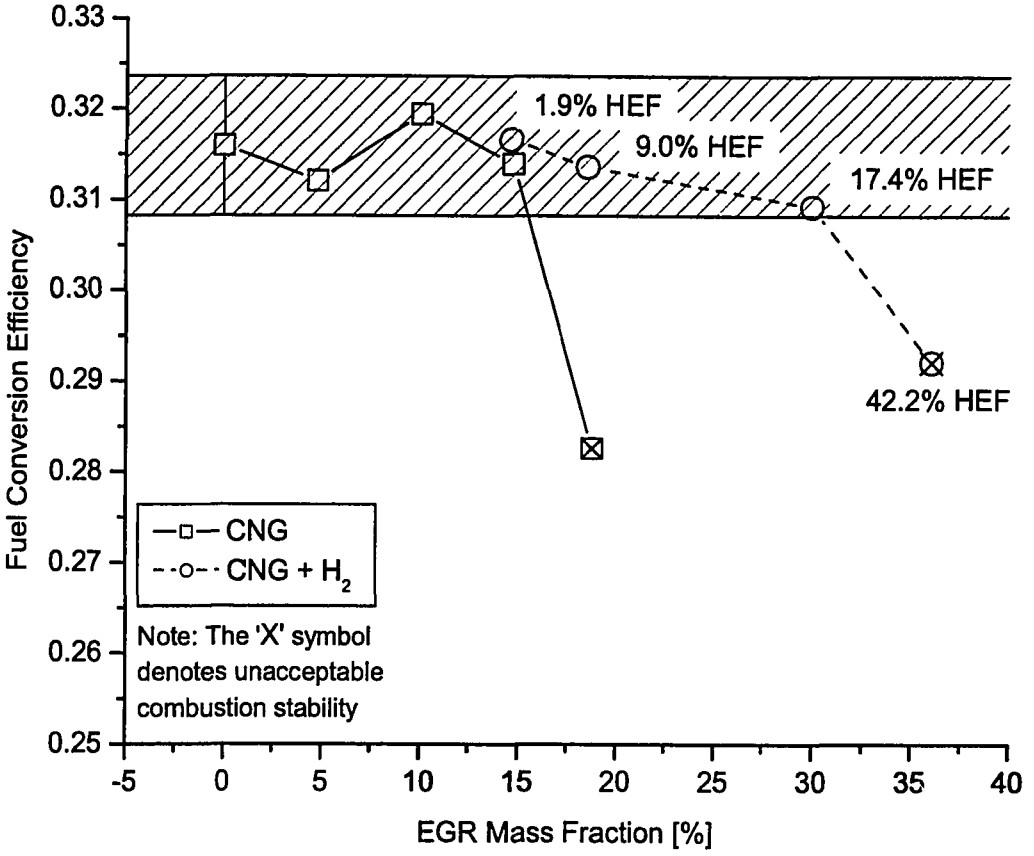

Figure 4.24: The effect of H_2 addition on exhaust diluted fuel conversion efficiency. The amount of H_2 employed at each point is listed as a H_2 energy fraction (HEF). The error bar represents a 95% confidence interval for an undiluted base condition. The symbols containing an 'X' indicate that the COV IMEP has exceeded the upper error bound of the undiluted base condition (6.54%) and the combustion stability is thus considered unacceptable.

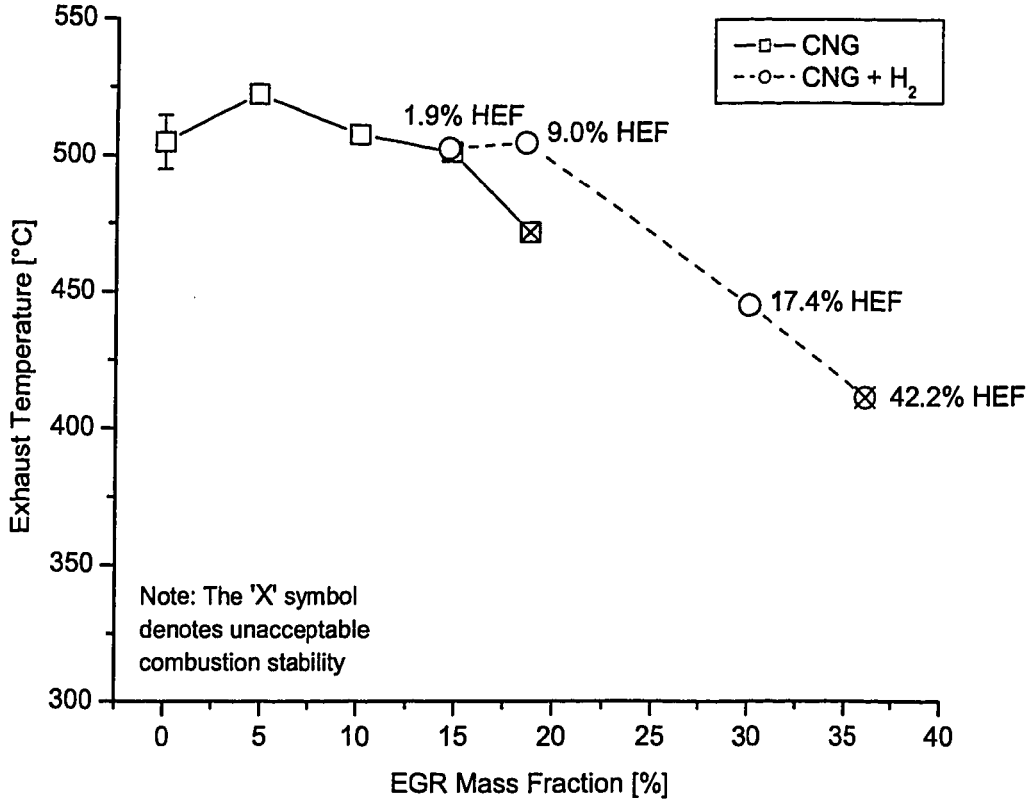

Figure 4.25: The effect of H_2 addition on exhaust diluted exhaust gas temperature. The amount of H_2 employed at each point is listed as a H_2 energy fraction (HEF). The error bar represents a 95% confidence interval for an undiluted base condition. The symbols containing an 'X' indicate that the COV IMEP has exceeded the upper error bound of the undiluted base condition (6.54%) and the combustion stability is thus considered unacceptable.

42% HEF. However, at this point combustion stability is unacceptable and all other measures of engine performance suffer as a result. The addition of H_2 at an EGR fraction of 19% results in a noticeable initial decrease in ISNO emissions which is due solely to an increase in IMEP as illustrated previously in Figure 4.19.

4.4.4.2 Carbon Monoxide

As CO emissions are considered to be equilibrated until the early stages of the expansion stroke, it is expected that further EGR dilution will only extend the decreasing trend originally established in Figure 4.17. However, additional EGR dilution has been shown to result in further decreases in both IMEP (Figure 4.19) and exhaust gas temperature (Figure 4.25), thus increasing indicated emissions and decreasing levels of post combustion oxidation. The effect of H_2 addition on ISCO emissions is shown in Figure 4.27. The initial decrease in CO emissions at 15% EGR can be attributed to both an increase in IMEP and a displacement of hydrocarbon fuel through the addition of H_2. From 15% EGR to 30% EGR, CO emissions stay relatively constant, likely due to competition between decreasing levels of post combustion oxidation, IMEP and hydrocarbon fuel. Beyond 30% EGR, ISCO emissions rise sharply, presumably as a result of a significant reduction in IMEP (due to slow burn and misfire engine cycle) and a further reduction in levels of post combustion oxidation.

4.4.4.3 Total Hydrocarbons

As was discussed in Section 4.2.4.3, THC emissions are determined by two factors (disregarding slow burn or misfire engine cycles): first, the mass of unburned mixture compressed into crevice volumes; and second, the amount of post combustion oxidation that occurs during the expansion and exhaust strokes. The effect of H_2 addition on ISTHC emissions is shown in Figure 4.28.

Similar to CO, THC emissions initially decrease at 15% EGR, again due to an increase in IMEP and the displacement of hydrocarbon fuel. THC emissions remain relatively constant between 15% and 30% EGR, where decreasing levels of post combustion oxidation, IMEP and the fraction of hydrocarbon fuel are in competition. However, unlike CO, beyond 30% EGR there is a slight *decrease* in THC emissions, as compared to the sharp increase

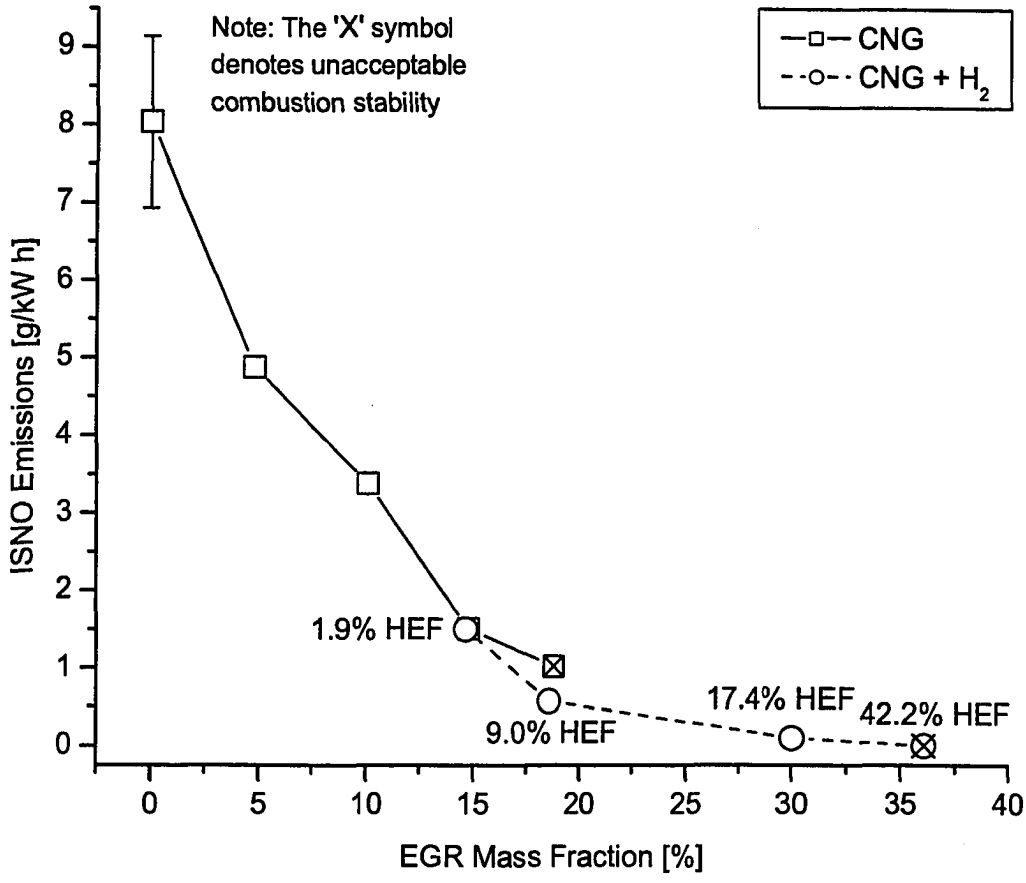

Figure 4.26: The effect of H_2 addition on exhaust diluted ISNO emissions. The amount of H_2 employed at each point is listed as a H_2 energy fraction (HEF). The error bar represents a 95% confidence interval for an undiluted base condition. The symbols containing an 'X' indicate that the COV IMEP has exceeded the upper error bound of the undiluted base condition (6.54%) and the combustion stability is thus considered unacceptable.

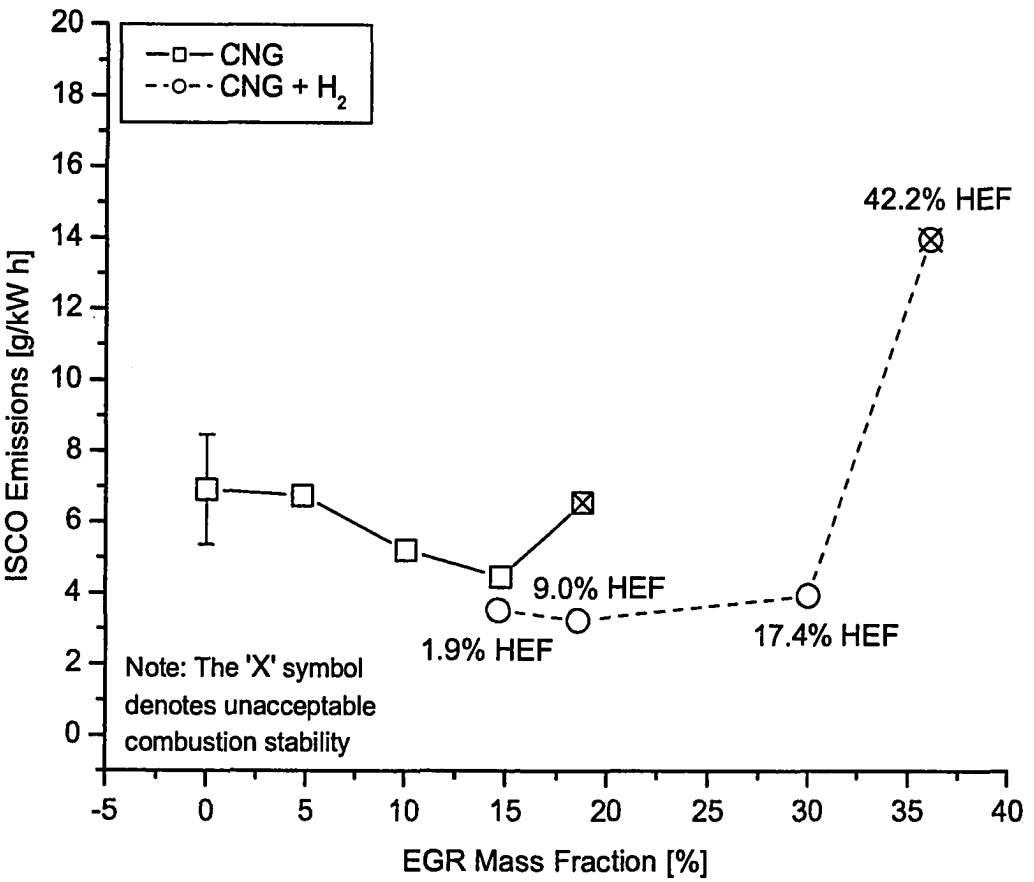

Figure 4.27: The effect of H_2 addition on exhaust diluted ISCO emissions. The amount of H_2 employed at each point is listed as a H_2 energy fraction (HEF). The error bar represents a 95% confidence interval for an undiluted base condition. The symbols containing an 'X' indicates that the COV IMEP has exceeded the upper error bound of the undiluted base condition (6.54%) and the combustion stability is thus considered unacceptable.

of CO seen in Figure 4.27.

This trend can be explained through the observation that at 36% EGR, a 42% HEF is required to maintain combustion stability. In terms of volume, a 42% HEF results in an approximate H_2 volume fraction of 69%, thus resulting in a large fraction of hydrocarbon fuel being displaced by the addition of H_2. This displacement is believed to be causing the observed trend in ISTHC emissions. While H_2 exhaust emissions were not observed, the presence of slow burn and partial burn cycles at a 36% EGR fraction would likely result in the presence of unburned H_2, further explaining the trend in THC emissions.

4.4.4.4 Carbon Dioxide

The inclusion of a section on CO_2 is a testament to the importance of greenhouse gas emissions. The effect of both H_2 addition and EGR on $ISCO_2$ emissions is shown in Figure 4.29. As expected, $ISCO_2$ emissions are essentially an inverse measure of η_{fc} when natural gas is the sole fuel, thus staying relatively constant until the onset of unstable combustion at an EGR fraction of 19%. As H_2 is added, there is a significant reduction in $ISCO_2$ emissions - 18%, from 638 g/kW h at 15% EGR to 521 g/kW h at 30% EGR while still maintaining acceptable combustion stability.

While the addition of H_2 results in a significant decrease in "usage" $ISCO_2$ emissions, as shown in Figure 4.29, there are also "upstream" CO_2 emissions which are created from the production of H_2; Figure 4.29 and the previous discussion do not take these emissions into account.

Although there are several methods of H_2 production, the steam reformation (SR) of CH_4 is one of the most popular and proven (Trimm and Önsan, 2001). The SR of CH_4 is an endothermic reaction which can be represented as:

$$CH_4 + H_2O \rightarrow 3\,H_2 + CO \qquad (\Delta H^\circ = 206 \text{ kJ/mol}) \tag{4.20}$$

Following SR, the CO is subjected to an exothermic water shift (WS) reaction in order to convert any CO to CO_2:

$$CO + H_2O \rightarrow CO_2 + H_2 \qquad (\Delta H^\circ = \text{-}41 \text{ kJ/mol}) \tag{4.21}$$

If it is presumed that the SR and WS reactions take place in an integrated facility, then any energy resulting from the exothermic WS reaction is used

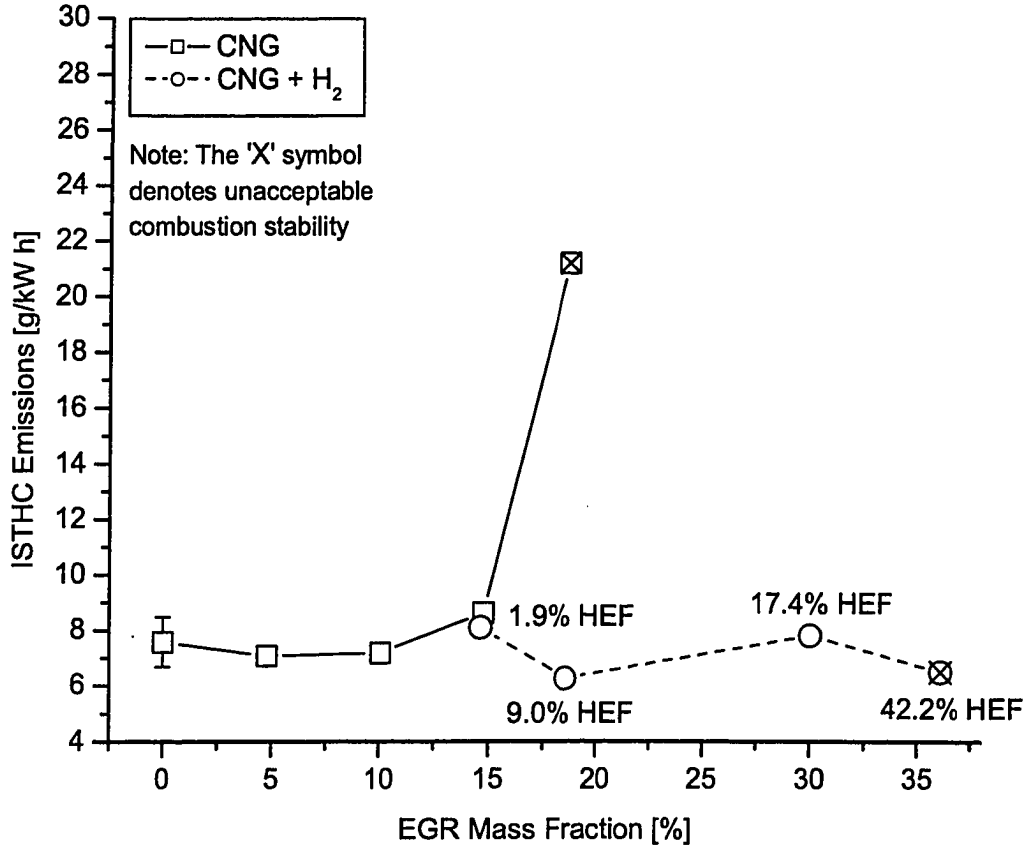

Figure 4.28: The effect of H_2 addition on exhaust diluted ISTHC emissions. The amount of H_2 employed at each point is listed as a H_2 energy fraction (HEF). The error bar represents a 95% confidence interval for an undiluted base condition. The symbols containing an 'X' indicates that the COV IMEP has exceeded the upper error bound of the undiluted base condition (6.54%) and the combustion stability is thus considered unacceptable.

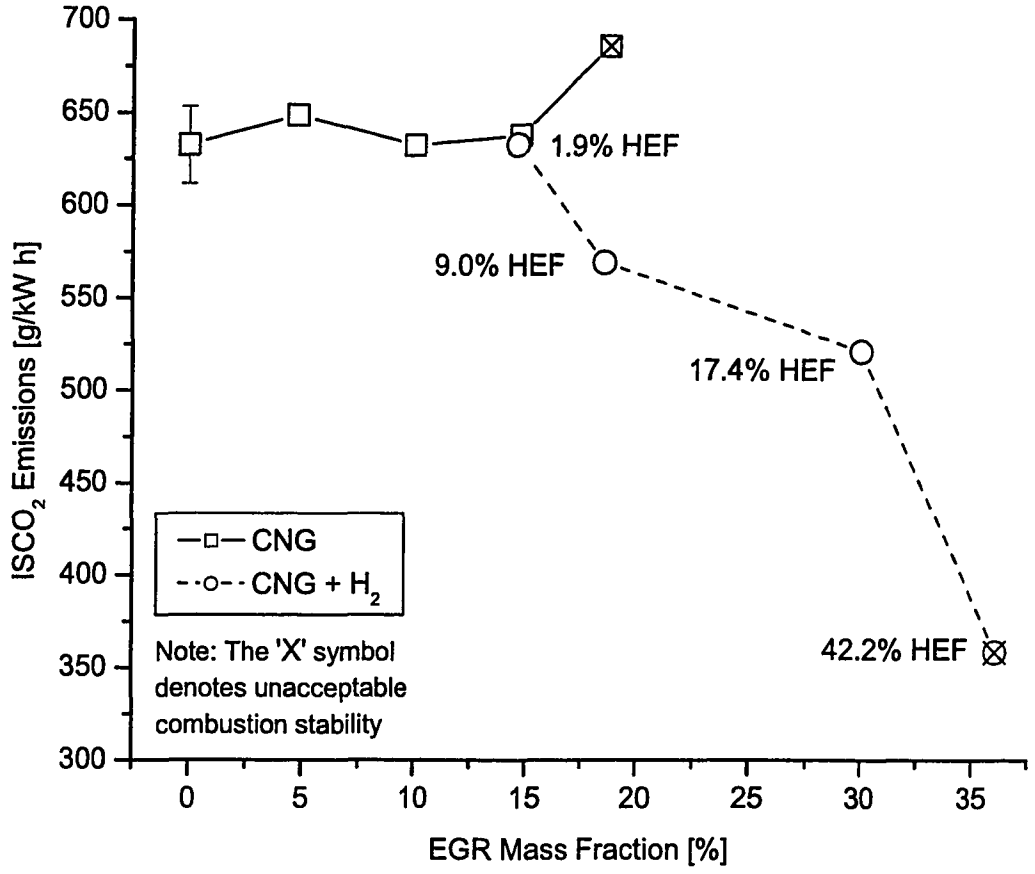

Figure 4.29: The effect of H_2 addition on exhaust diluted $ISCO_2$ emissions. The amount of H_2 employed at each point is listed as a H_2 energy fraction (HEF). The error bar represents a 95% confidence interval for an undiluted base condition. The symbols containing an 'X' indicate that the COV IMEP has exceeded the upper error bound of the undiluted base condition (6.54%) and the combustion stability is thus considered unacceptable.

to provide energy to the SR reaction. The entire process can then be viewed as:

$$SR + WS \rightarrow CO_2 + 4\,H_2 \qquad (\Delta H^\circ = 165 \text{ kJ/mol}) \tag{4.22}$$

With the energy of the WS reaction being applied to the SR process, the net result is an overall endothermic reaction. In order to provide the required energy for this process, it is assumed that stoichiometric CH_4-air is combusted and that all resulting energy is applied to the SR-WS system. The combustion of stoichiometric CH_4-air can be represented as:

$$CH_4 + 2\,(O_2 + 3.773\,N_2) \rightarrow$$
$$CO_2 + 2\,H_2O_{vap} + 7.546\,N_2 \qquad (\Delta H^\circ = \text{-}846 \text{ kJ/mol}) \tag{4.23}$$

From Equations 4.22 and 4.23 it can be determined that 0.195 moles of CH_4 must be combusted (and 0.195 moles of CO_2 produced) in order to provide the energy required by the SR-WS system. The net result is the production of 1.195 moles of CO_2 for every 4 moles of H_2 produced. In terms of mass, and taking into account a global reaction efficiency (η_{GR}), the H_2-specific CO_2 production can be represented as:

$$\boxed{\frac{m_{CO_2}}{m_{H_2}} = \frac{1.195 \cdot M_{CO_2}}{4 \cdot M_{H_2} \cdot \eta_{GR}} = \frac{6.522}{\eta_{GR}}} \tag{4.24}$$

Thus, for every 1 gram of H_2 produced, approximately 6.5 grams of CO_2 are produced (neglecting η_{GR}). Recent estimates of m_{CO_2}/m_{H_2} for the SR of CH_4 vary from 7.178 (Edwards et al., 1999) to 8.889 (Spath and Mann, 2001), which results in a range of approximate global efficiency values:

$$\boxed{0.734 = \frac{6.522}{8.889} \leq \eta_{GR} \leq \frac{6.522}{7.178} = 0.909} \tag{4.25}$$

An average η_{GR} value of 0.822 results in a m_{CO_2}/m_{H_2} value of 7.939. When these upstream CO_2 emissions are taken into account, the significant decrease in $ISCO_2$ emissions originally reported in Figure 4.29 is no longer valid. Figure 4.30 illustrates the importance of the upstream CO_2 emissions when considering total $ISCO_2$ emissions. Here it is shown that the addition of H_2, and subsequent extension of the EGR limit, results in a 6% *increase* in $ISCO_2$ emissions, from 638 g/kW h at 15% EGR to 679 g/kW h at 30%

EGR. These results underscore the importance of life-cycle considerations when comparing the emissions performance of alternative fuels.

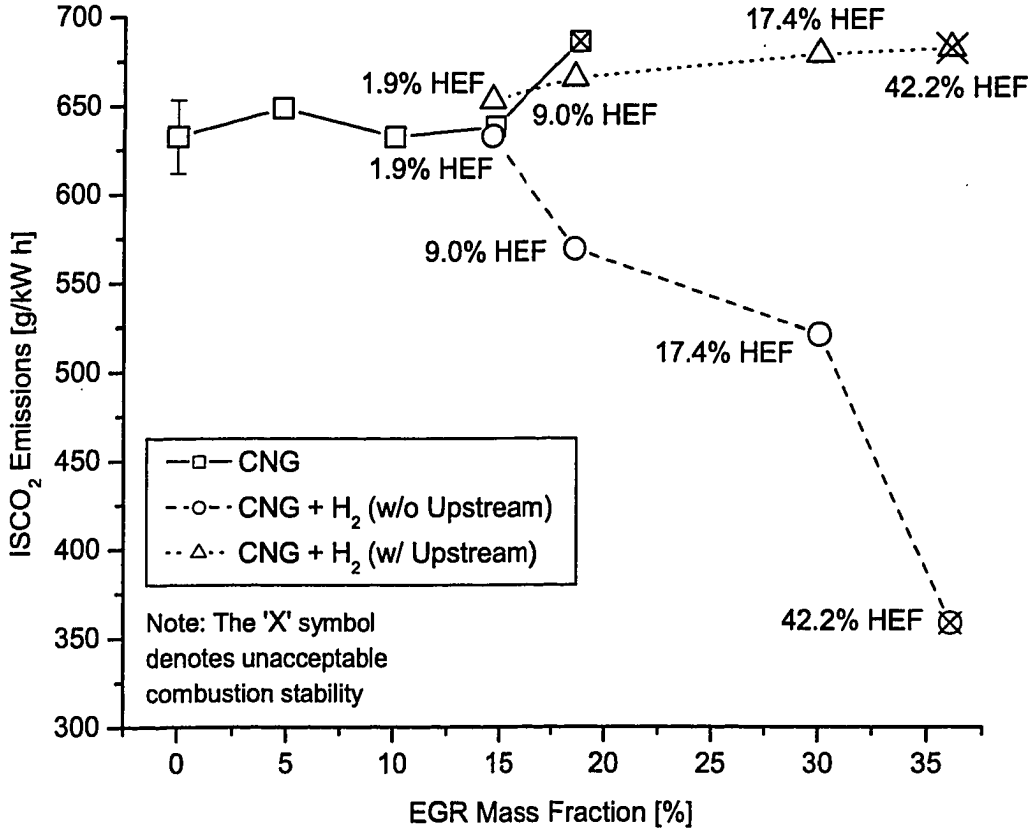

Figure 4.30: The effect of upstream CO_2 emissions on H_2 supplemented exhaust diluted $ISCO_2$ emissions. The amount of H_2 employed at each point is listed as a H_2 energy fraction (HEF). The error bar represents a 95% confidence interval for an undiluted base condition. The symbols containing an 'X' indicate that the COV IMEP has exceeded the upper error bound of the undiluted base condition (6.54%) and the combustion stability is thus considered unacceptable.

CHAPTER 5

CONCLUSIONS AND FUTURE WORK

5.1 Conclusions

The effect of H_2 addition on the exhaust diluted full-load performance of a spark ignition (SI) engine has been investigated through a series of experiments conducted on a single-cylinder research engine. Several conclusions can be drawn on the basis of the experimental results, including:

(1.) For natural gas fuelling, the maximum exhaust gas recirculation (EGR) mass fraction that could be tolerated at 1200 RPM, wide open throttle (WOT), without the covariant indicated mean effective pressure (COV IMEP) increasing beyond the upper error limit of the undiluted base condition, was 14.8%.

(2.) The addition of a 17.4% H_2 energy fraction (HEF) resulted in a maximum increase in EGR limit of 102% - from 14.8% to 30.0% EGR.

(3.) For natural gas fuelling, a 12.9% reduction in indicated mean effective pressure (IMEP), from 5.98 to 5.21 bar, was observed at the EGR dilution limit. The addition of H_2 and the subsequent extension of the EGR limit resulted in an additional 20.0% reduction in IMEP, from 5.21 to 4.17 bar.

(4.) For natural gas fuelling, a reduction in full-load indicated specific NO (ISNO) emissions of 81%, from 8.0 to 1.5 g/kW h, was achieved at the EGR limit of 14.8%. The addition of H_2 and associated extension of the EGR limit resulted in an additional 93% reduction in ISNO emissions, from 1.5 to 0.1 g/kW h. As NO emissions are typically a concern only

at high-load operation, it is promising that an 81% reduction in ISNO emissions has been achieved. at full-load, with an associated decrease in IMEP of only 12.9%. With an increase in engine displacement, it would be possible to achieve significant reductions in ISNO emissions while still maintaining the original maximum power output of the engine. The addition of H_2 and associated extension of the EGR limit resulted in additional 93% reduction in full-load ISNO emissions, with an associated 20.0% decrease in IMEP. While the engine displacement may be further increased to allow for similar maximum power outputs with additional decreases in ISNO emissions, this operating mode may also be used in place of throttling to achieve decreases in both IMEP and ISNO emissions. The added flexibility associated with H_2 addition may allow the development of an operating scheme which precludes the use of a reduction catalyst in abating NO emissions.

(5.) With natural gas fuelling, the fuel conversion efficiency (η_{fc}) remained relatively constant with EGR dilution, decreasing slightly from 31.6 to 31.4%. This deviation lies within the total uncertainty in η_{fc}. The use of H_2 again resulted in a marginal decrease in η_{fc}, from 31.4 to 30.9%, however this too was within the total uncertainty in η_{fc}. Thus, it can be stated that the η_{fc} remained essentially constant as the EGR dilution was increased, with and without H_2 addition.

(6.) While "usage" indicated specific CO_2 ($ISCO_2$) emissions remained relatively constant with EGR dilution alone (here $ISCO_2$ is essentially an inverse measure of η_{fc}), the addition of H_2 resulted in significant decreases in $ISCO_2$ emissions. A total reduction of 18.3% in usage $ISCO_2$ emissions, from 638 to 521 g/kW h, was accomplished with the use of a 17.4% H_2 energy fraction and a 30% EGR mass fraction. However, when the upstream CO_2 implications of H_2 production from the steam reformation of CH_4 are taken into account, an *increase* of 6% in total $ISCO_2$ emissions, from 638 to 679 g/kW h, was observed with the use of a 17.4% H_2 energy fraction and a 30% EGR mass fraction. These results underscore the importance of life cycle considerations when comparing the relative emissions of alternative fuels.

5.2 Future Work

Prior to performing further experiments, there are several equipment modifications that may be completed to expedite and simplify the experimental procedure.

The engine control module (ECM) is currently designed to operate in an open-loop mode, where the pulse width of both the H_2 and natural gas injectors are controlled based on input from a personal computer. To increase the ease and consistency with which the air/fuel ratio and HEF are set, the ECM should be modified to operate in a closed-loop mode. Feedback from either fuel and air mass flow rates, or exhaust oxygen level could be used to control the air/fuel ratio and the HEF. The incorporation of spark control should also be added to the ECM. Currently, spark timing is set with a common inductive timing light, making the adjustment of spark timing both tedious and time consuming.

The EGR system would also benefit from the implementation of closed loop control. Currently, the EGR mass fraction is set using two gate valves. Once the appropriate EGR mass fraction has been achieved, the position of the gate valves is left unchanged for the duration of the data acquisition. During this time, it is possible for the EGR mass fraction to drift. The measured CO_2 mole fraction within the intake plenum could be used as feedback in controlling a valve which meters the amount of EGR that reaches the intake plenum. A separate non-dispersive infrared gas analyzer should be used for this purpose which would also eliminate the need for separate "upstream" and "downstream" data acquisition.

Upon completion of the above-mentioned system modifications, experiments could be completed to determine the effect of both engine speed and load on the amount of H_2 required to extend the EGR limit. In addition to experiments with H_2 addition, simulated reformer products (e.g. 20% H_2, 25% CO and 55% N_2) could be substituted for H_2. The diluent effect of the additional N_2 and the possibility of increased CO emissions, when compared with neat H_2 addition, could be investigated.

A life cycle analysis (LCA) should be completed to compare the actual emission implications of using both H_2 and reformer gas addition. Based on various sources of H_2 production, a control scheme could be developed to minimize total "life cycle" emissions according to the method of H_2 production employed. The emissions reduction shown in this study as a result of EGR limit extension could also be investigated on a life cycle basis by

determining the corresponding reduction of precious metal loading required on a three-way catalytic converter to meet the same emissions characteristics of a traditional SI engine and three-way catalytic converter.

BIBLIOGRAPHY

S. Orhan Akansu, Zafer Dulger, Nafiz Kahraman, and T. Nejat Veziroğlu. Internal combustion engines fueled by natural gas-hydrogen mixtures. *International Journal of Hydrogen Energy*, 29:1527–1539, 2004.

S Allenby, W-C Chang, A Megaritis, and M.L. Wyszyński. Hydrogen enrichment: a way to maintain combustion stability in a natural gas fuelled engine with exhaust gas recirculation, the potential of fuel reforming. *Proceedings of the I MECH E Part D Journal of Automobile Engineering*, 215: 405–418, 2001.

Matthew Atkins. *Experimental Examination of the Effects of Fuel Octane and Diluent on HCCI Combustion.* M.Sc., University of Alberta, 2004.

Curtis Bauer. *The Effect of Hydrogen on the Performance of Methane-Fuelled S.I. Engines.* M.Sc., University of Alberta, 1999.

Wai K. Cheng, Douglas Hamrin, John B. Heywood, Simone Hochgreb, Kyoungdoug Min, and Michael Norris. An overview of hydrocarbon emissions mechanisms in spark-ignition engines. *Society of Automotive Engineers Transactions*, SAE Paper 932708, 1993.

Y.S. Cho, D.A. Santavicca, and R.M. Sonntag. The effect of spark power on spark-ignited flame kernel growth. *Society of Automotive Engineers*, SAE Paper 922168, 1992.

Enrico Conte and Konstantinos Boulouchos. Influence of hydrogen-rich-gas addition on combustion, pollutant formation and efficiency of an IC-SI engine. *Society of Automotive Engineers*, SAE Paper 2004-01-0972, 2004.

Wayne A. Daniel. Why engine variables affect exhaust hydrocarbon emission. *Society of Automotive Engineers Transactions*, SAE Paper 700108, 1970.

L.M. Das. On-board hydrogen storage systems for automotive application. *International Journal of Hydrogen Energy*, 21(9):789–800, 1996.

Wayne Edwards, Rob Dunlop, Wenli Duo, Don O'Connor, Nigel Fitzpatrick, and Sandy Constable. Alternative and future fuels and energy sources for road vehicles. Technical report, Levelton Engineering Ltd. for Transportation Issue Table National Climate Change Process, 1999.

M. Elia, M. Ulinski, and M. Metghalchi. Laminar burning velocity of methane-air-diluent mixtures. *Journal of Engineering for Gas Turbines and Power*, 123:190–196, 2001.

Jonathan W. Fox, Wai K. Cheng, and John B. Heywood. A model for predicting residual gas fraction in spark-ignition engines. *Society of Automotive Engineers Transactions*, SAE Paper 931025, 1993.

N. Gat and C.W. Kauffman. The effect of exhaust gas recirculation and turbulence on the burning velocity, dead space thickness, and minimum ignition energy in premixed methane-air combustion. *Combustion Science and Technology*, 23:1–15, 1980.

J.A. Gatowski, J.B. Heywood, and C. Deleplace. Flame photographs in a spark-ignition engine. *Combustion and Flame*, 56:71–81, 1984.

Irvin Glassman. *Combustion.* Academic Press, Inc., Orlando, second edition, 1987.

D.F. Hagen and G.W. Holiday. The effects of engine operating and design variables on exhaust emissions. *Society of Automotive Engineers Transactions*, SAE Paper 620404 (486C), 1962.

J.B. Heywood, J.M. Higgins, P.A. Watts, and R.J. Tabaczynski. Development and use of a cycle simulation to predict SI engine efficiency and NO_x emissions. *Society of Automotive Engineers*, SAE Paper 790291, 1979.

John B. Heywood. *Internal Combustion Engine Fundamentals.* McGraw-Hill Series in Mechanical Engineering. McGraw-Hill Inc., New York, 1988.

John B. Heywood and Fernando R. Vilchis. Comparison of flame development in a spark-ignition engine fueled with propane and hydrogen. *Combustion Science and Technology*, 38:313–324, 1984.

Hannu E. Jääskeläinen and James S. Wallace. Examination of charge dilution with EGR to reduce NO_x emissions from a natural gas-fuelled 16 valve DOHC four-cylinder engine. *Society of Automotive Engineers Transactions*, SAE Paper 942006, 1994.

Y. Jamal and M.L. Wyszynski. On-board generation of hydrogen-rich gaseous fuels - a review. *International Journal of Hydrogen Energy*, 19(7):557–572, 1994.

Ghazi A. Karim. Hydrogen as a spark ignition fuel. *International Journal of Hydrogen Energy*, 28:569–577, 2003.

Jan Kašpar, Paolo Fornasiero, and Neal Hickey. Automotive catalytic converters: Current status and some perspectives. *Catalysis Today*, 77:419–449, 2003.

H. Kuroda, Y. Nakajima, K. Sugihara, Y. Takagi, and S. Muranaka. The fast burn with heavy EGR, new approach for low NO_x and improved fuel economy. *Society of Automotive Engineers Transactions*, SAE Paper 780006, 1978.

David R. Lancaster, Roger B. Krieger, Spencer C. Sorenson, and William L. Hull. Effects of turbulence on spark-ignition engine combustion. *Society of Automotive Engineers Transactions*, SAE Paper 760160, 1976.

George A. Lavoie, John B. Heywood, and James C. Keck. Experimental and theoretical study of nitric oxide formation in internal combustion engines. *Combustion Science and Technology*, 1:313–326, 1970.

Grant Lumsden, David Eddleston, and Richard Sykes. Comparing lean burn and EGR. *Society of Automotive Engineers*, SAE Paper 970505, 1997.

Frederic A. Matekunas. Modes and measures of cyclic combustion variability. *Society of Automotive Engineers Transactions*, SAE Paper 830337, 1983.

Kazuma Matsui, Taro Tanaka, and Shunichi Ohigashi. Measurement of local mixture strength at spark gap of S.I. engines. *Society of Automotive Engineers Transactions*, SAE Paper 790483, 1979.

B.E. Milton and J.C. Keck. Laminar burning velocities in stoichiometric hydrogen and hydrogen-hydrocarbon gas mixtures. *Combustion and Flame*, 58:13–22, 1984.

B. Nagalingam, F. Duebel, and K. Schmillen. Performance study using natural gas, hydrogen-supplemented natural gas and hydrogen in AVL research engine. *International Journal of Hydrogen Energy*, 8(9):715–720, 1983.

Y. Nakajima, K. Sugihara, Y. Takagi, and S. Muranaka. Effects of exhaust gas recirculation on fuel consumption. *Proceedings of the Institution of Mechanical Engineers*, 195:369–377, 1981.

Nir Ozdor, Mark Dulger, and Eran Sher. Cyclic variability in spark ignition engines - a literature survey. *Society of Automotive Engineers Transactions*, SAE Paper 940987, 1994.

Ather A. Quader. Why intake charge dilution decreases nitric oxide emission from spark ignition engines. *Society of Automotive Engineers Transactions*, SAE Paper 710009, 1971.

Ather A. Quader, John E. Kirwan, and M. James Grieve. Engine performance and emissions near the dilute limit with hydrogen enrichment using an onboard reforming strategy. *Society of Automotive Engineers Transactions*, SAE Paper 2003-01-1356, 2003.

Marius J. Rauckis and William J. Mclean. The effect of hydrogen addition on ignition delays and flame propagation in spark ignition engines. *Combustion Science and Technology*, 19:207–216, 1979.

M. Shelef and R.W. McCabe. Twenty-five years after introduction of automotive catalysts: What next? *Catalysis Today*, 62:35–50, 2000.

Jack A. Smith and Gordon J.J. Bartley. Stoichiometric operation of a gas engine utilizing synthesis gas and EGR for NO_x control. *Journal of Engineering for Gas Turbines and Power*, 122:617–623, 2000.

Pamela L. Spath and Maragret K. Mann. Life cycle assessment of hydrogen production via natural gas steam reforming. Technical Report NREL/TP-570-27637, National Renewable Energy Laboratory, 2001.

R. Stone, A. Clarke, and P. Beckwith. Correlations for the laminar-burning velocity of methane/diluent/air mixtures obtained in free-fall experiments. *Combustion and Flame*, 114:546–555, 1998.

John R. Taylor. *An Introduction to Error Analysis.* University Science Books, Sausalito, California, 2nd edition, 1997.

David L. Trimm and Z. Ilsen Önsan. Onboard fuel conversion for hydrogen-fuel-cell-driven vehicles. *Catalysis Reviews*, 43:31–84, 2001.

G. Yu, C.K. Law, and C.K. Wu. Laminar flame speeds of hydrocarbon + air mixtures with hydrogen addition. *Combustion and Flame*, 63:339–347, 1986.

Appendix A

Detailed Equipment Information

Detailed information on the equipment used in this study is presented in order that all experiments be wholly reproducible. A tabular description of all equipment is given, including the manufacturer, model number, serial number and a general description of each component. Following this, an overview of the individual operating principles of the gas analyzers used for emission measurements is given.

A.1 Equipment Specifications

A tabular description of all equipment is presented in Table A.1.

Table A.1: Detailed Equipment Information

Manufacturer	Model	Serial #	Description
AFS[1]	30-02024	04-230202	Falcon natural gas regulator
AFS	400010-5	456550	Sparrow II engine control module
BEI	XH25P-SS-3600-T2-ABZC-7272-SM18	DD042564	Rotary encoder (used on crankshaft)
Bosch	N/A	N/A	Electronic natural gas fuel injector (used for natural gas and H_2)
CA[2]	300	1J09001	Non-dispersive infrared gas analyzer (CO_2 and CO)
CA	100P	8J09003	Paramagnetic gas analyzer (O_2)
CA	300-CLD	28J04007	Chemiluminescent detector (CLD) gas analyzer (NO)
CA	300M-FID	30J04002	Flame ionization detector gas analyzer (THC)
Dasibi	5008	678	Multi-gas calibrator
Digalog	1002A	821112	230 volt dynamometer controller
Dynascan	3300	93-00867	Pulse generator
Eaton	3168	2360	Dynamometer load cell
Ford	N/A	N/A	Variable reluctance crankshaft sensor (used by Sparrow II engine control module)

[1]Alternative Fuel Systems
[2]California Analytical

Table A.1: continued

Manufacturer	Model	Serial #	Description
GSE	550	25405	Electronic top loading mass balance (used for calibration of Omega FMA-A2117 natural gas flow meter)
Harris	MR501-6	N/A	Compressed gas pressure regulator
HP[3]	6038A	3221A-11427	0-60 volt, 0-10 amp, 200 watt power supply
Lucas/Schaevitz	500DC-E	7576	Linear variable differential transformer
Mettler	PE16	N/A	Electronic top loading mass balance
MTS	1104CA	36322503	Pressure transducer charge amplifier
MTS	E002-0093	36422503	Baseline combustion analysis system (CAS) processing unit
NI[4]	PCIMIO16E-1	10018C3	12-bit data acquisition card (device 1)
NI	PCIMIO16E-1	1001882	12-bit data acquisition card (device 2)
NI	PCIMIO16E-4	A4833F	12-bit data acquisition card (device 3)
NI	SCB-68	N/A	Shielded connector block (devices 1-3)
NGK	AB-6	N/A	Spark plug
Omega	FMA-A2108	6780	H_2 thermal mass flow meter (0-5 SLPM)
Omega	FMA-A2117	6958	H_2 thermal mass flow meter (0-50 SLPM)
Omega	FMA-A2117	6760	Natural gas thermal mass flow meter (0-50 SLPM)
Omega	HH506	53001085	Thermocouple thermometer (used to measure exhaust sample line temperature)
Omega	PCL 601	P601146810	Pressure calibrator (0-200 kPa)

[3]Hewlett Packard
[4]National Instruments

Table A.1: continued

Manufacturer	Model	Serial #	Description
Shurflo	8000-933-250	N/A	Diaphragm pump (415 kPa bypass)
TE[5]	N/A	0203311	Thermocouple temperature controller
TSI	42350101	42350402003	Intake air thermal mass flow meter
Validyne	CD15	12308	Intake pressure carrier demodulator
Validyne	CD15	56365	Exhaust pressure carrier demodulator
Validyne	DP15	63251	Intake pressure transducer
Validyne	DP15	28916	Exhaust pressure transducer
Vishay	2110	0133474	Strain gauge power supply
Vishay	2120	40479	Strain gauge signal conditioner

[5]Thermoelectric

A.2 Equipment Operating Principles

The operating principles of several instrumentation components are discussed here in detail.

A.2.1 Chemiluminescent Detector Gas Analyzer

A California Analytical model 300-CLD chemiluminescent detector (CLD) was used to measure the NO concentration of the exhaust products from the cooperative fuel research (CFR) engine. Within the CLD, any NO in the exhaust products is converted to NO_2 via an oxidative reaction with molecular ozone, which is produced on-board the gas analyzer using bottled air. It is typical for a portion of these NO_2 molecules to become electronically excited, after which they return to their original state, causing the emission of photons. A photodiode detector converts this photon emission into a low-level DC voltage, which is proportional to the NO concentration of the gas. This voltage is amplified and is available as a voltage output from the instrument.

A.2.2 FID Gas Analyzer

A California Analytical model 300M-FID flame ionization detector (FID) was used to measure the total hydrocarbon (THC) concentration of the exhaust products from the CFR engine. The FID utilizes a carbon-free flame, supplied in this case by a 40%-60% H_2-He gas mixture, through which the gas sample is passed. Any carbon atoms within the sample are ionized, thus causing the production of both electrons and positive ions. These ions are collected by a 250 volt polarized electrode ring and a low-level current is produced, which is proportional to the carbon content of the sample. This current is amplified and converted to a DC voltage by the main electrometer amplifier board and is available as a voltage output from the instrument.

A.2.3 NDIR Gas Analyzer

A California Analytical model 300 non-dispersive infrared (NDIR) gas analyzer was used to measure both the CO and CO_2 within the intake plenum and exhaust system of the CFR engine. Within the infrared gas analyzer, an infrared beam is passed through a "chopper" which essentially divides the

continuous infrared beam into a series of finite length segments. These segments are passed through a chamber of known length which contains the gas sample to be analyzed. The presence of the gas component of interest results in an attenuation of the infrared light source, which is subsequently directed into the front chamber of a two-chamber micro-flow sensor. The micro-flow sensor is filled with the gas component of interest, and the infrared light is further attenuated upon passing through both the front and rear chambers of the sensor. This energy absorption results in a differential pressure between the front and rear chambers of the micro-flow sensor, thus causing a gas flow that is proportional to the concentration of the gas component of interest. The output signal is a low-level AC voltage and is amplified and rectified after which it is available as a voltage output from the instrument.

A.2.4 Paramagnetic Gas Analyzer

A California Analytical model 100P paramagnetic gas analyzer was used to measure the O_2 content from the exhaust stream of the CFR engine. The paramagnetic analyzer relies on the paramagnetic properties of O_2 when compared to other gases. Within the analyzer, two quartz spheres are filled with (diamagnetic) N_2 and this dumbbell is suspended within a symmetrical magnetic field. As the sample gas is passed around this dumbbell, the presence of any O_2 results in an altered magnetic field, thus causing the dumbbell to rotate. This rotation is detected by an optical circuit and a countering torque is applied to the dumbbell via a platinum wire which is wrapped around the center of the dumbbell. The amount of current required to restore the original dumbbell position is proportional to the O_2 content of the gas sample. The temperature dependency of the paramagnetic susceptibility of O_2 is compensated for within the feedback circuit.

APPENDIX B

CALIBRATION AND ERROR ANALYSIS

To ensure reliable results, all instrumentation was carefully calibrated before any experiments were performed. An overview of the techniques and equipment used in the calibration of various components is presented here, along with representative calibration plots.

While it is important to ensure that all instrumentation is carefully calibrated, it is also prudent to calculate the uncertainty of individual measurements resulting from the finite accuracy of both calibration procedures and individual instruments. Wherever possible, a differential error analysis has been performed to determine the uncertainty associated with a particular calibration method. The larger of either maximum calibration or instrument uncertainty is then used to represent the error in a given measurement. The maximum instrument uncertainty typically corresponds to calibrated values which are very small when compared to the measurement range of the instrument, resulting in large values of maximum instrument uncertainty reported for several instruments. Note that the instruments are rarely (if ever) used for measurements of this magnitude and the maximum instrument uncertainty is much lower for the range in which they are typically used.

Prior to a detailed description of calibration procedures and differential error analysis, a tabular overview of all instrumentation, including maximum instrument and calibration uncertainties is first presented. The interested reader can find further details in the subsequent sections.

B.1 Overview of Measurement Error

A tabular description of the uncertainty associated with instrumentation and calibration procedures is presented in Table B.1. The larger of either

maximum instrument or calibration uncertainty is presented in underline as the governing amount of measurement error.

Table B.1: Instrument and Calibration Uncertainty

Description	Maximum Calibration Uncertainty[1]	Maximum Instrument Uncertainty[2]
TSI model 4235 air thermal mass flow meter	1.0%	2.5%
Omega model FMA-A2117 H_2 thermal mass flow meter	0.6%	5.8%
Omega model FMA-A2117 natural gas thermal mass flow meter	1.8%	5.6%
Validyne model DP15 intake pressure transducer	0.4%	1.3%
Validyne model DP15 exhaust pressure transducer	0.8%	1.3%
Eaton model 3168 dynamometer load cell	0.05%	2.2%[3]
California Analytical CLD gas analyzer	3.2%	9.7%
California Analytical FID gas analyzer	2.9%	17.9%
California Analytical NDIR gas analyzer (CO_2)	2.8%	11.1%
California Analytical NDIR gas analyzer (CO)	2.8%	9.2%
California Analytical paramagnetic gas analyzer	2.8%	10.7%

[1]Maximum percentage uncertainty of a given measurement based on total calibration uncertainty

[2]Maximum percentage uncertainty of a given measurement due to instrument uncertainty, typically occurring at the lowest calibrated value - note that the instrument is typically not operated in this region

[3]Based on a summation of worst case specified hysteresis and non-linearity

B.2 Differential Error Analysis Overview

Given a function, $f = f(x, \ldots, y)$, the error in f can be calculated as the error which is propagated through independent and random uncertainties in each of $x, \ldots, y$ as:

$$\delta f = \sqrt{\left(\frac{\partial f}{\partial x}\delta x\right)^2 + \cdots + \left(\frac{\partial f}{\partial z}\delta z\right)^2} \tag{B.1}$$

where δ represents the uncertainty in a given variable (Taylor, 1997).

B.3 Mass Flow Meters

Each of air, H_2 and natural gas were measured with thermal mass flow meters in this study. Each flow meter required a unique method of calibration due to differences in the physical properties of the measured gases.

B.3.1 Air Mass Flow Meter

The TSI model 4235 mass flow meter was calibrated by measuring the time it took for a known volume of air to pass through the flow meter. The volume of air was measured using a recently calibrated 140 litre (5 ft^3) bell prover which was accurate to within 0.5%. As all testing took place at ambient conditions with negligible pressure increase across the flow meter, the air density was calculated for ambient temperature and atmospheric pressure. The voltage output of the mass flow meter was monitored using an averaging volt meter. Upon completion of a test, the average voltage over the duration of the test was recorded. The time of each test was measured by hand with a NIST traceable stopwatch.

The mass flow rate of air can be calculated as:

$$\dot{m}_{air} = \frac{V_{air}\, P_{air}}{t\, R_{air}\, T_{air}} \tag{B.2}$$

where: V_{air} = Volume of air as measured with bell prover
P_{air} = Atmospheric pressure
t = Elapsed time
R_{air} = Gas constant for air
T_{air} = Ambient temperature

To determine the uncertainty in the mass flow rate of air, Equation B.2 is differentiated according to Equation B.1. If it is assumed that the error in the gas constant of air is negligible, the uncertainty in the mass flow rate of air is calculated as:

$$\delta \dot{m}_{air} = \left[\left(\frac{P_{air}\, \delta V}{t\, R_{air}\, T_{air}} \right)^2 + \left(\frac{V_{air}\, \delta P}{t\, R_{air}\, T_{air}} \right)^2 + \left(\frac{-P_{air}\, V_{air}\, \delta t}{t^2\, R_{air}\, T_{air}} \right)^2 + \left(\frac{-P_{air}\, V_{air}\, \delta T}{t\, R_{air}\, T_{air}^2} \right)^2 \right]^{0.5} \quad \text{(B.3)}$$

Since the elapsed time is the only variable that changes as the flow rate is varied, a worst-case uncertainty exists at the highest flow rate where the fractional uncertainty in time is highest. At this condition, the variables and respective uncertainties are:

$$\begin{aligned} V_{air} &= 0.1133 \pm 0.0006 \text{ m}^3 \\ P_{air} &= 92.1 \pm 0.1 \text{ kPa} \\ t &= 12.3 \pm 0.1 \text{ s} \\ R_{air} &= 0.287 \pm 0 \text{ kJ/kg K} \\ T_{air} &= 293 \pm 1 \text{ K} \end{aligned}$$

which results in an air mass flow rate of:

$$\boxed{\dot{m}_{air} = 10.3 \pm 0.1 \text{ g/s}}$$

A representative calibration plot of the TSI model 4235 mass flow meter is included in Figure B.1.

B.3.2 H_2 Mass Flow Meter

The H_2 thermal mass flow meter was calibrated using the same procedure that was followed for the air mass flow meter, as outlined in Section B.3.1, except that the working gas was switched from air to N_2. It is typical to calibrate a thermal mass flow meter with an inert gas (such as N_2) and then apply a correction factor which accounts for differences in gas density and specific heat between calibration and working gases. In the case of H_2, no

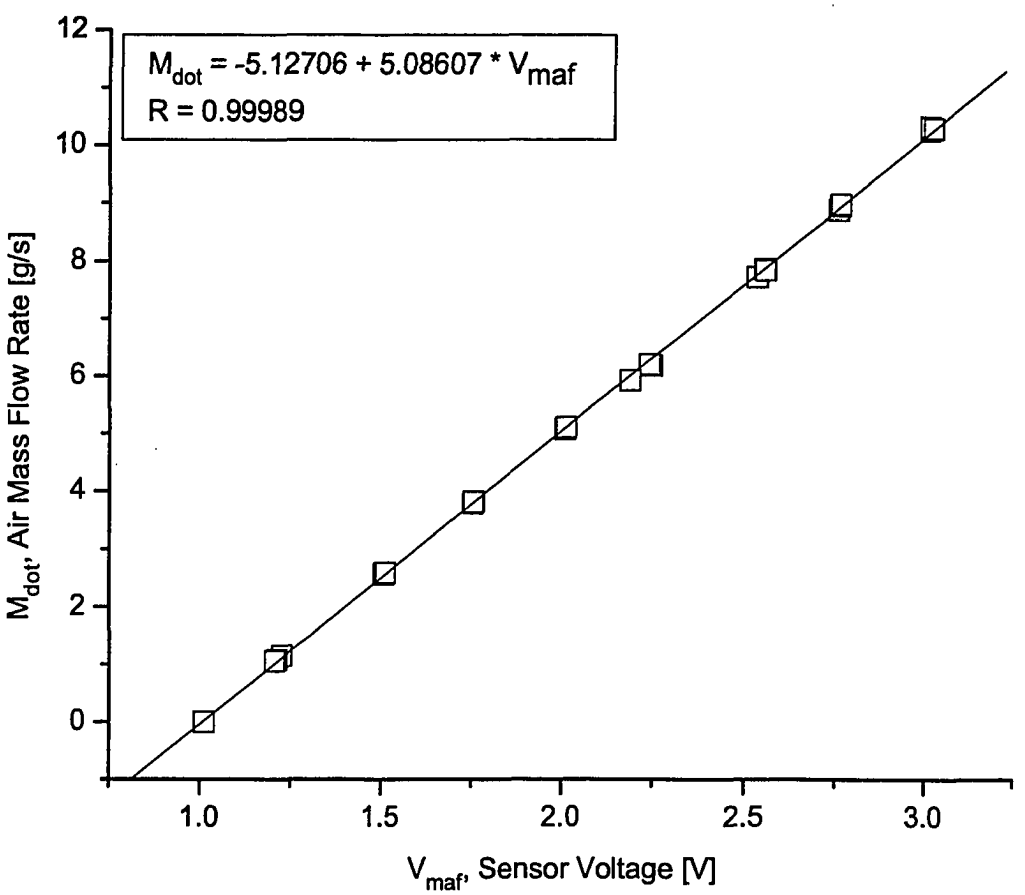

Figure B.1: Calibration of TSI model 4235 air mass flow meter.

correction factor is needed when a calibration has been performed with N_2 as the product of density and specific heat between the two gases is within one percent.

Thus, a worst case uncertainty in H_2 mass flow rate is again taken at the highest mass flow rate where the fractional uncertainty in time is highest. At this condition, the variables and respective uncertainties are:

$$\begin{aligned} V_{N_2} &= 0.1133 \pm 0.0006 \text{ m}^3 \\ P_{N_2} &= 93.2 \pm 0.1 \text{ kPa} \\ t &= 122.2 \pm 0.1 \text{ s} \\ R_{N_2} &= 0.2968 \pm 0 \text{ kJ/kgK} \\ T_{N_2} &= 292 \pm 1 \text{ K} \end{aligned}$$

which results in a N_2 mass flow rate of:

$$\dot{m}_{N_2} = 0.997 \pm 0.006 \text{ g/s}$$

The mass flow rate of H_2 can then be calculated as:

$$\boxed{\dot{m}_{H_2} = \dot{m}_{N_2} \frac{R_{N_2}}{R_{H_2}} = 71.8 \pm 0.2 \text{ mg/s}}$$

A representative calibration plot of the Omega model FMA-A2117 H_2 mass flow meter is included in Figure B.2.

B.3.3 Natural Gas Mass Flow Meter

As the specific heat of the domestic natural gas supply was not readily available, the calibration method used for the air and H_2 mass flow meters was not applicable in calibrating the natural gas mass flow meter. Instead, the natural gas mass flow meter was calibrated by measuring the reduction in mass that occurred over a given time when natural gas was vented out of a pressurized cylinder. The mass was measured using a model GSE 550 electronic top loading mass balance which was interfaced to a Labview data acquisition system.

Using this system, the mass flow rate of natural gas can be calculated as:

$$\dot{m}_{CNG} = \frac{m_{start} - m_{end}}{t} \tag{B.4}$$

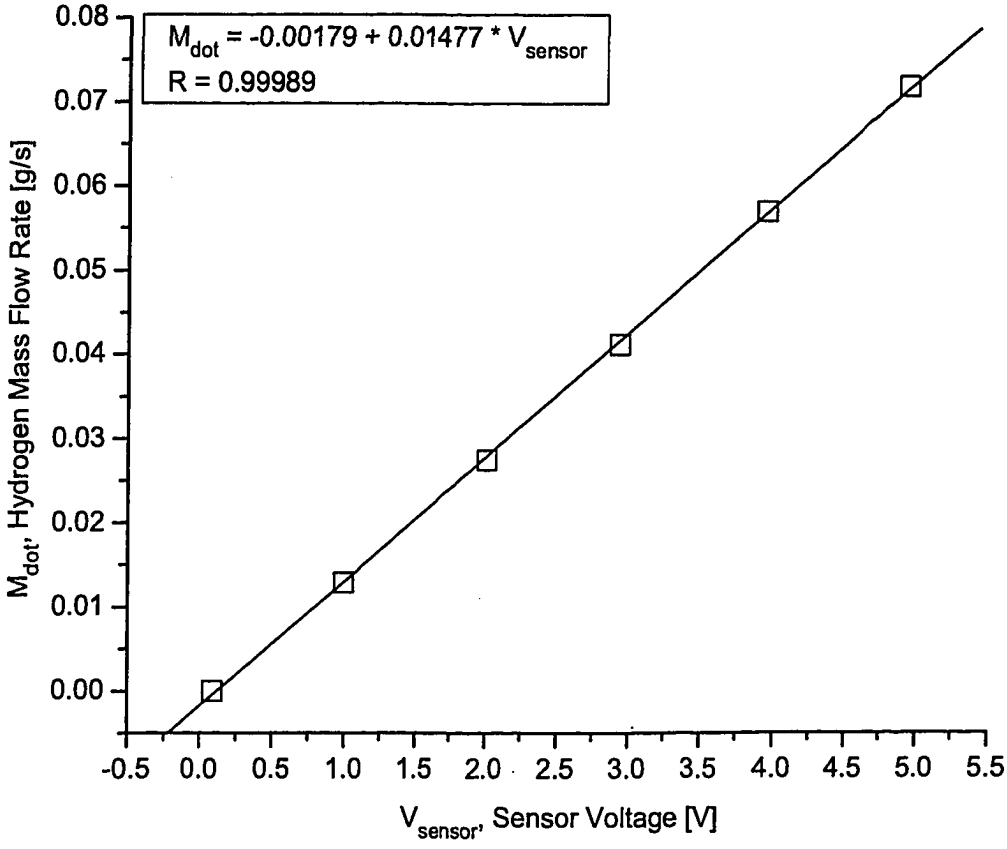

Figure B.2: Calibration of Omega model FMA-A2117 H_2 mass flow meter.

where: m_{start} = Cylinder mass at beginning of calibration
m_{end} = Cylinder mass at end of calibration
t = Elapsed time

Differentiating Equation B.4 according to Equation B.1, the uncertainty in natural gas mass flow rate can be calculated as:

$$\delta\dot{m} = \left\{ \left[\frac{\delta m_{start}}{t}\right]^2 + \left[\frac{-\delta m_{end}}{t}\right]^2 + \left[\frac{(m_{end} - m_{start})\,\delta t}{t^2}\right]^2 \right\}^{0.5} \quad \text{(B.5)}$$

Again, a worst case uncertainty occurs at the highest flow rate, as the fractional uncertainty in time is highest. At this condition, the variables and respective uncertainties are:

m_{start} = 29049 ± 1 g
m_{end} = 28972 ± 1 g
t = 156.0 ± 0.1 s

which results in a natural gas mass flow rate of:

$$\boxed{\dot{m}_{CNG} = 504 \pm 9 \text{ mg/s}}$$

A representative calibration plot of the Omega model FMA-A2117 natural gas mass flow meter is included in Figure B.3.

B.4 Pressure Transducers

Validyne differential pressure transducers were used to measure the intake and exhaust pressures in this study. To calibrate the differential pressure transducers, an Omega PCL 601 (0-200 kPa) pressure calibrator was used. The pressure calibrator was accurate to within 0.1 kPa, over a temperature range of 0 to 40 °C. As the calibration error is a fixed value of 0.1 kPa, and is only a function of the calibration device, the worst case uncertainty occurs at the lowest calibrated pressure.

The worst case uncertainty for both the intake and exhaust pressure transducers can then be calculated as:

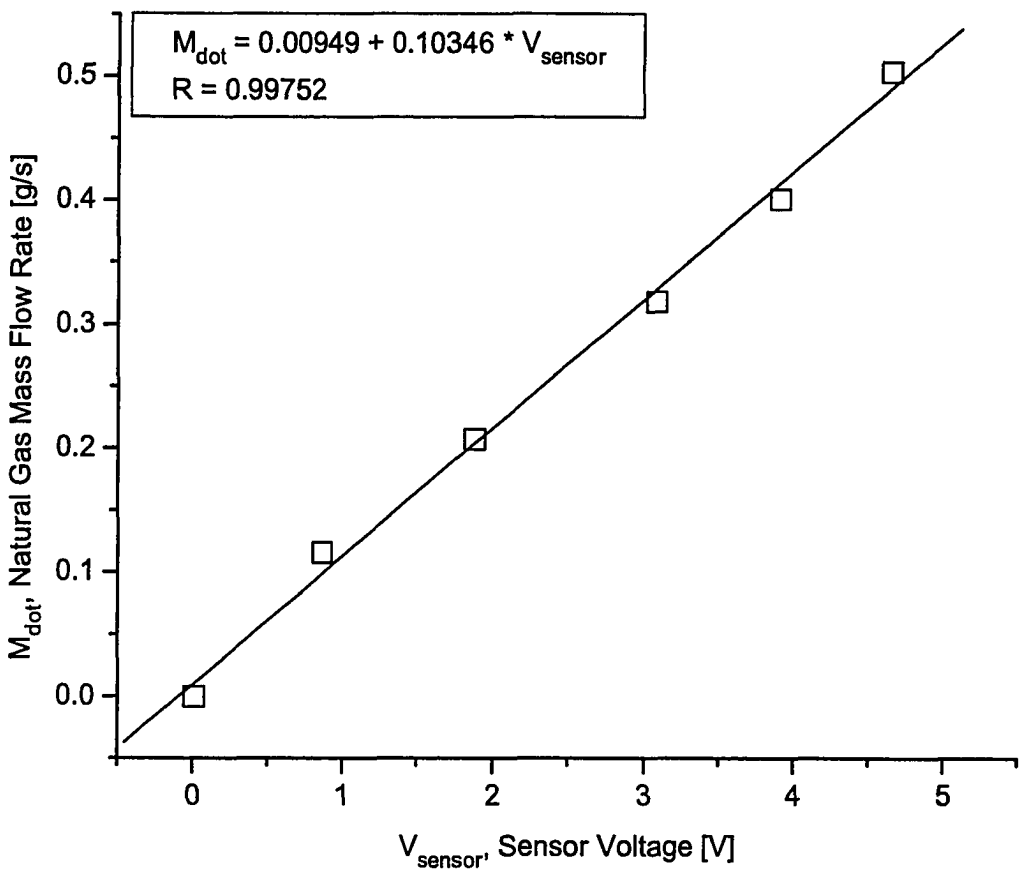

Figure B.3: Calibration of Omega model FMA-A2117 natural gas mass flow meter.

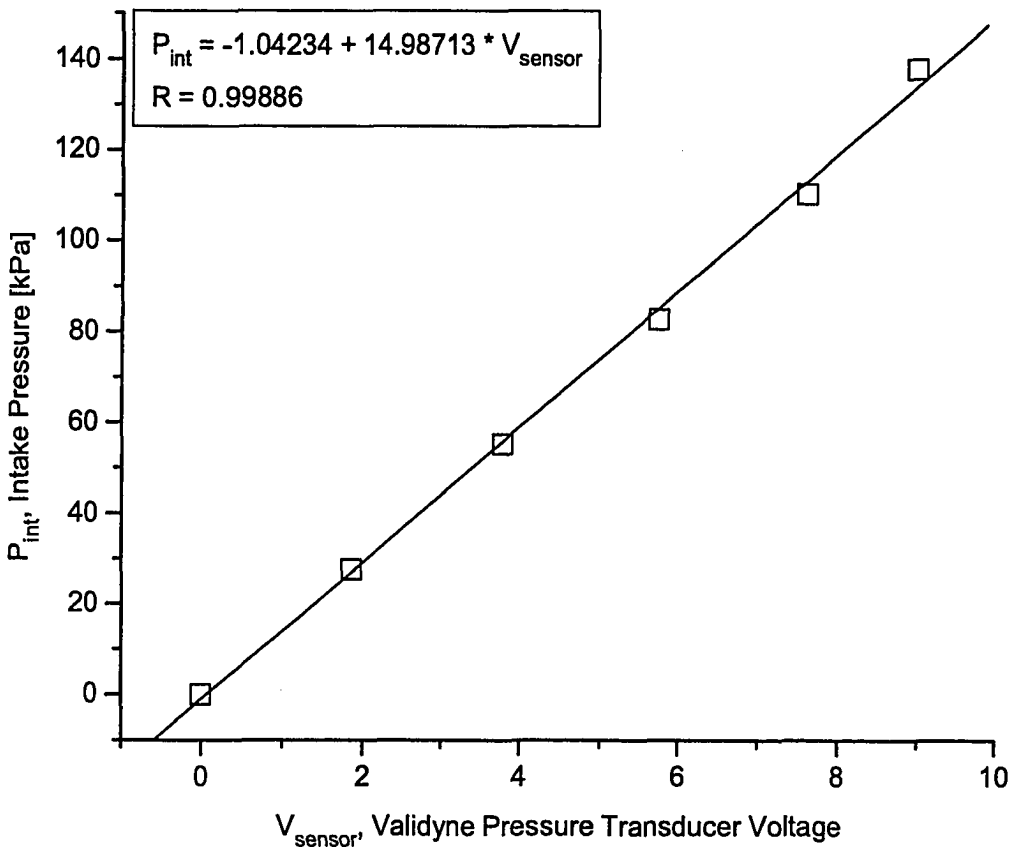

Figure B.4: Calibration of Validyne model DP15 intake pressure transducer.

$$\boxed{P_{intake} = 27.6 \pm 0.1 \text{ kPa}} \tag{B.6}$$

$$\boxed{P_{exhaust} = 13.8 \pm 0.1 \text{ kPa}} \tag{B.7}$$

Representative calibration plots for both intake and exhaust pressure transducers are shown in Figures B.4 and B.5 respectively.

B.5 Dynamometer Load Cell

To measure brake torque, a load cell was mounted at a distance from the centerline of the eddy current dynamometer used to absorb engine power.

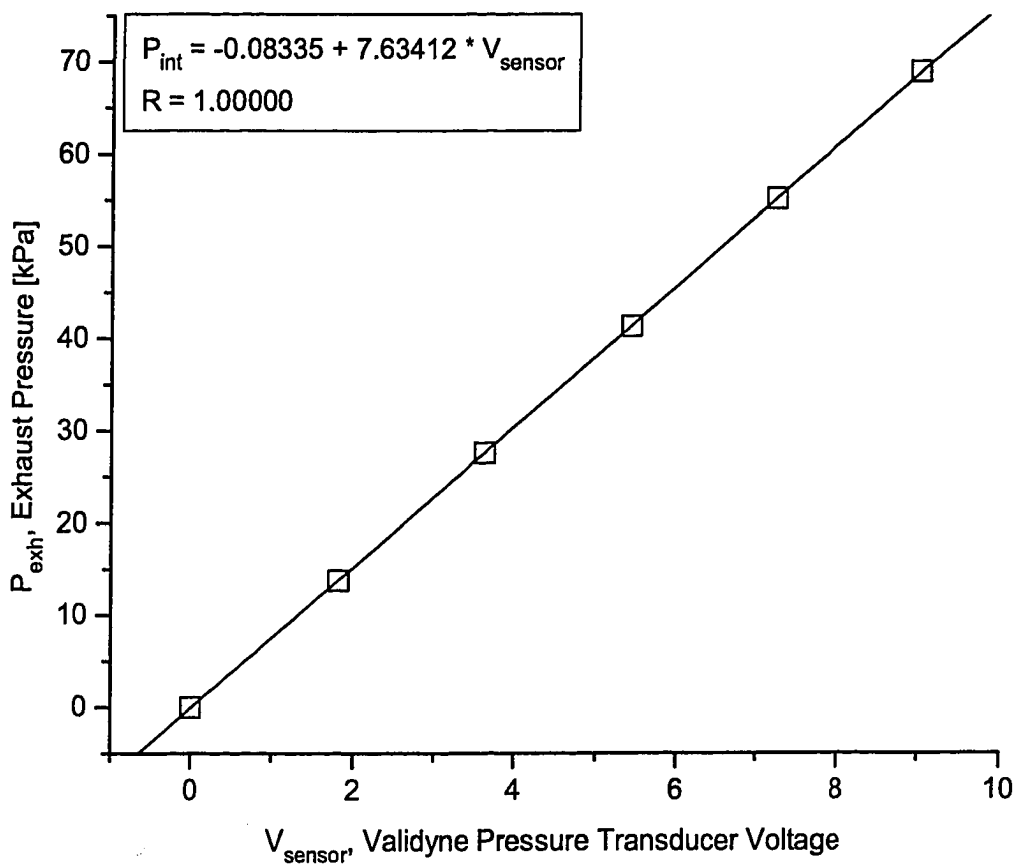

Figure B.5: Calibration of Validyne model DP15 exhaust pressure transducer.

The force measured by the load cell was directly proportional to the brake torque of the engine.

The load cell was calibrated by connecting a platform of known mass to the top of the load cell, on to which various masses were placed. The low-level output of the load cell was connected to a Vishay model 2120 load cell signal conditioner and was measured using a Labview data acquisition system. The load cell force can be calculated as:

$$F_{LC} = m_{total} \cdot g \tag{B.8}$$

where: m_{total} = Total mass on load cell
g = Gravitational constant

Prior to calibration, the mass of each calibration weight was determined using a Mettler PE-16 electronic top loading mass balance to an accuracy of 0.2 grams. Assuming that there is no uncertainty in the gravitational constant, the uncertainty in the load cell force can be calculated as:

$$\delta F_{LC} = g \cdot \delta m_{total} \tag{B.9}$$

As the uncertainty in measured mass is constant, a worst case uncertainty in load cell force occurs at the minimum calibrated mass. At this condition, the variables and respective uncertainties are:

$m_{total} = 420.6 \pm 0.2$ g
$g = 9.81 \pm 0$ m/s^2

The worst case uncertainty in load cell force is then calculated as:

$$\boxed{F_{LC} = 4.126 \pm 0.002 \text{ N}} \tag{B.10}$$

A calibration plot of the dynamometer load cell is given in Figure B.6.

The uncertainty in brake torque measurements was further compounded by an uncertainty in measuring the distance between dynamometer centerline and load cell measurement axis. Brake torque is calculated as:

$$T_{brake} = F_{LC} \cdot d \tag{B.11}$$

where: d = Measured distance between dynamometer and load cell

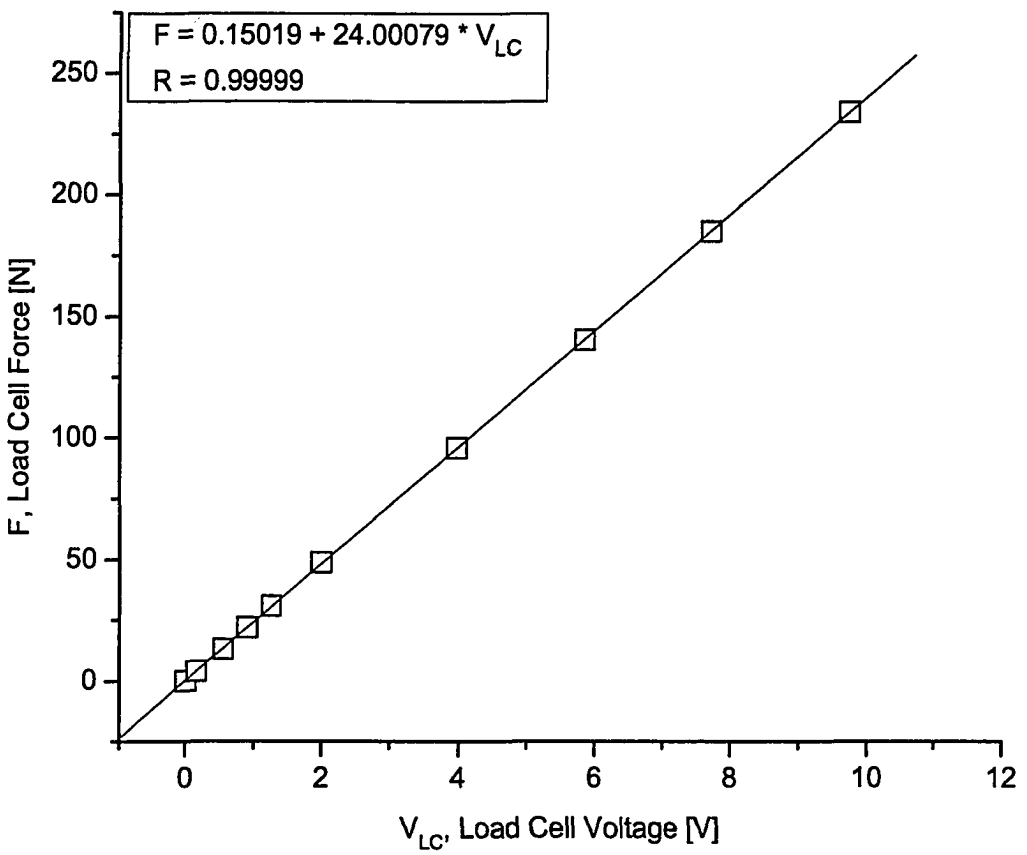

Figure B.6: Calibration of Eaton model 3168 dynamometer load cell.

The uncertainty in brake torque can then be calculated as:

$$\delta T_{brake} = \left[(d \cdot \delta F_{LC})^2 + (F_{LC} \cdot \delta d)^2\right]^{0.5} \tag{B.12}$$

As the uncertainty in d is a constant, the worst case uncertainty in brake torque occurs at the minimum calibrated load cell force. At this condition, the variables and respective uncertainties are:

$$F_{LC} = 4.126 \pm 0.002 \text{ N}$$
$$d = 29 \pm 1 \text{ cm}$$

The worst case uncertainty in brake torque is then calculated as:

$$\boxed{T_{brake} = 1.20 \pm 0.04 \text{ N m}} \tag{B.13}$$

B.6 Gas Analyzers

The calibration of the emission analyzers was performed using Praxair Certified Standard bottled gases and a Dasibi model 5008 multi-gas calibrator. The analytical accuracy of the bottled gases was ±2% of the stated concentration, while the accuracy of the multi-gas calibrator was 0.25% of the full scale flow measurement of 10 LPM. Prior to calibration, each gas analyzer was allowed a minimum of one hour to reach a steady operating condition. Careful attention was paid to achieving the appropriate sample inlet pressure and flow rate, as specified in the instruction manual of each analyzer.

B.6.1 Chemiluminescent Detector Gas Analyzer

The chemiluminescent detector (CLD) was used to measure the NO concentration of the exhaust gas sample. To obtain the appropriate calibration gas, it was necessary to use Praxair Certified Primary Standard bottled gas which had an analytical uncertainty of ±1% of the stated composition of 4021 ppm NO. The CLD analyzer was calibrated over an operating range of 0-3000 ppm. To calibrate the CLD analyzer over a number of NO concentrations, measured amounts of N_2 were mixed with the calibration gas using a multi-gas calibrator. The NO concentration in a given mixture of calibration gas and N_2 can be calculated as:

$$y_{NO} = \frac{y_{NO,bot} Q_{NO,bot}}{Q_{NO,bot} + Q_{N_2,bot}} \tag{B.14}$$

where: $y_{NO,bot}$ = Molar concentration of NO in calibration gas
$Q_{NO,bot}$= Volume flow rate of calibration gas
$Q_{N_2,bot}$ = Volume flow rate of N_2 dilution gas

Differentiating Equation B.14 according to B.1 results in an expression for the uncertainty in measured NO concentration:

$$\delta y_{NO} = \left\{ \left[\frac{Q_{NO,bot} \cdot \delta y_{NO,bot}}{Q_{NO,bot} + Q_{N_2,bot}} \right]^2 + \left[\frac{y_{NO,bot} \cdot \delta Q_{NO,bot}}{Q_{NO,bot} + Q_{N_2,bot}} - \frac{y_{NO,bot} \cdot Q_{NO,bot} \cdot \delta Q_{NO,bot}}{(Q_{NO,bot} + Q_{N_2,bot})^2} \right]^2 + \left[\frac{y_{NO,bot} \cdot Q_{NO,bot} \cdot \delta Q_{N_2,bot}}{-(Q_{NO,bot} + Q_{N_2,bot})^2} \right]^2 \right\}^{0.5} \tag{B.15}$$

As the uncertainty of the NO concentration in the bottle gas is constant, a worst case uncertainty in measured NO concentration occurs at the lowest calibrated concentration. At this condition, the variables and respective uncertainties are:

$y_{NO,bot} = 4021 \pm 40$ ppm
$Q_{NO,bot} = 0.78 \pm 0.03$ LPM
$Q_{N_2,bot} = 9.22 \pm 0.03$ LPM

The worst case uncertainty in measured NO concentration is then calculated as:

$$\boxed{y_{NO} = 310 \pm 10 \text{ ppm}} \tag{B.16}$$

A representative calibration plot for the California Analytical CLD gas analyzer is given in Figure B.7.

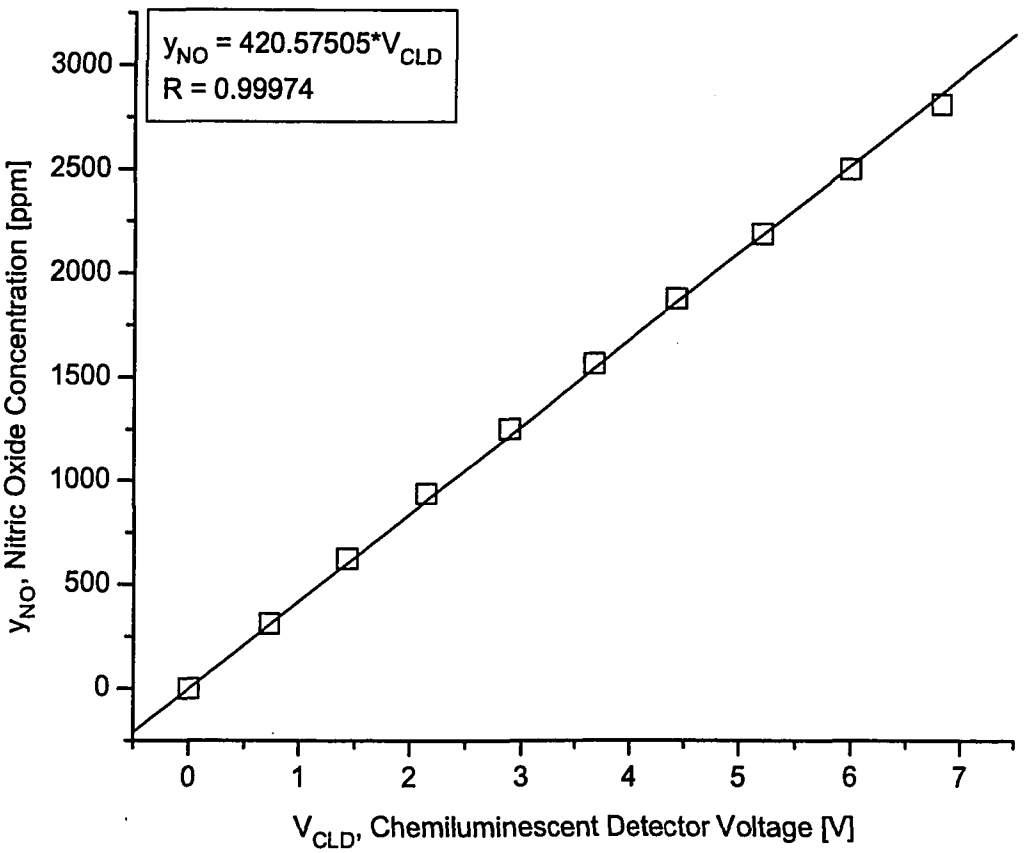

Figure B.7: Calibration of California Analytical model 300-CLD CLD gas analyzer.

B.6.2 FID Gas Analyzer

A California Analytical model 300M-FID flame ionization detector (FID) was used to measure the total hydrocarbon (THC) concentration of the exhaust gas sample. The FID was allowed to warm up for one hour after the internal burner had been ignited. To calibrate the FID, a CH_4-N_2 blend was supplied to the FID from two gas cylinders: a Praxair Certified Standard gas cylinder with a CH_4 concentration of 5030 ppm; and a separate cylinder of N_2. CH_4 and N_2 were blended using a multi-gas calibrator. The FID was calibrated using an operating range of 0-10000 ppm, although the maximum CH_4 concentration used for the calibration was 5030 ppm. For a given blend of CH_4 and N_2, the CH_4 concentration can be calculated as:

$$y_{THC} = \frac{y_{THC,bot}\, Q_{THC,bot}}{Q_{THC,bot} + Q_{N_2,bot}} \tag{B.17}$$

where: $y_{THC,bot}$ = Molar concentration of CH_4 in calibration gas
$Q_{THC,bot}$= Volume flow rate of calibration gas
$Q_{N_2,bot}$ = Volume flow rate of N_2 dilution gas

Equation B.17 can be differentiated according to Equation B.1 to solve for the uncertainty in measured THC concentration as:

$$\delta y_{THC} = \left\{ \left[\frac{Q_{THC,bot} \cdot \delta y_{THC,bot}}{Q_{THC,bot} + Q_{N_2,bot}} \right]^2 + \left[\frac{y_{THC,bot} \cdot \delta Q_{THC,bot}}{Q_{THC,bot} + Q_{N_2,bot}} - \frac{y_{THC,bot} \cdot Q_{THC,bot} \cdot \delta Q_{THC,bot}}{(Q_{THC,bot} + Q_{N_2,bot})^2} \right]^2 + \left[\frac{y_{THC,bot} \cdot Q_{THC,bot} \cdot \delta Q_{N_2,bot}}{-(Q_{THC,bot} + Q_{N_2,bot})^2} \right]^2 \right\}^{0.5} \tag{B.18}$$

As the uncertainty in the CH_4 concentration of the calibration gas is constant, a worst case uncertainty occurs at the calibration point with the lowest CH_4 concentration. The values of the variables and their respective uncertainties at this condition are:

$$y_{THC,bot} = 5030 \pm 101 \text{ ppm}$$

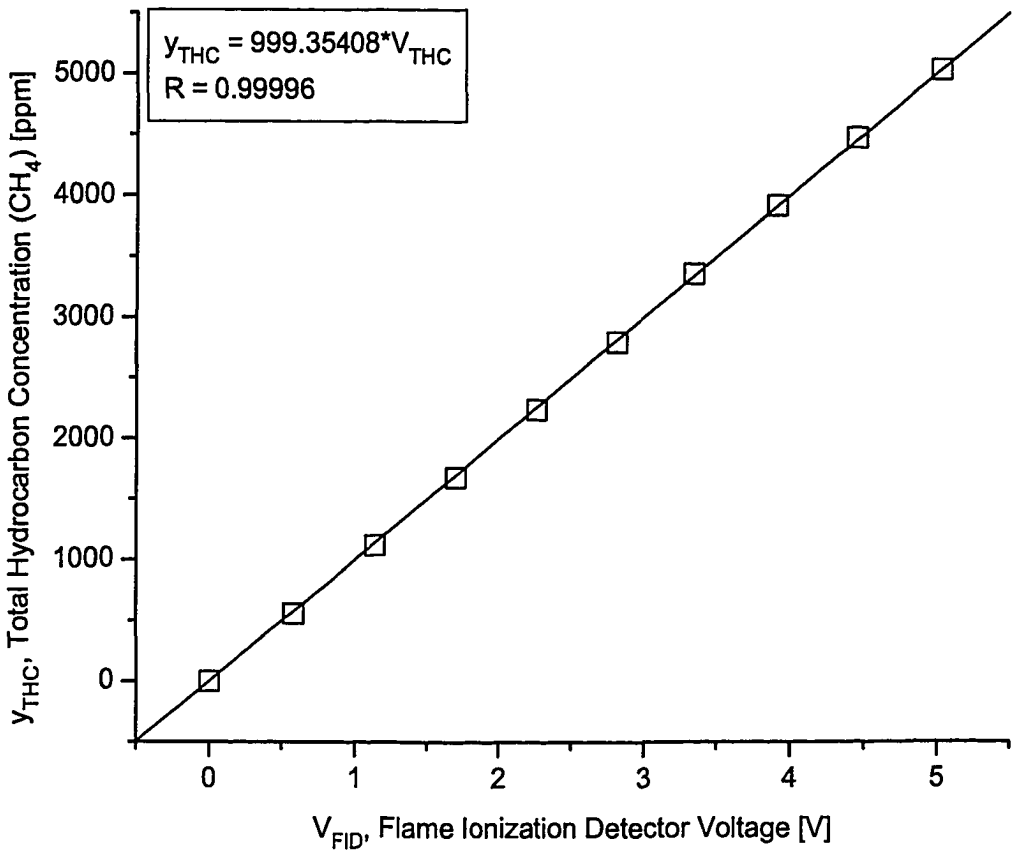

Figure B.8: Calibration of California Analytical model 300M-FID flame ionization detector gas analyzer.

$$Q_{THC,bot} = 1.11 \pm 0.03 \text{ LPM}$$
$$Q_{N_2,bot} = 8.89 \pm 0.03 \text{ LPM}$$

A worst case uncertainty in measured THC concentration is then calculated as:

$$\boxed{y_{THC} = 559 \pm 16 \text{ ppm}} \tag{B.19}$$

A representative calibration plot of the California Analytical model 300M-FID flame ionization detector is given in Figure B.8.

B.6.3 NDIR Gas Analyzer

A California Analytical model 300 non-dispersive infrared (NDIR) gas analyzer was used to measure both the CO_2 and CO of gas samples in this study. Prior to calibration or usage, the NDIR analyzer was allowed to warm up for a minimum of one hour.

B.6.3.1 Carbon Dioxide Measurements

To calibrate the NDIR analyzer for CO_2 measurements, varying blends of CO_2 and N_2 were supplied to the NDIR analyzer using a multi-gas calibrator. CO_2 was provided from a Praxair Certified Standard gas cylinder with a CO_2 concentration of 20.2% while N_2 was supplied from a separate gas cylinder. The NDIR analyzer was calibrated over a range of 0 to 20.2% CO_2 using an analyzer measurement range of 0 to 25%. For a given blend of CO_2 and N_2, the CO_2 concentration can be calculated as:

$$y_{CO_2} = \frac{y_{CO_2,bot} Q_{CO_2,bot}}{Q_{CO_2,bot} + Q_{N_2,bot}} \tag{B.20}$$

where: $y_{CO_2,bot}$ = Molar concentration of CO_2 in calibration gas
$Q_{CO_2,bot}$= Volume flow rate of calibration gas
$Q_{N_2,bot}$ = Volume flow rate of N_2 dilution gas

To determine the uncertainty in measured CO_2 concentration, Equation B.20 can be differentiated according to Equation B.1 as:

$$\delta y_{CO_2} = \left\{ \left[\frac{Q_{CO_2,bot} \cdot \delta y_{CO_2,bot}}{Q_{CO_2,bot} + Q_{N_2,bot}} \right]^2 + \left[\frac{y_{CO_2,bot} \cdot \delta Q_{CO_2,bot}}{Q_{CO_2,bot} + Q_{N_2,bot}} - \frac{y_{CO_2,bot} \cdot Q_{CO_2,bot} \cdot \delta Q_{CO_2,bot}}{(Q_{CO_2,bot} + Q_{N_2,bot})^2} \right]^2 + \left[\frac{y_{CO_2,bot} \cdot Q_{CO_2,bot} \cdot \delta Q_{N_2,bot}}{-(Q_{CO_2,bot} + Q_{N_2,bot})^2} \right]^2 \right\}^{0.5} \tag{B.21}$$

Again, the uncertainty in the CO_2 concentration in the calibration gas is constant, thus a worst case uncertainty in measured CO_2 concentration

occurs at the lowest concentration that was calibrated. The variables and respective uncertainties at this condition are:

$$y_{CO_2,bot} = 20.2 \pm 0.4\ \%$$
$$Q_{CO_2,bot} = 1.11 \pm 0.03\ \text{LPM}$$
$$Q_{N_2,bot} = 8.89 \pm 0.03\ \text{LPM}$$

A worst case uncertainty in measured CO_2 concentration can then be calculated as:

$$\boxed{y_{CO_2} = 2.24 \pm 0.06\ \%} \tag{B.22}$$

A representative calibration plot of the California Analytical 300 NDIR gas analyzer is shown in Figure B.9 for CO_2.

B.6.3.2 Carbon Monoxide Measurements

The procedure for calibrating the NDIR gas analyzer for CO is much the same as that for CO_2, which was discussed in Section B.6.3.1. The CO was provided from a Praxair Certified Standard gas cylinder with a CO concentration of 2.45%. The CO was mixed in various proportions with N_2 from a separate cylinder through the use of a multi-gas calibrator. The NDIR analyzer was calibrated over a range of 0 to 2.45% CO using an analyzer measurement range of 0 to 2.5%. For a given blend of CO and N_2, the CO concentration can be calculated as:

$$y_{CO} = \frac{y_{CO,bot}\, Q_{CO,bot}}{Q_{CO,bot} + Q_{N_2,bot}} \tag{B.23}$$

where: $y_{CO,bot}$ = Molar concentration of CO in calibration gas
$Q_{CO,bot}$ = Volume flow rate of calibration gas
$Q_{N_2,bot}$ = Volume flow rate of N_2 dilution gas

The uncertainty in measured CO concentration can then be determined by differentiating Equation B.23 according to Equation B.1 as:

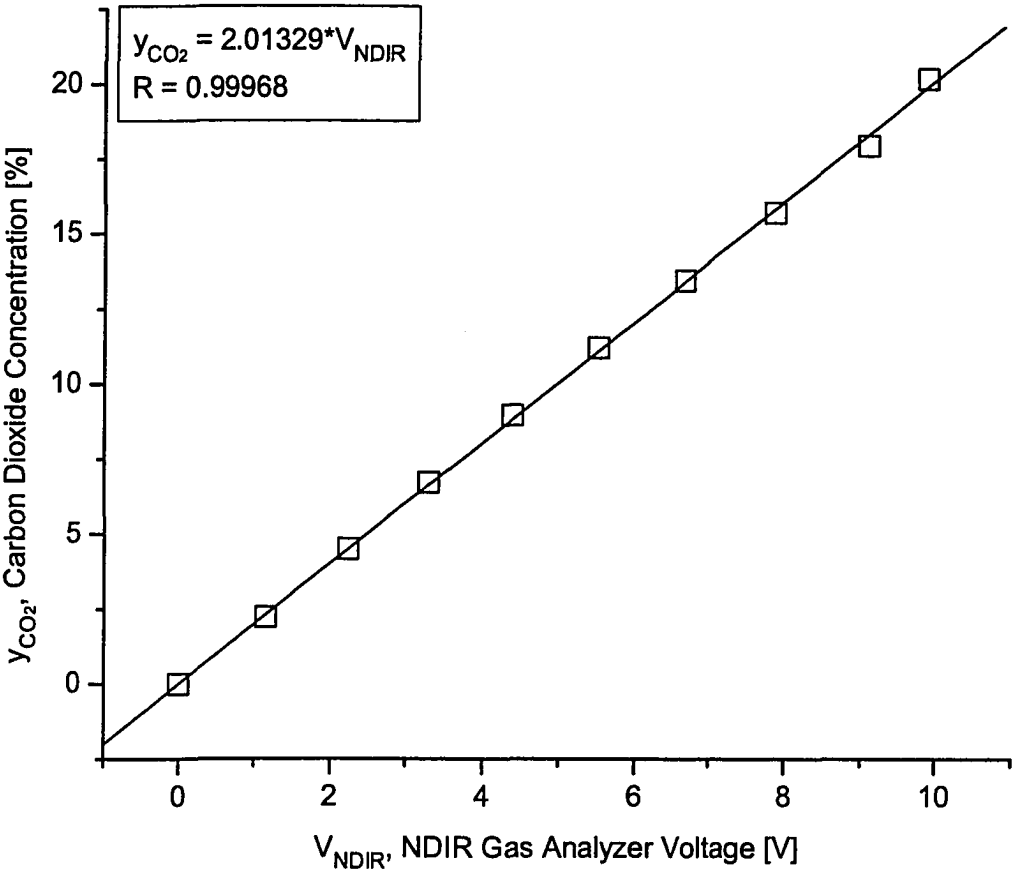

Figure B.9: Calibration of California Analytical model 300 non-dispersive infrared gas analyzer for CO_2.

$$\delta y_{CO} = \left\{ \left[\frac{Q_{CO,bot} \cdot \delta y_{CO,bot}}{Q_{CO,bot} + Q_{N_2,bot}} \right]^2 + \left[\frac{y_{CO,bot} \cdot \delta Q_{CO,bot}}{Q_{CO,bot} + Q_{N_2,bot}} - \frac{y_{CO,bot} \cdot Q_{CO,bot} \cdot \delta Q_{CO,bot}}{(Q_{CO,bot} + Q_{N_2,bot})^2} \right]^2 + \left[\frac{y_{CO,bot} \cdot Q_{CO,bot} \cdot \delta Q_{N_2,bot}}{-(Q_{CO,bot} + Q_{N_2,bot})^2} \right]^2 \right\}^{0.5} \quad \text{(B.24)}$$

As with CO_2, a worst case uncertainty in measured CO concentration occurs at the minimum calibrated concentration. Values of the variables and their respective uncertainties at this conditions are:

$y_{CO,bot} = 2.45 \pm 0.05$ %
$Q_{CO,bot} = 1.11 \pm 0.03$ LPM
$Q_{N_2,bot} = 8.89 \pm 0.03$ LPM

A worst case uncertainty in measured CO concentration can then be calculated as:

$$\boxed{y_{CO} = 0.272 \pm 0.007\ \%} \quad \text{(B.25)}$$

A representative calibration plot of the California Analytical 300 NDIR gas analyzer is shown in Figure B.10 for CO.

B.6.4 Paramagnetic Gas Analyzer

A California Analytical model 100P paramagnetic gas analyzer was used in this study to measure the O_2 concentration in exhaust gas samples. Prior to calibration or experimentation, the paramagnetic analyzer was allowed to warm up for a minimum of one hour. Using a multi-gas calibrator and separate gas cylinders, various O_2-N_2 blends were used to calibrate the gas analyzer. A Praxair Certified Standard gas cylinder with an O_2 concentration of 20.95% was blended with N_2 from a separate gas cylinder for the calibration. The paramagnetic analyzer was calibrated over a range of 0 to

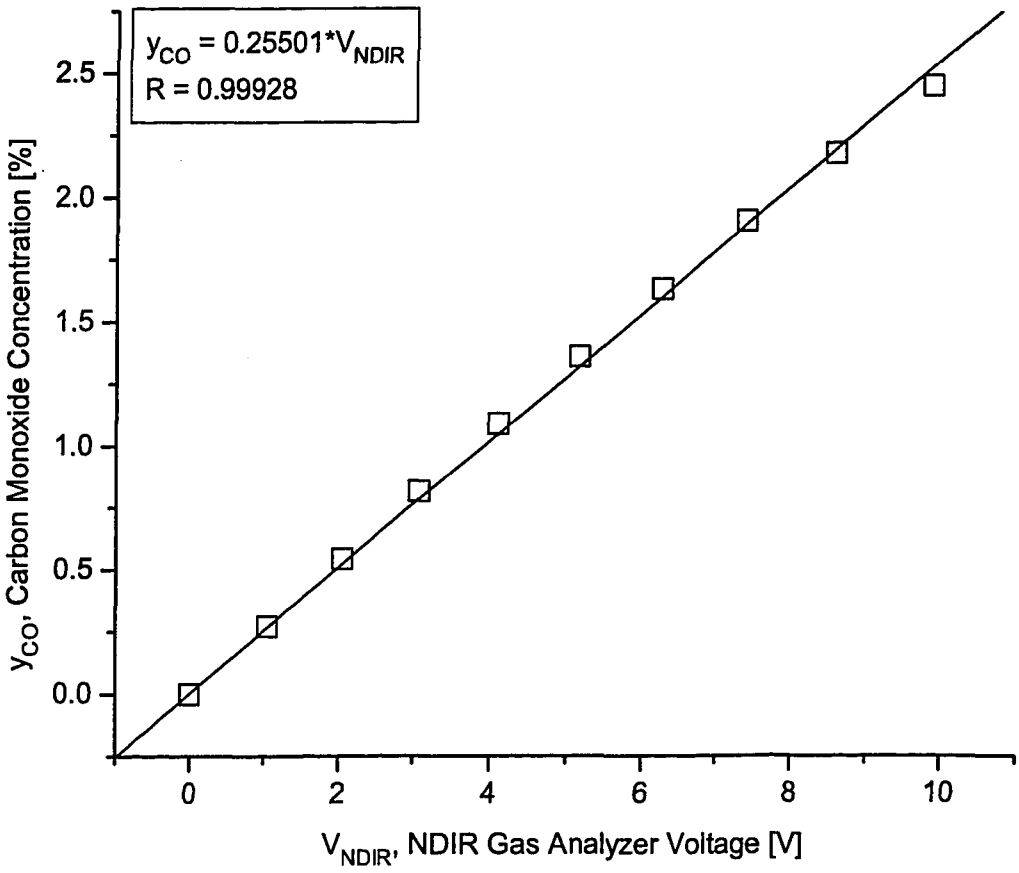

Figure B.10: Calibration of California Analytical model 300 non-dispersive infrared gas analyzer for CO.

20.95% O_2 using an analyzer measurement range of 0 to 25%. For a given O_2-N_2 blend, the O_2 concentration can be determined as:

$$y_{O_2} = \frac{y_{O_2,bot}\, Q_{O_2,bot}}{Q_{O_2,bot} + Q_{N_2,bot}} \tag{B.26}$$

where: $y_{O_2,bot}$ = Molar concentration of O_2 in calibration gas
$Q_{O_2,bot}$= Volume flow rate of calibration gas
$Q_{N_2,bot}$= Volume flow rate of N_2 dilution gas

To determine an expression for the uncertainty in measured O_2 concentration, Equation B.26 can be differentiated according to Equation B.1, yielding:

$$\delta y_{O_2} = \left\{ \left[\frac{Q_{O_2,bot} \cdot \delta y_{O_2,bot}}{Q_{O_2,bot} + Q_{N_2,bot}} \right]^2 + \left[\frac{y_{O_2,bot} \cdot \delta Q_{O_2,bot}}{Q_{O_2,bot} + Q_{N_2,bot}} - \frac{y_{O_2,bot} \cdot Q_{O_2,bot} \cdot \delta Q_{O_2,bot}}{(Q_{O_2,bot} + Q_{N_2,bot})^2} \right]^2 + \left[\frac{y_{O_2,bot} \cdot Q_{O_2,bot} \cdot \delta Q_{N_2,bot}}{-(Q_{O_2,bot} + Q_{N_2,bot})^2} \right]^2 \right\}^{0.5} \tag{B.27}$$

As in the calibration of the other gas analyzers, a worst case uncertainty occurs for the lowest calibrated O_2 concentration. The values of variables and respective uncertainties at this condition are:

$y_{O_2,bot}$ = 21.0 ± 0.4%
$Q_{O_2,bot}$= 1.11 ± 0.03 LPM
$Q_{N_2,bot}$= 8.89 ± 0.03 LPM

The worst case uncertainty in measured O_2 concentration can then be calculated as:

$$\boxed{y_{O_2} = 2.33 \pm 0.07\ \%} \tag{B.28}$$

A representative calibration plot of the California Analytical 100P paramagnetic gas analyzer is shown in Figure B.11.

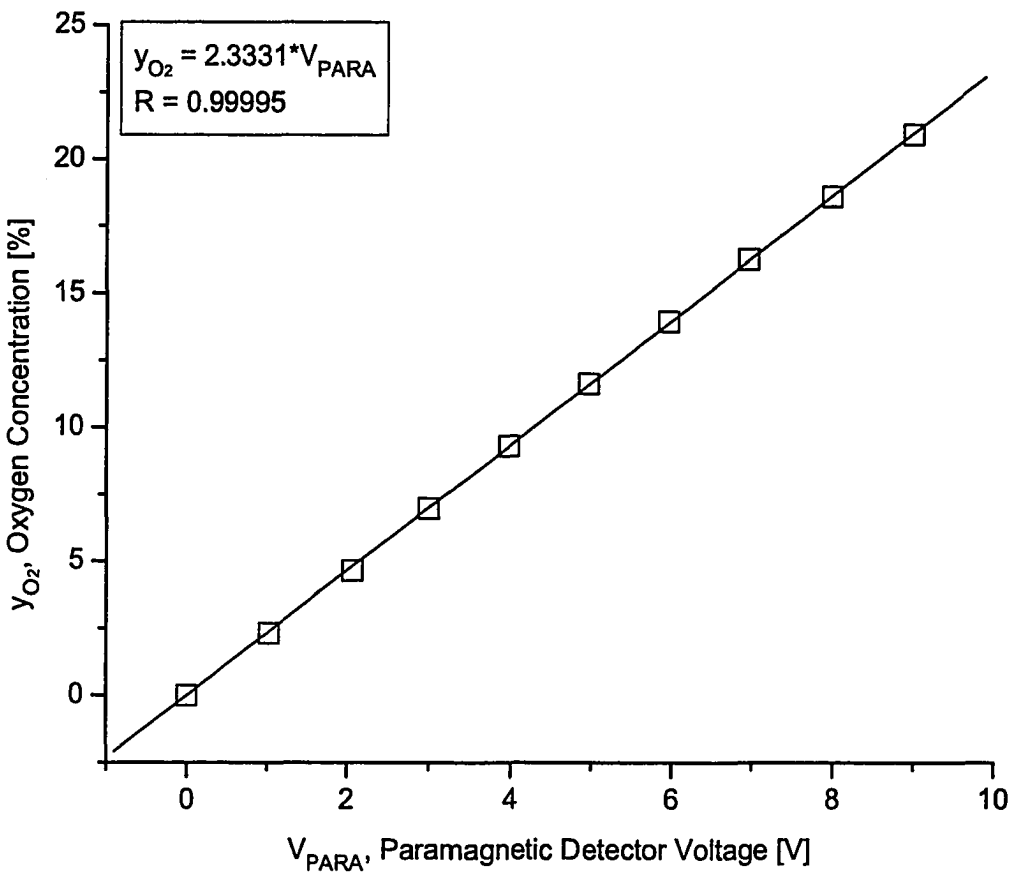

Figure B.11: Calibration of California Analytical model 100P paramagnetic gas analyzer.

B.7 Rotary Encoder Alignment

To obtain relevant measurements with the MTS combustion analysis system (CAS), it was first necessary to establish the relationship between piston TDC and the 1 PPR pulse from the BEI crankshaft rotary encoder. After removing the spark plug, piston displacement was measured directly using a Lucas/Schaevitz model 500DC-E linear variable differential transformer (LVDT) mounted on a magnetic base. The output from both the LVDT and the BEI crankshaft rotary encoder were connected to a Labview data acquisition system, thus allowing for LVDT measurements to be obtained at a sample rate based on crankshaft position. To measure the 1 PPR pulse from the rotary encoder as an analog input to the Labview data acquisition system, it was necessary to use a Dynascan model 3300 pulse generator. The 1 PPR pulse from the rotary encoder was used as an external trigger to the pulse generator, which produced a wider pulse which was measurable as an analog signal to the Labview data acquisition system.

After warming up the engine and achieving steady oil and coolant temperatures, the engine was shut off and the spark plug removed. The LVDT was mounted through the spark plug hole as previously described and all instrumentation was connected to the Labview data acquisition system. The crankshaft position was set to an approximate value of TDC on the exhaust stroke, based on the valve and indicated flywheel positions. With the data acquisition software running, the engine was turned by hand for five complete engine cycles. Piston displacement was measured at 0.1° CA intervals and the "stretched" index pulse from the pulse generator was measured on a separate channel. Results from the calibration are shown in Figure B.12. Here it is shown that, on average, the 1 PPR pulse from the BEI crankshaft rotary encoder occurred 271.5° CA prior to TDC on the compression stroke. This relationship was then used in MTS CAS to relate absolute piston position to the crankshaft rotary encoder 1 PPR pulse.

B.8 Cylinder Pressure Transducer

The Kistler model 6043A water cooled piezoelectric pressure transducer was calibrated over a range of 0 to 50 bar by the manufacturer[4] with a stated full scale linearity of ±0.1%. A full overview of the pressure transducer

[4]Kistler calibration certificate serial number: 1246099

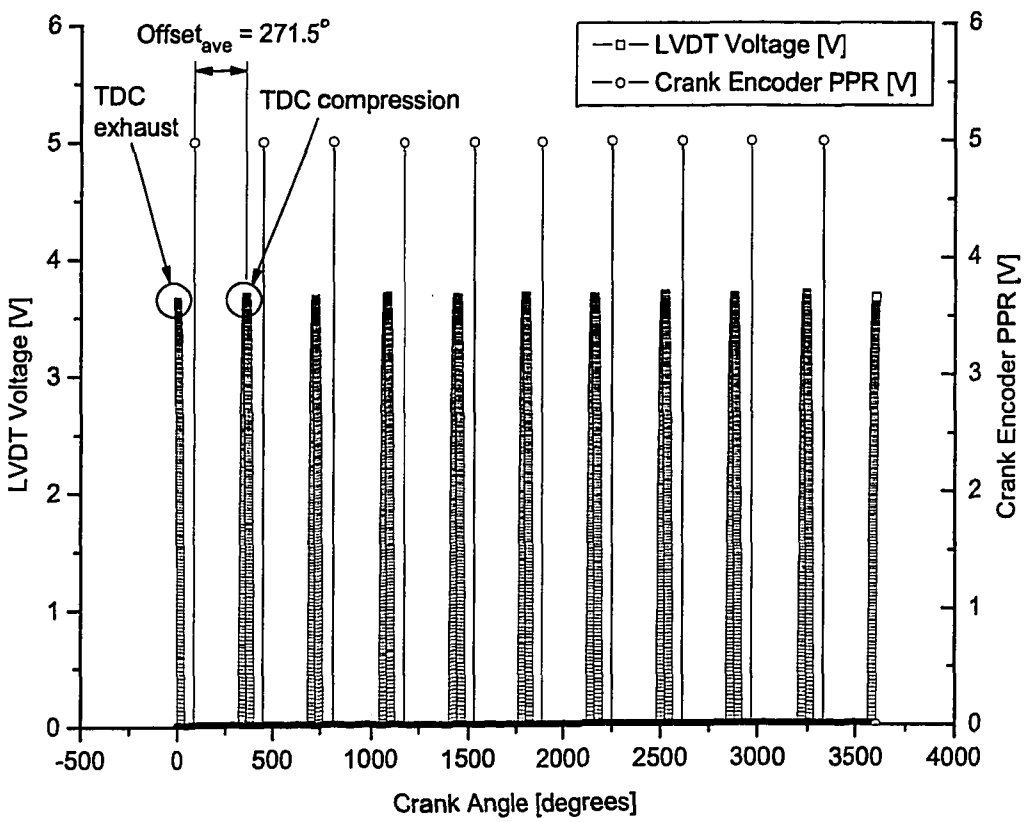

Figure B.12: Aligning the BEI rotary encoder with piston TDC.

Table B.2: Kistler 6043A Cylinder Pressure Transducer Properties

Description	Value
Measurement Range [bar]	0 to 250
Calibrated Measurement Range [bar]	0 to 50
Overload Limit [bar]	300
Sensitivity [pC/bar]	-20
Calibrated Sensitivity (50°C) [pC/bar]	-19.7
Natural Frequency [kHz]	70
Linearity [%FSO]	$\leq \pm 0.5$
Calibrated Linearity [%FSO]	$\leq \pm 0.1$
Hysteresis [%FSO]	≤ 0.5
Optimal Temperature With Cooling [°C]	50
Cooling Water Flow [LPM]	0.5 to 1
Change in Sensitivity With Cooling (50±35°C) [%]	±0.5
Insulation Resistance (20°C) [Ω]	$> 10^{13}$

characteristics is given in Table B.2.

Because the pressure transducer calibration was performed over a range of 0 to 50 bar, the maximum calibration uncertainty would occur at the minimum calibrated pressure as the linearity is given in terms of a percentage of the full scale pressure. As the details of this minimum pressure are not given, a value for maximum calibration uncertainty cannot be calculated.

APPENDIX C

PHYSICAL PROPERTIES

C.1 Gaseous Fuels

C.1.1 Natural Gas

The natural gas used to fuel the cooperative fuel research (CFR) engine was taken from the domestic supply which is obtained via an underground pipeline from the Edmonton Ethane Extraction Plant. An analysis of the natural gas was obtained from Atco Pipelines. The analysis was performed on a gas chromatograph and measured the mole fractions of thirteen separate molecular components. Any individual component which accounted for less than one molar percent was not included in the gas property calculations. The remaining components were normalized to maintain a fractional sum of unity. An average of 12 consecutive days readings was used in reporting the natural gas composition, which is shown in Table C.1.

C.1.2 H_2

Industrial grade H_2 with a stated purity of 99.95% was obtained from Praxair in pressurized cylinders.

C.2 Air/Fuel Mixture

To calculate the stoichiometric air/fuel ratio, the typical hydrocarbon combustion equation was modified to include the following: a blend of both natural gas and H_2 fuels; the natural gas composition given in Table C.1; and the water vapour fraction present in the air. As both air and fuel amounts were measured as rates, the combustion equation can be written as:

Table C.1: Domestic Natural Gas Properties

Description	Value
Normalized CH_4 Dry Molar Fraction	95.39%
Normalized C_2H_6 Dry Molar Fraction	1.90%
Normalized N_2 Dry Molar Fraction	1.93%
Normalized CO_2 Dry Molar Fraction	0.78%
Molar Mass [g/mol]	16.76
Density at STP[1][kg/m^3]	0.748
H/C Ratio	3.92
Lower Heating Value [kJ/kg]	44818

[1] 273.15 K and 101.325 kPa

$$\begin{aligned} \dot{\alpha}\, H_2 \; &+ \\ \dot{\beta}\,(0.007778\, CO_2 + 0.01934\, N_2 & \\ + 0.9539\, CH_4 + 0.01901\, C_2H_6) \; &+ \\ \dot{\gamma}\,(O_2 + 3.773\, N_2 + \delta\, H_2O) \; &\rightarrow \\ \dot{\epsilon}\, H_2O + \dot{\eta}\, CO_2 + \dot{\theta}\, N_2 \end{aligned} \qquad \text{(C.1)}$$

All three of $\dot{\alpha}$, $\dot{\beta}$ and $\dot{\gamma}$ were measured using mass flow meters; δ can be calculated using partial pressures with water vapour (P_{v,H_2O}) and atmospheric (P_{atm}) pressures. While P_{atm} can be measured using a mercury barometer, determining P_{v,H_2O} requires the use of a wet sling psychrometer and associated psychrometric equations.

To calculate the relative air/fuel ratio, λ, it is necessary to first calculate the stoichiometric value of $\dot{\gamma}$ for a given $\dot{\alpha}$ and $\dot{\beta}$. The four unknowns to be determined are then $\dot{\gamma}$, $\dot{\epsilon}$, $\dot{\eta}$ and $\dot{\theta}$. To solve for the four unknowns, Equation C.1 is rearranged into matrix form to perform elemental balances on each of C, H, N and O, as:

$$\begin{bmatrix} 0\dot{\gamma} & + & 0\dot{\epsilon} & + & 1\dot{\eta} & + & 0\dot{\theta} \\ 2\delta\dot{\gamma} & - & 2\dot{\epsilon} & + & 0\dot{\eta} & + & 0\dot{\theta} \\ (2+\delta)\dot{\gamma} & - & 1\dot{\epsilon} & - & 2\dot{\eta} & + & 0\dot{\theta} \\ 7.546\dot{\gamma} & + & 0\dot{\epsilon} & + & 0\dot{\eta} & - & 2\dot{\theta} \end{bmatrix} = \begin{vmatrix} 0.9997\dot{\beta} \\ -2\dot{\alpha} - 3.930\dot{\beta} \\ -0.01556\dot{\beta} \\ -0.03868\dot{\beta} \end{vmatrix} \qquad \text{(C.2)}$$

Equation C.2 is then solved for each of $\dot{\gamma}$, $\dot{\epsilon}$, $\dot{\eta}$ and $\dot{\theta}$ after which the relative air/fuel ratio can be calculated as:

$$\lambda = \frac{(\frac{A}{F})_{actual}}{(\frac{A}{F})_{stoich}} = \left(\frac{\dot{m}_{air,actual}}{\dot{m}_{H_2} + \dot{m}_{CNG}}\right) \cdot \left(\frac{\dot{m}_{H_2} + \dot{m}_{CNG}}{\dot{m}_{air,stoich}}\right) = \frac{\dot{m}_{air,actual}}{\dot{m}_{air,stoich}} \quad \text{(C.3)}$$

where

$$\dot{m}_{air,stoich} = M_{air}\,\dot{\gamma} \quad \text{(C.4)}$$

and $\dot{m}_{air,actual}$ is measured directly with the intake air mass flow meter. The relative air/fuel ratio (λ) is then:

$$\boxed{\lambda = \frac{\dot{m}_{air,actual}}{M_{air}\,\dot{\gamma}}} \quad \text{(C.5)}$$

APPENDIX D

CALCULATING EGR MASS FRACTION

To calculate the amount of external exhaust gas recirculation (EGR) dilution, the mole fraction of CO_2 was measured in the intake plenum of the engine, directly downstream of the EGR inlet. The EGR mass fraction can be defined as (Heywood, 1988):

$$m_{EGR} = \frac{\dot{m}_{EGR}}{\dot{m}_i} \tag{D.1}$$

where $\dot{m}_{EGR}$ and $\dot{m}_i$ are the EGR and total intake (including EGR) mass flow rates.

To relate m_{EGR} to the "dry"[1] measured mole fraction of CO_2 ($y_{CO_2,KO}$) within the intake plenum, it is necessary to start with the typical stoichiometric hydrocarbon combustion equation modified to include: a blend of both natural gas and H_2 fuels; the natural gas composition given in Table C.1; and the water vapour fraction present in the air. This modified combustion equation is given as:

$$\begin{aligned} \dot{\alpha}\, H_2 \quad &+ \\ \dot{\beta}\,(0.007778\, CO_2 + 0.01934\, N_2 & \\ + 0.9539\, CH_4 + 0.01901\, C_2H_6) \quad &+ \\ \dot{\gamma}\,(O_2 + 3.773\, N_2 + \delta\, H_2O) \quad &\rightarrow \\ \dot{\epsilon}\, H_2O + \dot{\eta}\, CO_2 + \dot{\theta}\, N_2 & \end{aligned} \tag{D.2}$$

[1] A portion of water is removed from the sample by passing through a water knockout heat exchanger

where: $\dot{\alpha}$ = Mole rate of H_2
$\dot{\beta}$ = Mole rate of natural gas
$\dot{\gamma}$ = Mole rate of air
δ = Number of moles of water in air

An elemental balance for each of carbon (C), nitrogen (N) and hydrogen (H) allows for the restatement of Equation D.2 wholly in terms of the measured reactant mole rates:

$$\begin{aligned}
\dot{\alpha}\, H_2 \; &+ \\
\dot{\beta}\,(0.007778\, CO_2 + 0.01934\, N_2 & \\
+ 0.9539\, CH_4 + 0.01901\, C_2H_6) \; &+ \\
\dot{\gamma}\,(O_2 + 3.773\, N_2 + \delta\, H_2O) \; &\rightarrow \\
& (\dot{\alpha} + 1.9648\,\dot{\beta} + \delta\,\dot{\gamma})\, H_2O \\
&+ \; (0.9997\,\dot{\beta})\, CO_2 \\
&+ \; (0.01934\,\dot{\beta} + 3.773\,\dot{\gamma})\, N_2 \qquad \text{(D.3)}
\end{aligned}$$

The addition of EGR can be represented as a fraction, μ, of the exhaust products shown in Equation D.3 being recirculated as reactants:

$$\begin{aligned}
\dot{\alpha}\, H_2 \; &+ \\
\dot{\beta}\,(0.007778\, CO_2 + 0.01934\, N_2 & \\
+ 0.9539\, CH_4 + 0.01901\, C_2H_6) \; &+ \\
\dot{\gamma}\,(O_2 + 3.773\, N_2 + \delta\, H_2O) \; &+ \\
\mu\,(\dot{\alpha} + 1.9648\,\dot{\beta} + \delta\,\dot{\gamma})\, H_2O \; &+ \\
\mu\,(0.9997\,\dot{\beta})\, CO_2 \; &+ \\
\mu\,(0.01934\,\dot{\beta} + 3.773\,\dot{\gamma})\, N_2 \; &\rightarrow \\
& (1+\mu)\,(\dot{\alpha} + 1.9648\,\dot{\beta} + \delta\,\dot{\gamma})\, H_2O \\
&+ \; (1+\mu)\,(0.9997\,\dot{\beta})\, CO_2 \\
&+ \; (1+\mu)\,(0.01934\,\dot{\beta} + 3.773\,\dot{\gamma})\, N_2 \\
& \qquad \text{(D.4)}
\end{aligned}$$

The relation between the measured dry CO_2 mole fraction ($y_{CO_2,KO}$) and the fraction, μ, of EGR can be established by first considering the composition of the intake plenum sample. The measured CO_2 mole fraction can be represented as:

$$y_{CO_2,dry} = \frac{\dot{n}_{CO_2}}{\dot{n}_{CO_2} + \dot{n}_{N_2} + \dot{n}_{H_2O,KO} + \dot{n}_{air}} \tag{D.5}$$

where: $\dot{n}_{CO_2}$ = Mole rate of CO_2 in intake plenum
$\dot{n}_{N_2}$ = Mole rate of N_2 in intake plenum
$\dot{n}_{H_2O,KO}$ = Mole rate of water in intake plenum sample downstream of water knockout
$\dot{n}_{air}$ = Mole rate of air in intake plenum

All terms in Equation D.5 except $\dot{n}_{H_2O,KO}$ can be calculated directly from the measured reactant mass flow rates. To calculate $\dot{n}_{H_2O,KO}$ it necessary to measure temperature and pressure within the sample line downstream of the water knockout, at which point the specific humidity of the sample can be calculated as:

$$\omega = \frac{m_v}{m_a} = \frac{P_v R_a}{P_a R_v} \tag{D.6}$$

where: m_v = Mass of water in sample
m_a = Mass of remaining "dry" components in sample
P_v = Partial pressure of water in sample
P_a = Partial pressure of remaining "dry" components in sample
R_v = Water gas constant
R_a = Gas constant of remaining "dry" components in sample

Equation D.6 can be restated in terms of known quantities by noting that: the partial pressure of water in the sample (P_v) is equal to the saturated vapour pressure at the measured sample temperature ($P_{sat@T}$); the partial pressure of the remaining dry sample components is the difference between the measured sample pressure (P_{sample}) and the partial pressure of water in the sample ($P_{sat@T}$); and the gas constant of the remaining dry sample components can be calculated as the ratio of the universal gas constant (R_u) to the collective molar mass of the dry sample components ($M_{sample,dry}$). The

mole rate of water within the gas sample downstream of the water knockout ($\dot{n}_{H_2O,KO}$) can then be expressed as:

$$\dot{n}_{H_2O,KO} = \frac{P_{sat@T}\left(\dot{n}_{CO_2} + \dot{n}_{N_2} + \dot{n}_{air,dry}\right)}{\left(P_{sample} - P_{sat@T}\right)} \tag{D.7}$$

where: $P_{sat@T}$ = Saturated vapour pressure at sample line temperature
$\dot{n}_{air,dry}$ = Mole rate of dry air
P_{sample} = Measured sample line pressure

Substituting Equation D.7 into D.5 results in an expression for the measured mole fraction of CO_2 (y_{CO_2}) in terms of known quantities:

$$y_{CO_2,dry} = \frac{\dot{n}_{CO_2}}{\dot{n}_{CO_2} + \dot{n}_{N_2} + \frac{P_{sat@T}\left(\dot{n}_{CO_2}+\dot{n}_{N_2}+\dot{n}_{air,dry}\right)}{\left(P_{sample}-P_{sat@T}\right)} + \dot{n}_{air}} \tag{D.8}$$

The mole rates of CO_2, N_2, dry air and air within the intake plenum can be expressed, as in Equation D.4:

$$\begin{aligned} \dot{n}_{CO_2} &= \mu\left(0.9997\,\dot{\beta}\right) \\ \dot{n}_{N_2} &= \mu\left(0.01934\,\dot{\beta} + 3.773\,\dot{\gamma}\right) \\ \dot{n}_{air,dry} &= 4.773\,\dot{\gamma} \\ \dot{n}_{air} &= \dot{\gamma}\left(4.773 + \delta\right) \end{aligned} \tag{D.9}$$

Substituting the expressions given in Equation D.9 into Equation D.8 (and some algebraic manipulation) results in an expression for the EGR fraction (μ) solely in terms of measured and known quantities:

$$\mu = \frac{\dot{\gamma}\left[\frac{4.773\,P_{sat@T}}{\left(P_{sample}-P_{sat@T}\right)} + 4.773 + \delta\right]}{\frac{0.9997\,\dot{\beta}}{y_{CO_2}} - \left(1.0190\,\dot{\beta} + 3.773\,\dot{\gamma}\right)\left[1 + \frac{P_{sat@T}}{\left(P_{sample}-P_{sat@T}\right)}\right]} \tag{D.10}$$

Now that the EGR fraction (μ) has been represented in terms of measured and known quantities, it is possible to calculate the EGR mole fraction as:

$$y_{EGR} = \frac{\dot{n}_{H_2O} + \dot{n}_{CO_2} + \dot{n}_{N_2}}{\dot{n}_{H_2O} + \dot{n}_{CO_2} + \dot{n}_{N_2} + \dot{n}_{H_2} + \dot{n}_{CNG} + \dot{n}_{air}} \tag{D.11}$$

where:
$$\dot{n}_{H_2O} = \mu\,(\dot{\alpha} + 1.9648\,\dot{\beta} + \delta\,\dot{\gamma})$$
$$\dot{n}_{CO_2} = \mu\,(0.9997\,\dot{\beta})$$
$$\dot{n}_{N_2} = \mu\,(0.01934\,\dot{\beta} + 3.773\,\dot{\gamma})$$
$$\dot{n}_{H_2} = \dot{\alpha}$$
$$\dot{n}_{CNG} = \dot{\beta}$$
$$\dot{n}_{air} = \dot{\gamma}\,(4.773 + \delta)$$

Finally, Equation D.11 and the calculated molar masses of the EGR (M_{EGR}) and intake mixture (M_{intake}) can be combined to solve for the EGR mass fraction:

$$\boxed{m_{EGR} = \frac{y_{EGR}\,M_{EGR}}{M_{intake}}} \tag{D.12}$$